Citation for published version:
Gursul, I, Gordnier, R & Visbal, M 2005, 'Unsteady Aerodynamics of Nonslender Delta Wings', *Progress in Aerospace Sciences*, vol. 41, no. 7, pp. 515-557. https://doi.org/10.1016/j.paerosci.2005.09.002

DOI:
10.1016/j.paerosci.2005.09.002

Publication date:
2005

Link to publication

University of Bath

Alternative formats
If you require this document in an alternative format, please contact:
openaccess@bath.ac.uk

General rights
Copyright and moral rights for the publications made accessible in the public portal are retained by the authors and/or other copyright owners and it is a condition of accessing publications that users recognise and abide by the legal requirements associated with these rights.

Take down policy
If you believe that this document breaches copyright please contact us providing details, and we will remove access to the work immediately and investigate your claim.

Download date: 05. May. 2023

UNSTEADY AERODYNAMICS OF NONSLENDER DELTA WINGS

I. Gursul*, R. Gordnier**, and M. Visbal**

Abstract

Unsteady aerodynamics of nonslender delta wings, covering topics of shear layer instabilities, structure of nonslender vortices, breakdown, maneuvering wings, and fluid/structure interactions, are reviewed in this paper. Vortical flows develop at very low angles of attack, and form close to the wing surface. This results in strong interactions with the upper-surface boundary layer and in a pronounced dependence of the flow structure on Reynolds number. Vortex breakdown is observed to be much less abrupt compared to breakdown over slender wings. This results in challenges for the precise determination of vortex breakdown location and the interpretation of flow visualizations. One of the distinct features of nonslender wings is the location of the primary attachment zone outboard of the symmetry plane. Reattachment location correlates with the wing stall process and increased buffeting. Dramatic fluid/structure interactions emerge with increasing wing flexibility and result in substantial lift enhancement in the post-stall region. This recently discovered phenomenon appears to be a feature of nonslender wings. Rigid delta wings undergoing small amplitude oscillations in the post-stall region exhibit many similarities to flexible wings, including reattachment and re-formation of the leading-edge vortices. Unusual self-excited roll oscillations have also been observed for free-to-roll nonslender wings.

* University of Bath, Department of Mechanical Engineering, Bath, BA2 7AY, UK

** Air Force Research Laboratory, Wright Patterson Air Force Base, OH 45433, USA

NOMENCLATURE

c	root chord length
C_L	lift coefficient
C_N	normal force coefficient
C_R	rolling moment coefficient
C_p	pressure coefficient
f	frequency
k	fluctuating kinetic energy
Re	Reynolds number based on chord length
s	local semispan
S	spectral density
St	Strouhal number
t	time; thickness of delta wing
T	period
u	axial velocity
U_∞	free stream velocity
v	swirl velocity
x	chordwise distance
x_{bd}	breakdown location
y	spanwise distance
z	vertical distance above wing surface
ϕ	roll angle; incidence of measurement plane
λ	wavelength; dimensionless flexibility parameter
Γ	circulation
Λ	sweep angle
α	angle of attack
δ	wing tip displacement
ν	kinematic viscosity
ω	vorticity

CONTENTS

1. Introduction

The next generation of unmanned flight vehicles will be highly flexible, will have lower structural-weight-to-take-off-weight ratios, and will be capable of performing extreme manuevers at high g. The proposed concepts will incorporate low to moderately swept (35° to 55°) wing planforms. Figure 1 shows some conceptual Unmanned Combat Air Vehicle (UCAV) designs, which incorporate blended delta wing-body configurations. Similarly, low-aspect ratio wings with low sweep angles are often used for Micro Air Vehicle (MAV) configurations, as shown in Figure 1. All these configurations exhibit vortex-dominated flows [1]. At the recent international "*Workshop on Aerodynamic Issues of Unmanned Air Vehicles*" [2] it was recognised that serious aerodynamic, stability and control issues may exist for these configurations. In most cases, laminar-transitional flows are dominant, and separation, transition and vortical flows play important roles.

The recent interest in MAVs and UAVs has resulted in a need to further our understanding of flows over nonslender delta wing configurations. For the purposes of this review article, a nonslender wing is defined as one with leading-edge sweep equal to or less than 55°. Vortical flow over nonslender delta wings has recently become a topic of increased interest in the literature. While the flow topology over more slender wings, typically $\Lambda \geq 65°$, has been extensively studied and is now reasonably well understood [3, 4, 5, 6], the flow over lower sweep wings has only recently attracted more attention [7].

1.1. Overview

Early work in the field [8] reported that the vortex core was very unsteady and the vortex breakdown was difficult to identify for sweep angles of 55° and 45°. Wentz and Kohlman [9]

indicated that the vortex breakdown was only observed in a region close to the apex for a Λ = 50° wing. Both studies, which were conducted at Reynolds numbers on the order of 10^6, concluded that the location of breakdown could not be found for a Λ = 45° wing, indicating that it was very close to the apex of the wing at small incidences.

Well-defined vortices were visible in low-Reynolds number experiments (Re = 7,000 in [10] and Re = 8,500 in [11]) over a Λ = 50° swept wing. At these very low Reynolds numbers, vortices exhibit wake-like axial velocity profiles even upstream of breakdown [11, 12, 13]. The vortices form close to the surface of the wing [14], and vortex/boundary layer interaction becomes important [15, 16]. A further consequence of the interaction between the boundary layer and vortex flows is the sensitivity of non-slender wing flows to the Reynolds number that is not observed over slender wings [17].

Separated and vortical flows are dominant even at very low incidences. The flows that occur over nonslender wings have been shown to differ substantially from those documented over more slender planforms at high angles of attack and Reynolds number. While a slender wing typically exhibits a coherent primary vortex generated by the rollup of the shear layer separating from each leading edge, recent computational and experimental studies have demonstrated that a 'dual' primary vortex structure exists over non-slender wings at low incidence. This vortex structure is a direct result of the proximity of the vortex formation to the wing surface, and the corresponding interaction with the surface boundary layer.

Evidence [8, 9] suggests that, at high Reynolds numbers, vortex breakdown occurs close to the apex of the wing even at small incidences. Substantial differences from the breakdown of slender vortices may exist, and there is evidence of highly unsteady flows over the wing. With increasing angle of attack, vortex breakdown reaches the apex, and the separated shear layers

become the dominant feature of the flow. Much of the existing knowledge on vortex flows is related to slender wings. A number of unsteady phenomena are known to exist over slender delta wings, such as vortex wandering [18], helical mode instability [19, 20], shear layer instabilities [21], vortex interactions [22], and at high incidences vortex shedding [23]. The role of these instabilities in buffeting of slender wings is well understood [24]. However, very little is known about the structure and characteristics of unsteady flow phenomena over nonslender wings.

A unique feature of nonslender vortices is that primary attachment occurs outboard of the symmetry plane even when vortex breakdown is close to the apex. With increasing incidence this attachment line moves in-board towards the wing centerline. Just prior to stall, substantial buffeting is associated with the attachment region. With further increase of angle of attack, reattachment is no longer observed, corresponding to stall of the wing.

1.2. Aerodynamic forces

There are surprisingly little force data on low-sweep delta wings in the literature. Compared with more slender planforms, nonslender wings have lower maximum lift coefficient and also lower stall angle [8]. Figure 2 shows the variation of lift coefficient for delta wings with various sweep angles in the range of Λ=45° to 76°, adapted from Earnshaw and Lawford's data [8]. For the delta wings with low sweep angle, the maximum lift coefficient decreases considerably, although the slope of the lift curve increases, as expected. Earnshaw and Lawford [8] measured the lift characteristics of a range of delta wings for Reynolds numbers in the range 0.2 to 0.5 million. However, the wings studied were relatively thick (having a thickness-to-chord ratio of 6%) and incorporated a slight stream-wise camber; these factors account for the negative

zero-lift angle (α_0) observed in their data. The slope of the pitching moment coefficient about the wing's apex increases in magnitude with decreasing sweep angle [8, 25].

According to Polhamus' leading-edge suction analogy [26], the vortex lift contribution becomes a smaller portion of the total lift as the sweep angle decreases. Also, there is no obvious correlation between the onset of vortex breakdown over nonslender wings and the change of the lift coefficient [27]. In a comparison of the lift coefficient at α=20° as a function of sweep angle, it is shown that the lift coefficient remains nearly the same for low sweep delta wings. Bartlett and Vidal [28] also showed that the lift coefficient at α=20° for four low-aspect ratio wings with sweep angles 0° to 30° is little affected.

The effect of wing sweep on normal force coefficient is even larger, in particular at high incidences. For low sweep angles, the normal force coefficient may become larger again after the initial drop following the stall [8]. Figure 3 shows the difference between the maximum normal force coefficient at stall and at zero incidence, $C_{N,max}$-$C_{N,0}$, as a function of sweep angle from various sources. It is seen that, for low and high sweep angles, there is a trend of reaching nearly constant values of maximum attainable force coefficient. While the local maximum for sweep angle Λ=70° is related to the vortex breakdown phenomenon, it is not clear why there is an asymptotic value at low sweep angles.

Strong Reynolds number influence [29] for Λ=55° wings, even with sharp leading-edges, was noted near the stall angle, with earlier stall as the Reynolds number is increased in the range of Re=0.38 to $2.2*10^6$. As will be discussed later, there is a direct relation between flow reattachment and stall; this indicates that the Reynolds number has possible effect on reattachment.

2. Structure of nonslender vortical flows

Before describing the distinctive characteristics of the vortex structure for low sweep delta wings, a brief description of the basic vortical flow features for high sweep wings is provided. Rockwell [3] and Visbal [4] have discussed extensively the mean and unsteady vortical flow structure over a 75° sweep delta wing. For a highly swept, sharp-edged delta wing boundary layer separation occurs at the leading edge and results in the formation of free, three-dimensional, shear layers that roll into a pair of counter rotating primary vortices. Viewed in a spanwise plane normal to the wing these vortices appear as a nearly circular region of high vorticity surrounded by a shear layer or feeding sheet which originates at the leading edge. This shear layer may exhibit various forms of instability giving rise to vortical sub-structures which wrap around the leading-edge vortex. The primary vortex interacts with the boundary layer developing on the upper surface of the wing giving rise to boundary layer separation and the formation of a secondary vortex of opposite sign vorticity.

As the angle of attack of a delta wing is increased the leading–edge vortices experience a dramatic flow disruption termed ‘vortex breakdown’ or ‘vortex burst’. For higher sweep delta wings the breakdown structure consists of a spiral winding opposite to the vortex swirl which rotates in the swirl direction. Interior to the spiral is a region of reverse axial flow which gives the characteristic switch from jet-like to wake-like flow from upstream to downstream of breakdown. The onset of breakdown is very abrupt with the core expanding by approximately a factor of 3.0. For this reason a location for vortex breakdown can be defined in a very straightforward manner as the point of maximum upstream penetration of the reversed axial flow. The fluctuations in the breakdown region due to the rotating spiral structure produce distinct, dominant peaks in the frequency spectra in the core of the vortex. The time-averaged

representation of the spiral breakdown results in single-celled bubbles of reversed axial flow with both front and aft stagnation points.

2.1. Vortex structure

Coherent leading edge vortices have been visualized experimentally for angles of attack as low as α=2.5°. Surface oil flow visualizations of a 50° sweep delta wing by Taylor and Gursul [30] show the distinctive imprint of a leading-edge vortex structure with a primary attachment line and secondary separation line clearly visible (see Figure 4). Ol and Gharib [11] have also stated that flow visualizations via dye injection indicate the presence of leading-edge vortices down to an angle of attack α=2.5°. Experimental measurements [11, 15, 31] and computational simulations [16] all report that for low angles of attack an elongated separated flow region exists which lies very close to the upper surface of the wing. A plot of the velocity profile through the vortex core from the computations of Gordnier and Visbal [16], Figure 5, indicates a broad wake-like flow. This is consistent with the experimental measurements [12, 13] which also exhibited wake-like behaviour for low angles of attack.

Computations [16] for a 50° sweep delta wing at α=5° have shown that this elongated separated flow region at low angles of attack can take on an interesting dual vortex structure, Figure 6. At upstream locations near the apex, the long, thin shear-layer that emanates from the leading edge of the delta wing terminates in the formation of the primary vortex. Further downstream a second vortex, with vorticity of the same sign as the primary vortex, emerges in the separated shear layer outboard of the primary vortex creating a dual vortex structure. This second vortex, which is slightly weaker and smaller than the original vortex, arises from the interaction of the secondary flow with the primary shear layer. As the secondary flow separates

from the surface it impinges on the primary shear layer splitting it into the two same sign vortices. At locations on the downstream half of the wing, the dual vortex structure weakens and becomes less distinct. This is attributable to the onset of unsteadiness on the aft portion of the wing.

The existence of this type of dual vortex structure has been confirmed by experimental PIV measurements [15, 31], Figure 7, albeit for different Reynolds numbers, sweep angle and angles of attack. Taylor et al [15] observed the dual vortex structure in PIV measurements for a 50° sweep wing at α=7.5° and a Reynolds number Re=8,700, Figure 7b. Sensitivity of this structure to Reynolds number was noted in these experiments and was also seen in the computations of Gordnier. This will be discussed in a subsequent section. PIV measurements by Yaniktepe and Rockwell [31] for a 38.7° sweep delta wing at α=7° angle of attack and Re=10,000, Figure 7c, showed two individual vorticity concentrations that retain their identity along the surface of the wing. They report the wavelength between these concentrations to be λ/s=0.25.

The mean structure of the vortex system changes as the angle of attack of the low sweep wing increases [16]. The primary vortex increases in both size and strength with the core of the primary vortex moving away from the surface and inboard on the wing. The axial velocity in the core of the primary vortex reaches values of twice the freestream velocity by α=15°, Figure 5. Stereo PIV velocity measurements by Ol and Gharib [11] at a lower Reynolds number, Re=8,500, indicate a conical flow development of the primary vortex in a region slightly downstream of the apex and upstream of the vortex breakdown location.

By α=10° a remnant of the dual vortex structure observed at 5° angle of attack remains, albeit with the primary vortex now being much more prominent than the second primary vortex

which stays embedded in the separated shear layer. As the angle of attack is increased further to α=15°, Figure 8, a vortex structure more reminiscent of those observed for higher sweep delta wings is recovered. A dual vortex structure can no longer be distinguished and the classic primary, secondary, and tertiary vortex structure characteristic of the flow over more slender delta wings (see for instance Visbal [4]) is recovered, Figure 8b. A substantial secondary separated flow region with axial vorticity of the opposite sign is obtained. Underneath this secondary flow structure is a region of tertiary flow with vorticity of the same sign as the primary vortex.

The impact of the vortical flow system above the wing on the surface flow is seen in Figure 9 for α=15°. Due to the strengthening of the primary vortex above the delta wing, low values of pressure are obtained under the vortical flow region. The limiting streamlines show a primary separation at the leading edge, primary attachment line (PA), secondary separation line (SS) and secondary attachment line (SA). In between the secondary separation and attachment lines there are tertiary separation (TS) and attachment (TA) lines over a limited axial extent associated with the tertiary flow observed in Figure 8b. In this case the primary attachment line (PA) is observed to be outboard of the symmetry plane. Inboard of this attachment line the limiting streamlines are approximately aligned with the freestream direction. This differs from what has normally been observed for high sweep delta wings where the attachment line coincides with the symmetry plane. With increasing angle of attack the primary attachment line moves inboard and the region between the primary attachment line and the secondary separation line expands. Experimental oil flow patterns obtained by Taylor and Gursul [30] show a similar surface streamline pattern, Figure 9.

2.2. Shear layer instabilities

The mean vortical flow structure described in the previous section results from an unsteady vortical flow that becomes progressively more complex with increasing angle of attack. Figure 10 displays an isosurface of axial vorticity for α=15° from Reference [16] to visualize this unsteady flow. At upstream locations a series of vortical substructures can be observed in the outer shear layer that rolls up to form the primary vortex. These vortices form in the shear layer that emanates from the leading edge. Subsequently, they are shed and convect downstream and around the primary vortex. These shear-layer features surround a distinct vortex core visible interior to the shear layer at upstream locations. Downstream this distinct vortex system breaks up into a collection of very fine scale structures.

In this section we will concentrate on the unsteady flow features upstream of vortex breakdown. Contours of the axial component of vorticity are plotted at an upstream location in Figure 11a. One of the vortical structures that form in the shear-layer that emanates from the leading edge of the delta wing and is subsequently shed can be clearly distinguished in Figure 11a. Accompanying this shear-layer instability is a significant unsteady behavior of the secondary flow with vorticity of the opposite sign being ejected from the surface and wrapped into the primary vortex. This eruptive response of the secondary flow, Figure 11a, results from the interaction of the leading-edge vortex with the surface boundary layer flow. The unsteady formation and shedding of these vortical structures and their close link to the boundary layer eruptive behavior induced by the vortex/surface interaction has been described in detail previously [21, 32, 33, 34] for higher sweep delta wings.

This unsteady behavior of the shear layer and secondary flow leads to a significant wandering of the vortex core around a mean core location. The vortex core moves in an oval

pattern with the same sense of rotation as the swirl of the vortex. This unsteady motion of the vortex core results in high values of the fluctuating kinetic energy, k, in the vortex core upstream of vortex breakdown, Figure 11b. High levels of fluctuating kinetic energy are also present in the shear layer and where the secondary flow eruption process occurs.

Experimental evidence for these types of shear-layer instabilities on low sweep delta wings [Λ=45° and Λ=60°] was first reported by Gad-el-Hak and Blackwelder [35]. They observed in flow visualizations at low Reynolds number that the vortex sheet emanating from the leading edge rolls up periodically into discrete vortical sub-structures. They attributed this phenomenon to the inviscid Kelvin-Helmholtz type instability of the shear layer. In more recent experimental measurements for a Λ=38.7° wing, Yavuz et al [36] show regions of average vorticity exhibiting well-defined concentrations of like sign along the leading edge which are also distinguishable in instantaneous images of the flow, Figure 12. They state that these features indicate the existence of a co-rotating pattern of small scale vorticity concentrations. Measurements of the root-mean square velocity, Figure 12, indicate that substantial fluctuations occur in this leading edge region. Yavuz et al [36] indicate that further investigation is required to determine the exact physical origin of these ordered patterns of vorticity observed in the leading-edge region.

2.3. Vortex breakdown

A common means used to study vortex breakdown over delta wings has been to visualize streaklines by releasing smoke or dye in the vortex core upstream of vortex breakdown. This technique has been very successful in displaying the distinctive character of the spiral vortex breakdown [37, 38] that occur over slender delta wings. For low sweep wings, however,

additional challenges in interpreting these streakline visualizations exist due to the nature of the vortex breakdown flow. Figure 13 compares the experimentally observed streakline visualization [31] for a Λ=39° wing at α=7° with the numerical equivalent of the streakline visualization for a Λ=50° wing at α=15°. Both the experiments and computations show very similar structures. The flow structure observed exhibit distinct differences from the classic flow visualizations of spiral vortex breakdown for high sweep wings. In each case the streakline initially remains straight. Yaniktepe and Rockwell [31] then identify three distinct stages in the breakdown process. In region I small scale undulations of the vortex core filament are evident. Gordnier and Visbal [16] point out that this spiralling is associated with the vortex core motion driven by the shear layer instabilities and not with the onset of vortex breakdown. Therefore, the initiation of spiraling of the streakline may not be used to identify the onset of vortex breakdown. The beginning of region II marks the location of the onset of vortex breakdown. Region II is characterized by a small scale bubble or thickening of the vortex filament which is terminated at its downstream end by a pinch off region where the diameter again becomes small. This is followed in region III by an abrupt expansion of the breakdown region where the particles are diffused over a broad area covering the outboard half of the wing.

Both Ol and Gharib [11] and Taylor et al [15] have reported from their flow visualizations that the vortex breakdown location shows significant fluctuations in the streamwise direction. For some cases fluctuations of 40% to 50% of the chord of the wing were observed. This is in contrast to more slender wings where fluctuations of the order of 10% of the chord length have been reported [39]. Ol and Gharib [11] noted that for certain cases in the angle of attack range α=12.5° to 17.5° the right and left vortices actually disintegrate and reform on a quasi-alternating basis. These large scale streamwise excursions of the vortex breakdown

location were not observed in the computations of Gordnier and Visbal [16]. This may be attributable to the symmetry boundary condition imposed in the computations.

The structure of vortex breakdown over a 50° sweep delta wing has been studied in greater detail both computationally [16] and by PIV measurements [11, 15, 30, 40]. The impact of vortex breakdown on the mean flow structure at α=15° can be seen in Figures 8a and 9. The high suction peaks obtained at upstream locations are lost further downstream, Figure 9. This loss in suction peak corresponds to progressively smaller values of maximum axial vorticity in the vortex core for downstream locations, Figure 8a. In addition, the core of the primary vortex becomes more diffuse and increases in size. This change in character of the vortex is seen more clearly by comparing the mean vortex structure for axial locations upstream and downstream of breakdown, Figures 8b and c respectively.

The onset of vortex breakdown can be more clearly seen by examining the vortex structure on a vertical plane through the vortex core. Figure 14 displays contours of the mean axial velocity for α=5°–15°. At the higher angles of attack, Figures 14a, b, a jet-like velocity is observed in the core of the vortex for upstream locations. This is similar to vortices over slender delta wings at angle of attack, which exhibit a strong vortex core jet. To further examine this behavior the mean axial velocity profiles across the vortex core at x/c=0.3 are plotted in Figure 5. As noted previously, at the lowest angle of attack, α=5° a broad wake-like flow is obtained throughout the whole vortex region, Figure 14c. As the angle of attack is increased, jet-like velocities are obtained with the peak velocity in the core increasing from a value U_{core}/U_{∞}=1.48 at α=10° to U_{core}/U_{∞} =1.99 for the 15° case.

Over a limited region in the axial direction a transition from a jet-like to a wake-like flow occurs for the 10° and 15° cases, Figure 14a, b. This switch from a jet-like to a wake-like flow is

indicative of the onset of vortex breakdown (see for instance Rockwell [3] and Visbal [4]). In neither case is an actual reversal of the mean axial flow achieved as is seen in the more slender wing case. The onset of breakdown is also much less abrupt for the low sweep case with the core expanding in a shallow, conical fashion. Due to these features of the low-sweep wing case, it becomes much more difficult to define an exact location of vortex breakdown as done in the high sweep case. Instead, by examining Figure 14 a region over which vortex breakdown occurs can be defined. For α=10° this region extends from x/c=0.49 to x/c=0.7. The vortex breakdown region is located further upstream for α=15° from x/c=0.4 to x/c=0.54. Although not shown here, associated with this change from a jet to wake profile is a switch in the sign of azimuthal vorticity [16] which is also characteristic of vortex breakdown [41].

PIV measurements [30] exhibit the same basic features for the breakdown structure. Figure 15 compares the computed velocity magnitude with the experimental measurements for α=15°. Contours of the inplane velocity magnitude are plotted on a plane through the vortex core that forms an angle ϕ= 6° with the delta wing surface. The computational results agree well with the experimental measurements with the vortex breakdown located only slightly further upstream in the experiment. In both the experiment and computation the switch from jet-like flow upstream of breakdown to wake-like flow downstream of breakdown can again be clearly seen.

As noted previously the mean vortical flow structure results from a very complex, unsteady flow. The unsteady structure of vortex breakdown is seen in Figure 16a where the coherent vortex core upstream of breakdown disintegrates into fine-scale, unsteady structures downstream. The breakdown of the coherent vortex core into finer scales is also evident in a plane normal to the vortex core, Figure 11c. At this location the whole vortex system has broken down into a large number of small, highly unsteady flow features. Only a large region of

vortical flow made up of small scale structures can be distinguished with no clear vortex core discernable. Also a distinct secondary flow region cannot be defined, though pockets of vorticity of the opposite sign exist. Spectral analysis of the pressure fluctuations at the location noted in Figure 13 shows a broad frequency distribution ranging from St=0 to St=5.0 with a peak Strouhal number, St ≈ 2.8. This value is similar to the measurements [31] for a Λ=38.7° sweep where a St ≈ 3.3 was measured.

In Figure 16b, there is again a switch from a jet-like flow in the core upstream of breakdown to a wake-like flow in the breakdown region. In contrast to the mean flow, however, small pockets of reversed axial flow (highlighted by white zero velocity contour lines) exist in the breakdown region. The resulting levels of fluctuating kinetic energy in the vortex core plane are seen in Figure 16c. The small-scale unsteady flow features of breakdown result in a broad region of fluctuating kinetic energy, Figures 11d and 16c. Note that these levels are less than the values associated with the vortex wandering upstream of breakdown.

2.4. Shear layer reattachment and stall

As noted earlier one of the distinct features of the low sweep flow structure is the attachment of the shear layer inboard of the symmetry plane. Taylor and Gursul [30] explored in more detail this reattachment process for a 50° sweep delta wing using PIV measurements in a plane parallel and very close to the wing surface for α=10° to α=25°. Figure 17 shows the streamline pattern and the magnitude of the rms velocity near the surface. For α=10° the footprint of the vortex is bounded by the shear layer attachment line to the inboard side and the secondary separation line to the outboard side. Increasing incidence moves the primary reattachment line inboard towards the wing centerline. Figure 18 shows the inboard progression

of the attachment line for both wind tunnel and water channel cases [30]. In both cases, the attachment line moves towards the centerline until it finally reaches the centerline near the onset of stall $\alpha \approx$ 22-23°. At the largest angle of attack, $\alpha = 25°$, the wing has stalled and the streamline pattern takes the form described in previous research [8] as a 'whorl'.

At the lower angle of attack, Figure 17, a region of high rms velocity lies underneath the path of the vortex. Downstream of breakdown this region of high rms velocity kinks and widens. The maximum velocity fluctuations at α=15° occur just underneath the vortex axis after the point of breakdown. By α=20° the vortex breakdown has reached the apex and the nature of the fluctuations changes. The largest fluctuations are now observed near the wing centreline in the region of the apex and just outboard along the attachment line. This region of large fluctuations associated with the attachment of the shear layer provides an additional source of buffeting for nonslender delta wings. This is in agreement with previous findings of Honkan and Andreopoulos [42] who reported that the shear layer reattachment zone is associated with high-turbulence activity. By α=25° flow has become completely stalled with very low time-averaged velocities and velocity fluctuations near the wing surface.

As discussed above, the primary attachment region is characterized by high unsteadiness at high angles of attack before complete stall takes place. Spectral analysis of the velocity fluctuations near the surface [30] and of the surface pressure fluctuations [43, 44, 45] showed dominant frequencies in the range of fc/U_∞= 1 to 2 for low sweep wings with Λ=40° and 50°.

2.5. Effect of Reynolds number

Some of the features of the low sweep delta wing flow described here show sensitivity to Reynolds number, particularly for the lower Reynolds numbers that were investigated. This low

Reynolds number range is important for applications related to MAVs. Figure 19 shows the impact of Reynolds number on the development of the vortical flow and dual vortex structure in the computations of Gordnier and Visbal [16]. Figures 19a-c present computed solutions for Reynolds numbers 10,000, 20,000 and 50,000, respectively. The flow at the lowest Reynolds number, Re=10,000, exhibits a strong viscous influence. Only a thick separated shear layer is seen with no discernible vortex structure present. As the Reynolds number is increased to Re=20,000, the influence of viscosity is reduced and a clear dual vortex structure develops. Increasing Reynolds number to 50,000, results in a further strengthening of these vortices. Downstream of the present location at this higher Reynolds number, the flow becomes highly unsteady due to the transitional nature of the separated shear layer.

The influence of viscosity on the vortex structure at very low Reynolds numbers can also be seen in the measurements [11] for a 50° sweep delta wing at Re=8500. In that study, wake profiles were measured for all angles of attack (α=5° to α= 20°), including angles for which vortex breakdown was downstream of the measurement location and a jet-like flow might be expected (e.g. α=10°). This is in contrast to the computations [16] for a similar 50° sweep wing with Re=26,000 which showed jet-like velocity profiles through the core of the vortex except at the lowest angle of attack, α=5°, Figure 5. To investigate this difference a computation was performed for α=15° and a Reynolds number, Re=8500. The computed velocity profile for this case, Figure 5, is comparable to the measurements of Ol and Gharib [11] with a shallow wake associated with the intact primary vortex core. A much more significant wake is associated with the large secondary flow near y/y_{le}=0.8. These computations indicate that at very low Reynolds numbers or low angles of attack wake-like flows can exist in the vortex core even upstream of

breakdown for low sweep delta wings. At higher angles of attack and more typical Reynolds number the more standard jet-like flow is recovered.

The primary vortex core location has also shown sensitivity to Reynolds number. Taylor and Gursul [30] showed that the trajectory of the vortex core shifted inboard towards the centreline as the Reynolds number is reduced. Figure 20 shows the variation of the spanwise location of the primary vortex core with Reynolds number. Comparisons of the measurements are made with other data presented in the literature [10, 11, 16]. At higher Reynolds numbers (on the order of 30,000) the flow approaches an asymptotic state, with further increases in Reynolds number resulting in only small variations in the location of the vortex core. There appears to be a strong dependence of the vortex trajectory on incidence at very low Reynolds numbers and a degree of scatter exists in the data indicating that the measured results may be sensitive to small changes in the experimental set-up or measurement technique. At higher Reynolds numbers this sensitivity of vortex trajectory to angle of attack decreases, which is consistent with the inviscid theory of Moore and Pullin [46]. All of these results suggest that care must be taken when trying to extrapolate the vortical flow structure found at very low Reynolds numbers to higher Reynolds numbers.

The Reynolds number dependence of the multiple vortices and their interactions on a generic UCAV configuration was reported by Elkhoury and Rockwell [47] for $Re \leq 40{,}000$. It was shown that the sensitivity of vortex breakdown is much larger at low angles of attack when the vortex system resides closer to the wing. Furthermore, multiple vortex interactions also display marked dependence on Reynolds number. This is more apparent a low incidences and decreases with increasing angle of attack.

2.6. Effect of leading edge shape

The basic features of the flow for sharp leading-edges described here are strongly affected by the leading-edge shape. Realistic configurations will have round leading-edges, and this affects not only the flow separation characteristics, but also the primary attachment location. Figure 21 shows the location of the attachment line for various leading-edge shapes [48] for Λ=50° wings with thickness/chord ratio of 4%. It is seen that for all rounded edges the reattachment line is more outboard for any given angle of attack, which indicates a delay in the stall. Indeed, the measured lift coefficients [48] exhibit substantial delays, as shown in Figure 22. At first sight, this seems logical, given that nonslender wings are closer to two-dimensional airfoils, which are well-known for their sensitivity to flow separation at the leading-edge and resulting stall. However, in the case of nonslender delta wings, the stall is related to the reattachment process, although the origin of the separated shear layer is likely to be affected by the leading-edge separation. For a sweep angle of 45°, Kawazoe et al [49] also showed that the stall is delayed for rounded leading-edge, and this was due to the primary attachment line reaching the wing centerline at a larger angle of attack.

Miau et al [10] showed for Λ=50° wings with various leading-edge shapes that the flow separation and formation of the leading-edge vortices were strongly affected by leading-edge shape. However, their experiments were conducted at a low Reynolds number (Re=7,000), where viscous effects are dominant. Force measurements at much higher Reynolds numbers (shown in Figure 22) indicate that effects in the pre-stall region are small.

For slender wings, the leading-edge profile strongly affects the location of vortex breakdown, but lift is weakly influenced [50]. While there is virtually no change in stall angle

for slender wings, the effect for nonslender wings is substantial. Also, rounded leading-edges result in generally milder stall.

3. Fluid/structure interactions

The vortical flow over a low sweep delta wing described in the previous section became increasingly unsteady as the angle of attack of the wing increased. Sources of this unsteadiness included shear layer instabilities and vortex breakdown. Menke et al [22] have shown that there are a variety of unsteady phenomena that occur over slender delta wings, Figure 23, and the characteristic time scales of these phenomena differ by several orders of magnitude. These highly unsteady vortical flows can lead to buffeting of flexible delta wings due to the fluctuating loads on the surface of the wing.

3.1. Buffeting of wings with moderate sweep angle

Gray et al [51] have investigated the buffet response of a moderately swept, Λ=60°, aluminium delta wing over a variety of flow regimes by varying the angle of attack from 0° to 50°. In their experiments both a half-wing and full-wing model were investigated. Gordnier and Visbal [52] have performed corresponding computational simulations for the half-wing model using the inviscid Euler equations to simulate the aerodynamics and a finite element von Karman plate model for the structures.

The buffeting response of the delta wing as indicated by the rms acceleration at the wing tip is plotted as a function of angle of attack in Figure 24 for both the experiment and the computations. Good qualitative agreement is seen between the experimentally measured response and the computations. A number of factors contribute to the quantitative discrepancies

in the rms response including, structural damping, wind tunnel wall influences and unsteady viscous effects not captured by the inviscid Euler computations. As described by Gray et al. [51], a rapid increase in the buffet response of the wing occurs as vortex breakdown moves over the wing between α=5° and 22.5°. As the breakdown approaches the apex of the wing the rms acceleration reaches its maximum values for α=22.5°-27.5°. When the vortex breakdown reaches the apex of the wing and the onset of wing stall occurs, α=27.5°–40°, the level of buffeting reduces rapidly.

To better understand the buffeting response of the wing both the mean deflections and the unsteady fluctuations were studied. Figure 25 shows how the mean wingtip deflection varies as a function of angle of attack for the computations [52]. The mean deflection continually rises as angle of attack is increased up to α=35°. At α=40° a drop in the mean deflection occurs. This decrease in the deflection results from the loss of additional suction from the vortical flow with the onset of full stall over the wing for $\alpha \geq 35°$. The mean deflection of the wing is primarily a first mode bending (see insert Figure 25). Spectral analysis of the computed wingtip fluctuations exhibited a dominant peak at St=0.606 or 40.4 Hz which corresponds to the frequency of the first structural mode.

Spectral analysis of the wingtip acceleration was also carried out for both the experiment and the computation. Figure 26 displays the experimental [51] spectral analysis which shows large peaks at the frequencies corresponding to the second and third structural modes with somewhat smaller peaks at the first and higher modes. The computations showed similar behaviour albeit with somewhat higher peaks associated with the first structural mode. These results indicate that most of the energy is in the second and third modes of vibration when vortex breakdown is over the wing.

The reasons for the response of the wing in the second and third structural modes can be better understood by looking at the spectral analysis of the unsteady pressure fluctuations at an axial location x/c=0.5, Figure 27. The spectrum is characterized by a broadband frequency range from St=1.6 to St=3.6 with the maximum amplitude at a frequency St=2.14. These pressure fluctuations result from the strong interaction of the vortex breakdown with the wing surface and excite the buffet response of the first three modes of the delta wing. In particular, the frequencies of the second and third modes lie directly in the broadband frequency range of the pressure fluctuations giving rise to the additional second and third mode response of the delta wing.

Gray et al [51] also performed experiments for a full-span delta wing model. The variation in the rms wingtip acceleration with incidence for the full model was virtually the same as the half-model with no difference in the rms accelerations of the right and left side. Adoption of the full model introduces the possibility of exciting antisymmetric modes of vibration. Figure 28 shows the results of the spectral analysis for the full model. In this case the dominant mode is the second antisymmetric mode with the maximum response again occurring when the vortex breakdown is over the wing. The dominance of the second antisymmetric mode suggests that the antisymmetric axial motion of the vortex breakdown location reported by Menke et al [22] for slender delta wings may also be coupling with the structural motion in this situation.

3.2. Buffeting of wings with low sweep angle

Taylor and Gursul [40] have repeated their experiments for a low sweep wing, Λ=50°. The variation in the wing tip rms acceleration with angle of attack, Figure 29 is qualitatively similar to the Λ=60° wing. Buffeting at low levels of incidence is small and similar to the

magnitude measured for the 60° sweep wing with the same thickness and span. There is a moderate increase in the buffeting response up to $\alpha \approx 7°$, followed by a significant increase thereafter. A maximum value of rms acceleration that is slightly lower than the $\Lambda=60°$ case is obtained around $\alpha=19°$. This is followed by a rapid decrease in the vibration of the wingtip for angles of attack beyond $\alpha=21°$. This rapid decline in the buffet level is again associated with the onset of stall.

Taylor and Gursul [40] note that maximum buffeting of the $\Lambda=50°$ wing occurs prior to stall in a region where vortex breakdown reaches the apex of the wing. It was pointed out in Section 2.4, Figure 17, that at an angle of attack $\alpha=20°$ which is in the range where the maximum buffet is occurring, the largest flow fluctuations are found in the shear layer reattachment zone. Taylor and Gursul [40] suggest that this unsteadiness associated with the shear layer reattachment may be an important source of buffeting in this angle of attack range where vortex breakdown has reached the apex of the wing.

3.3. Aeroelastic instabilities

The previous discussion has focused on the buffeting response of the delta wing due to the unsteady aerodynamic forces resulting from the vortical flows and vortex breakdown. Delta wings in general and more specifically low sweep delta wings are also subject to the aeroelastic instabilities of flutter or limit cycle oscillations (LCO). Doggett and Soistmann [53] investigated experimentally and analytically the onset of flutter for a range of delta wing sweep angles from 30° to 72°. Their results showed that the flutter speed index decreases with increasing sweep angle or with an increase in the percentage of the root chord that is clamped.

More extensive experimental and analytical investigations of the flutter characteristics of nonslender delta wings at small angles of attack have been performed by Tang et al [54, 55] and Attar et al [56-58]. In these investigations a series of aeroelastic models of increasing fidelity in both the aerodynamics and structures were implemented. In the initial work of Tang et al [54], a linear vortex lattice model was coupled with a nonlinear von Karman plate model. Attar et al extended this model by replacing the linear vortex lattice model with a nonlinear vortex lattice model [56] and by replacing the von Karman model with a high fidelity structural model which accounts for geometric nonlinearities resulting from large deflections or rotations [58]. These computations and experiments showed that for the delta wings considered, limit cycle oscillations (limited amplitude fluctuations) occur after the onset of flutter. It is demonstrated that the geometric nonlinearity in the structural model is the mechanism for the development of the limit cycle oscillations for this type of plate like delta wing. Small changes in angle of attack were shown to have only a limited impact on the flutter speed and frequency [57, 58]. Attar et al [58] also showed that proper modelling of the geometric nonlinearities for moderate to large deflections is critical for capturing the correct LCO behaviour.

Gordnier and Melville [59] and Attar and Gordnier [60] have applied an aeroelastic solver that couples a Navier-Stokes/Euler code with either a von Karman plate model or a high-fidelity finite element model based on a co-rotational formulation to simulate limit cycle oscillations of a cropped, Λ=47.8° sweep delta wing. These computations captured the limit cycle response of the wing observed in the experiments of Schairer and Hand [61]. Structural nonlinearities were shown to provide the correct nonlinear mechanism for the development of limit cycle oscillations even in the transonic Mach number range considered in this problem. Attar and Gordnier [60] also demonstrated the importance of modelling both the fluid and

structural problems with high accuracy so that lower fidelity modelling in either discipline does not cause important physics to be missed resulting in inaccurate solutions to the coupled fluid/structure system.

4. Lift enhancement on flexible wings

It is seen in the previous section that wing flexibility may couple with vortical flow. When the flexibility is increased further, it has been found that a nonslender wing with Λ=50° exhibits lift enhancement [62], which can be regarded as a passive flow control method. This spectacular enhancement is observed when the wing flexibility reaches a minimum threshold value. It has been shown that for a wing of thickness, t/c = 0.32% at a Reynolds number, Re = $6.2*10^5$, a region of significant lift enhancement exists in the range of incidences immediately following the stall. An increase in time-averaged lift coefficient of up to 45%, and a delay in stall of up to 9° have been observed. Time-averaged drag also increases in this region, resulting in no noticeable change in lift/drag ratio [63]. Further experiments with various sweep angles have confirmed that this lift enhancement is always confined to the post-stall region of the rigid wings [64].

4.1. Effect of wing sweep

Figure 30 shows the variation of lift coefficient for rigid and flexible wings [64] with sweep angles Λ=40°, 45°, 50°, 55°, and 60°. The wing with Λ=60° can be regarded as a transition between the slender and nonslender wings. All wings had the same span, but different chord length (hence different Reynolds numbers, but this is not a factor in the range Re=440,000 – 900,000, as the sensitive range is below 30,000). All the flexible wings had the same thickness

(t/s = 0.38%). The parameter λ_s, the reciprocal of the spanwise bending stiffness of the wing normalized by the free-stream dynamic pressure, was used to give an indication of the relative flexibility of the wings, whereby a higher value of λ_s corresponds to a more flexible wing. The definition of λ_s is given by $\lambda_s=12(1-\nu^2)\rho_\infty U_\infty^2 s^3/Et^3$, where E is elastic modulus, ν Poisson's ratio, s semi-span, and t thickness of the wing. For the conditions in Figure 30, the nondimensional spanwise bending stiffness was $\lambda_s = 3.1$ for the flexible wings of all sweep angles, compared with a value of $\lambda_s = 0.025$ for the rigid wings.

Figure 30 shows that the lift enhancement phenomenon is not limited to wings of 50° leading edge sweep; rather, wing flexibility results in a region of enhanced lift for all wings except the 60° wing. The magnitude and extent of the lift enhancement region was a function of sweep angle, with the greatest enhancement being observed over the wing of lowest sweep. The 40° wing improved the maximum lift coefficient by over 40%, and at the point of stall of the flexible wing, lift coefficient was enhanced by over 50%. As sweep angle was increased the magnitude of the lift enhancement reduced, with the overall maximum lift coefficient of the 55° wing increased by just 1%, while the 60° wing experienced an overall reduction in lift. For all the wings, the nose-down pitching moment measured about the apex underwent a similar magnitude increase in the lift enhancement region.

Since no lift enhancement was observed for Λ=60°, this feature appears to be limited to flexible low-sweep wings. A unique feature of the flow structure on nonslender wings is that the vortex and primary attachment zone are located further outboard from the wing centerline. This characterstic may be responsible for the increased impact of wing flexibility on the aerodynamic loading.

There is evidence that similar lift enhancement on flexible wings of different shape is possible for low-aspect ratio wings. Figure 31 shows a MAV with a membrane wing, which exhibits similar lift enhancement relative to a rigid one [65]. Again, the lift enhancement is observed in the post-stall region, increasing the maximum lift and delaying the stall. Separated and vortical flows are common over low-aspect-ratio wings, in particular at low Reynolds numbers [66]. Tip vortices contribute to lift, and affect the majority of the wing surface [67]. Torres and Mueller [68] present the variation of lift coefficient with angle of attack for flat-plate wings with an elliptical planform, and show that the AR=1 wing produces monotonically increasing lift coefficient with incidence, very much like a thin delta wing. Hence, wing flexibility might be beneficial for a variety of low-aspect ratio wings, not just delta wings.

4.2. Self-excited antisymmetric vibrations

Due to the degree of flexibility employed in these experiments [64], considerable time-averaged and fluctuating displacements were observed. For the wings of 40°, 50° and 60° sweep, the variation of mean and peak-to-peak amplitude of wing-tip displacement with incidence is shown in Figure 32. For the 40° and 50° wings the lift enhancement region was accompanied by an increase in both the amplitude and, to a lesser extent, mean (time-averaged) tip deflection. For the 60° wing, which did not experience an increase in lift, no such discontinuity in the displacement curves was observed. In fact, it is clear that the 60° wing experiences much less vibrations than the lower sweep wings, although the maximum mean deflection is greater. Although the wings were designed to have identical values of λ_s, and therefore equivalent bending stiffness, the chord lengths of the wings are not equal resulting in a lower thickness-to-chord ratio for the 60° wing, and this probably accounts for the greater mean

deflection for this wing. This result confirms that mean deflection alone does not cause lift enhancement phenomena. In an earlier experiment [62], a rigid wing model (with 50 degree sweep angle) was given a spanwise dihedral camber of a form such that its cross-section approximately corresponded to the time-averaged deformation of the flexible wing during testing. The results showed that there was no lift enhancement due to static spanwise camber. All this evidence indicates that vibrations of the leading-edges are essential in delaying stall and increasing lift.

The fluctuations of the lift force [64] are not much different for the flexible and rigid wings, indicating that the wing vibrations do not necessarily cause large unsteadiness in lift. This is not surprising, as the lift enhancement appears to be related to the reattachment process. This is also important, as it signifies that the lift improvements can be achieved without the imposing high lift force fluctuations. On the other hand, the fluctuations of the rolling moment are strongly affected by wing flexibility. Figure 33 shows the variation of root-mean-square (RMS) of the rolling moment coefficient with incidence for three sweep angles. While there is virtually zero rolling moment for the rigid wings, for all the wings that experienced a lift enhancement, a significant increase in RMS rolling moment was observed in the lift enhancement region for the flexible wing. This is consistent with the initial observations in Reference 62 in that the wings vibrate in an anti-symmetric mode in the lift-enhancement region. The resulting unsteady rolling moment has a frequency corresponding to Strouhal number on the order of unity, which is much higher than the natural frequencies of real aircraft in roll motion.

The dominant frequency of the measured wing tip acceleration, predictions of the natural frequencies by finite element analysis, and visualization of the wing deformation reveal that wing vibrations switch to an anti-symmetric structural mode in the lift enhancement region.

Simultaneous measurements of both wing tip accelerations were also conducted for a 50° sweep wing. The spectral characteristics of the wing tip vibrations are summarized in Figure 34, which shows the variation of cross-spectral amplitude and phase angle between the wing-tip accelerations as a function of normalized frequency and incidence. Considering first the variation of cross-spectral amplitude, a dominant peak at St = 0.7 in the lift enhancement region should be immediately noted. Compared with this peak, other seemingly dominant frequencies are actually very small; note that the contour scale is logarithmic. Thus, in the region of enhanced lift, the wing experiences large wing-tip vibrations of a dominant frequency of St = 0.7. Furthermore, the phase map shown in Figure 34 shows that the wing-tip vibrations are out of phase at this frequency, indicating an anti-symmetric mode shape. Visualization of the deformation of the leading edge confirmed the mode shape as the second anti-symmetric mode.

The question as to whether or not an anti-symmetric vibration of the wing is a necessary condition for the production of additional lift is an important one. In order to answer this question, experiments for a half-wing model were conducted. Figure 35 shows the variation of wing-tip RMS acceleration with incidence for a half-wing 50° flexible model, and compares this with the full wing case. It is seen that the half-wing does not exhibit large self-excited vibrations in the post-stall region. This suggests that anti-symmetric vibration is essential for lift enhancement.

4.3. Flow reattachment

Self-induced vibrations excite the shear layer by energizing the shed vortices and promote vortex reformation which is accompanied by the reemergence of the attachment zone. Figure 36 shows tuft visualizations of the surface flow at $\alpha = 27°$ for the rigid and flexible wings

with 50° sweep angle. For the rigid wing, stalled flow is evident and large-scale unsteadiness was observed in the real-time video footage. For the flexible wing, however, a partially attached flow is observed. Although the large regions of reversed flow are also observed in this case, the flow is clearly energized at this incidence. Although flow reversal was still a feature of the flow towards the leading edges, the flow was much less unsteady.

In addition to the flow visualization with tufts, PIV measurements of the near-surface flow were undertaken for the rigid 50° wing at $\alpha = 27°$. Figure 37 shows the streamlines of the time-averaged flow, calculated from the velocity vectors, which confirms that the flow over the rigid wing at this high incidence is completely stalled, with maximum velocities near the wing surface of around $u/U_\infty = 0.3$ in the flow reversal region near the leading edges. The flow towards the centerline is devoid of the high axial velocities that are associated with shear layer reattachment. Figure 37 also shows the streamline pattern for the flexible wing at the same incidence. Contrary to the streamlines over the rigid wing, the flexible wing demonstrates a symmetrical time-averaged flow. Significant regions of flow reversal are observed over the wing, with high negative axial velocities peaking at $u/U_\infty = -0.38$. Along the centerline, high positive axial velocities are observed, peaking at around $u/U_\infty = 0.67$. A node exists on the centerline at around $x/c = 0.2$, and all surface streamlines on the wing issue from this node, indicating that it is a node of attachment.

Figure 37 therefore shows that the flow over the flexible wing is much more coherent than that over the rigid wing at the same incidence. For the flexible wing, shear layer reattachment is observed, extending the region of partially attached flow at high incidences. The main mechanism for lift enhancement is related to the excitation of the shear layer instabilities. For $\Lambda = 50°$ wing, the dominant frequency of structural vibration was around $St = 0.75$, which

compares well with the dominant frequencies of the shear layer instabilities [30]. Note that this range of natural frequencies of shear layer is much lower than those for slender wings [21, 24]. The self-induced vibrations of the wing energize the vortices shed into the shear layer and promote reattachment to the wing surface, resulting in delayed stall and increased lift. This is similar to the response of the flow over a backward-facing step to the periodic excitation. It is well known that, for both laminar and turbulent separation [69], excitation enhances the formation of vortical structures and substantially reduces reattachment length.

In addition to vibration of a flexible wing (which is a passive method), shear layer excitation with active control methods may also have substantial effects on the flow. Cipolla and Rockwell [70] studied the effect of a periodic pitching oscillation on a stalled 45° wing. For pitching frequencies in the range $0.5 < St < 1.0$, the extent of the stall region was decreased compared to the stationary wing at the same angle of attack (α=30°). For a higher sweep angle, Gad-el-Hak and Blackwelder [71] studied the effect of periodic tangential blowing along the leading edge of a 60° delta wing. The results showed that by blowing at a frequency of approximately half the natural shedding frequency, the cross-flow structure of the primary vortex could be made to be more organized. Margalit *et al* [72] investigated the use of oscillatory blowing along the leading edges of a 60° sweep delta wing. Significantly, lift enhancements of around 15% were exhibited for forcing frequencies in the range $1.0 < St < 4.0$. Further, these lift enhancements were observed in the post-stall region between α = 35 and 40°. The effect of shear layer excitation for slender wings [73, 74] is not clear. Recent PIV measurements involving oscillatory forcing of a 70° wing have shown that forcing of the shear layer in the region upstream of breakdown had no beneficial effect on the vortex structure, and only served to alter the trajectory of the primary vortex. However, experiments using periodic blowing have

demonstrated lift enhancement over a 70° wing in the range $34° < \alpha < 40°$ for a forcing frequency of St = 1.75.

Returning to the shear layer reattachment for flexible delta wings, in the experiments reported in [62] and [64], there was no evidence of streamwise flow forming within the reattached region. Figure 38 shows the results of LDV measurements of the chordwise velocity field in the cross-flow plane at x/c = 0.4 for the (a) rigid and (b) flexible 50° wings at $\alpha = 25°$. For the rigid wing, the flow is much more symmetric and coherent than suggested by the PIV measurements presented earlier for $\alpha = 27°$. The data show a large region of reversed flow extending well above the surface of the wing, but a region of high axial velocity remains along the centerline, albeit at a considerable distance from the wing surface. The chordwise velocity field over the flexible wing shares many similarities with that of the rigid wing. Again, a region of reversed flow extending well above the wing surface is evident along with a region of high axial velocity above the surface near the centerline. However, the region of flow reversal is reduced in extent and appears flatter than for the rigid wing, while the region of high axial velocity above the centre-line is larger and extends closer to the wing surface. In general, the flexible wing exhibits much higher axial velocities towards the wing surface than the rigid wing does.

With increasing flexibility, there is evidence of a change in the structure of the flow and streamwise flow develops within the reattached region. The water tunnel experiments [75] show that, for large values of λ_s, the leading-edge vortex re-forms and vortex breakdown occurs very close to the apex, as seen in the flow visualization pictures in Figure 39. This is somewhat unexpected in that the flexibility not only promotes earlier reattachment but also helps re-formation of the leading-edge vortices. Corresponding vorticity distributions in a cross-flow

plane at x/c=0.8 are shown in Figure 40 for α=20°. There are substantial effects on the vortical flow with increasing wing flexibility, as the oscillating leading edge is an unsteady source of vorticity. In fact, the time-averaged vorticity flux is expected to increase with the vibrations of the leading-edge, as this term is proportional to $\overline{U_s^2}$, where U_s denotes the velocity outside the boundary layer at the separation point. This is confirmed by the larger values of vorticity for the flexible wings in Figure 40. The variation of circulation with the spanwise bending stiffness normalized by free-stream dynamic pressure, λ_s, is shown in Figure 41. It is seen that the circulation of the vortical flow in a crossflow plane increases with flexibility in comparison to the rigid wing.

5. Nonslender delta wings undergoing small amplitude motion

5.1. Periodic roll oscillations

In order to simulate the effect of antisymmetric vibrations, experiments with a rigid wing undergoing small amplitude rolling motion were also conducted [75]. This approach has the advantage of independent control of the frequency parameter, which cannot be varied for a flexible wing without affecting the amplitude of vibrations. Figure 42 shows flow visualization for the stationary and rolling delta wing (with an amplitude of 5°) for an incidence of α = 25°. It is seen that the totally separated flow for the stationary wing becomes very organized for the rolling wing with increasing frequency. The most interesting observation is the re-formation of the leading edge vortices at high frequencies. Although the leading edge vortices become stronger due to the leading edge motion, vortex breakdown is delayed for the rolling wing compared to the stationary wing for which breakdown is at the apex. This appears to be in contrast to the well-known studies of vortex breakdown, which indicate that increased strength of

vortices should cause premature, rather than delayed, breakdown. This result suggests that streamwise pressure gradient might be modified favorably due to the wing motion.

Figure 43 shows the variation of mean breakdown location as a function of dimensionless frequency for different angles of attack in the range $\alpha = 20°$ to $30°$ in the post-stall region. It is seen that, for each incidence in the post-stall region, the breakdown location is zero for the stationary wing ($fc/U_\infty = 0$). Maximum delay of the vortex breakdown location is achieved in the range of $fc/U_\infty = 1$ to 2. Again, this range compares well with the dominant frequencies of the shear layer instabilities [30] for a nonslender wing of $\Lambda = 50°$. It was shown in Reference [75] for $\alpha = 25°$ that, even for a small amplitude of 1°, it is possible to have re-established leading edge vortices. The optimum dimensionless frequency is also in the same range.

In the case of the rigid wing undergoing small amplitude rolling motion, the dimensionless frequency fc/U_∞ is not only a ratio of time scales of convective time and rolling motion, but also the ratio of the leading edge velocity and freestream velocity for a given wing. Figure 43 suggests that increasing velocity of leading edge (with increasing frequency parameter) does not necessarily delay breakdown location. However, it is expected that the time-averaged vorticity flux will increase with increasing velocity of the leading edge. This is confirmed by the vorticity distributions in a cross-flow plane at $x/c = 0.80$ as shown in Figure 44 for $\alpha = 25°$. Note that the results shown in this figure are phase-averaged over 30 cycles, and correspond to zero roll angle as the roll angle changes the sign from negative to positive. This is the reason for the slight asymmetry, which is the result of the well-known hysteresis effect. It is seen that larger values of vorticity exist with increasing frequency. The variation of circulation with the dimensionless frequency is shown in Figure 45. It is seen that the circulation of the vortical flow in a crossflow plane increases with frequency in comparison to the stationary wing.

Further experiments for different sweep angles (not shown here) in the range Λ=30° to 50° indicated that the reattachment process is generic for all nonslender wings and there is an optimum frequency range of fc/U_∞ = 1 to 2. Exploitation of this result for low-aspect ratio wings, in the form of leading-edge vibrations, oscillatory blowing, or piezoelectric actuators should be beneficial.

5.2. Periodic pitch oscillations

One of the fundamental questions is whether the antisymmetric perturbations are necessary for the reattachment process in the post-stall region. The results for flexible wings discussed earlier suggest that anti-symmetric vibration is essential for lift enhancement. It was shown above that roll oscillations, which introduce antisymmetric perturbations, mimic the behaviour of the flow over the full flexible model. For the same configuration, the effects of pitch oscillations, which introduce symmetric perturbations, have been studied. Figure 46 shows the flow visualization pictures for various forcing frequencies for an amplitude of 1° pitching oscillations. It is seen that the same effects, including the reattachment of shear layers and vortex re-formation, are observed with increasing frequency. A direct comparison, of which forcing mechanism (symmetric versus antisymmetric) is more efficient, is not possible as the leading-edge velocity perturbations are vastly different in their geometric form. Nevertheless, the results show that symmetric perturbations also promote reattachment and vortex re-formation.

Yaniktepe and Rockwell [31] showed that, for even lower sweep angle of Λ=38.7°, the effect of small perturbations (1° pitching oscillations) is substantial as shown in Figure 47 for α=17°, which produces stalled flow for the stationary wing. The most effective frequency of

excitation (T=0.5) corresponded to the subharmonic of the broadband fluctuations in the region of the shear layer closest to the leading-edge in this case. The optimum period T=0.5, which corresponded to fc/U_∞=2.06, was also the smallest period of oscillations tested in these experiments. It is seen that forcing at this frequency produces a flow pattern characteristic of a typical leading-edge vortex.

For the same wing at a smaller angle of α=10°, the vortex breakdown is over the wing [36]. In this case, periodic pitching perturbations actually cause vortex breakdown to move upstream. However, it is still evident that the excitation causes earlier reattachment, as can be seen from the reattachment line moving outboard in the time-averaged streamline pattern near the wing surface.

6. Large amplitude maneuver of nonslender delta wings

Although there are a large number of studies on unsteady aerodynamics of maneuvering slender delta wings [24], very little is known about unsteady aerodynamics of nonslender wings. Recently, Cummings et al [76] conducted computational simulations and wind tunnel experiments for a pitching UCAV model. This configuration (Boeing 1301 UCAV, with Λ=50°) has a leading-edge vortex developing at α = 10°, in spite of the use of a rounded leading-edge. It was reported that the pitching characteristics are somewhat unusual in that the dynamic lift was actually much larger than that of the static case even for small incidences around zero angle of attack. This is in contrast with the results of slender delta wings [77, 78] for which increased dynamic lift is only observed in the post-stall region and there is virtually no difference between the static and dynamic cases up to the post-stall region. (The variation of dynamic lift is similar for slender delta wings and two-dimensional airfoils, although the flow physics are entirely

different). This difference for the nonslender UCAV was attributed to the leading-edge vortex in the dynamic case being stronger than the static case. Further studies are needed to shed light on this issue.

While the unsteady aerodynamics of rolling slender wings have been studied extensively (see, for example, [79]), there are not many studies on rolling nonslender wings. Previous studies on slender wings for static and forced rolling motions have revealed the existence of critical states [79] and the importance of vortex breakdown location [80, 81]. As the flow becomes asymmetrical, the strength of the vortex for each half of the wing is different as the effective sweep angle and incidence varies with the instantaneous roll angle. Experiments conducted for statically and dynamically rolled wings [82] show that the response of the vortical flow strongly depends on the angle of attack. For a wing with 50° leading edge sweep and at angle of attack $\alpha = 15°$, vortex breakdown was present over the wing at zero roll angle. However, its variation was little affected at static or dynamic roll angles, as seen in Figure 48. This insensitivity to roll angle is remarkable, and very much in contrast with slender wing vortices [83]. Vortex breakdown is highly sensitive to the variations in roll angle for slender delta wings.

The most drastic effects of roll angle occur around the stall angle. For $\alpha = 20°$, Figure 49 shows that vortex breakdown is at the apex of the wing at zero roll angle, but a coherent vortex is formed and breakdown is observed over the wing for large roll angles. Hence, partially attached flow on one side and completely stalled flow on the other side are simultaneously possible. In the dynamic case, even for small dimensionless frequencies, there were coherent leading-edge vortices on both sides of the wing throughout the whole cycle, rather than partially or completely stalled flow as in the static case. However, the variation of breakdown location over a cycle was

much smaller. When the dimensionless frequency of the rolling motion was substantially increased, the amplitude of cyclic variations in breakdown location decreased. In addition, hysteresis increased with increasing frequency, and was most noticeable at zero roll angle.

In Figure 50, vorticity in a crossflow plane at 80% of the chord length and at $\alpha = 20°$ at three instants over a cycle is presented for the quasi-static and dynamic cases ($fc/U_\infty = 0.15$). In this part of the cycle, the counter-clockwise vortex is much stronger for the dynamic case than for the static case. There is also evidence of multiple vortices of the same sign of vorticity at high roll angles in the dynamic case. Circulation of the vortices calculated as a line integral of velocity using PIV data is shown in Figure 51 for the countrer-clockwise vortex. It is seen that there is a large hysteresis loop and also the average circulation is higher in the dynamic case. The largest differences from the static case are observed for increasing roll angles. The increase in the time-averaged circulation is due to the increase in the time-averaged vorticity flux, which is a result of the oscillations of the leading edge. Comparison of Figures 49 and 51 shows that the variations in the breakdown locations are related to the variations in circulation, although the variations in the latter are relatively larger in the dynamic case. For increasing roll angles, the counter-clockwise vortex is stronger than for decreasing roll angles, which results in the vortex breakdown being closer to the apex for increasing roll angles.

7. Free-to-roll nonslender wings

7.1. Equilibrium positions at nonzero roll angles

Jenkins et al [79] showed that a delta wing configuration with 65-degree sweep angle had multiple stable trim points in roll. In the free-to-roll experiments, the model is released from an initial roll angle, and then is free to roll. In Figure 52, phase plane (roll rate versus roll angle)

trajectories, corresponding to two free-to-roll time histories for the 65 degree wing at α=30°, are shown. For the initial roll angle ϕ_0=-58.3, the trajectory finds the stable equilibrium point at zero roll angle, while for ϕ_0=53.1, the final equilibrium position is around ϕ=21 degrees. The existence of equilibrium positions at nonzero roll angles was also confirmed at other angles of attack for this slender delta wing configuration. The measured static rolling moment is around zero at these nonzero trim angles, and it is believed that asymmetric vortex breakdown is behind this behaviour.

Recent experiments [48, 84] for a free-to-roll nonslender delta wing with 50° sweep angle showed that multiple trim positions are possible. Only nonzero roll angles, or a combination of zero and nonzero roll angles, are possible, depending on the angle of attack. At angles of attack for which vortex breakdown was over the wing, several equilibrium positions at nonzero roll angles were found, depending on the initial roll angle. Figure 53 shows the time history of roll angle for the free-to-roll wing (Λ=50°) for α=15° for the initial roll angle ϕ_0=0° (top) and ϕ_0=45° (bottom). It is seen that, after the wing is released, new equilibrium roll angles are established ($\phi \approx 25°$ and $\phi \approx 35°$), depending on the initial roll angle. Negative equilibrium roll angles (mirror images) are also possible depending on the initial roll angle. It was interesting that zero roll angle was not an equilibrium position for this angle of attack. The existence of multiple roll "attractors" is somewhat similar to the observations for a slender wing (Λ=65°) [79]; however, the main difference is that the zero roll angle is not an attractor for the nonslender wing for pre-stall incidences. The flow physics behind this observation that zero roll angle is not a stable position is not clear, but is believed to be associated with reattachment, rather than vortex breakdown.

Around the stall angle for the nonslender wing with rounded leading-edges [48, 84], simultaneous existence of zero and nonzero trim angles was observed, as shown by two examples in Figure 54 by varying the initial roll angle. For small initial roll angles, the model reaches equilibrium around zero roll angle. For larger initial roll angles, a nonzero trim angle is observed. Just after the stall angle, there is only one trim position at zero roll angle, regardless of the initial roll angle, as shown in Figure 55 for α=35°. It is interesting that, when there is no flow reattachment, the only trim position is zero roll angle. This is consistent with the suspected role of reattachment in the existence of nonzero trim angles for smaller angles of attack. Another observation is that vortex or shear layer interactions such as vortex shedding do not induce self-excited roll oscillations, at least in this case.

7.2. Self-excited roll oscillations

Around the stall angle, self-excited roll oscillations (wing rock) [48, 84] are observed as shown in Figure 56 for a sweep angle of Λ=50°. These oscillations are unusual because not only are they observed for a nonslender wing, but also because the mean roll angle is nonzero. Somewhat similar oscillations were observed for an even lower sweep angle in a different facility [85, 86, 87], as shown in Figure 57 for a sweep angle of Λ=45°. Wing rock has more typically been observed for slender wings with Λ>75° [88] with corresponding mean roll angle of zero. Self-excited roll oscillations of nonslender wings with $\Lambda \leq$ 50° appear to be more complex in their aerodynamic origins than slender wing rock. Similarities to and differences from slender wing rock are discussed in References [89, 90].

In Figure 56, the self-excited roll oscillations are demonstrated for a wing with rounded leading-edges. The self-excited roll oscillations are also observed for a sharp leading-edge, but

are much smaller as shown in Figure 58. Hence, even when the separation point is fixed for the sharp leading-edge, these oscillations occur. As the amplitude of the motion is amplified for a round leading-edge, characteristics of flow separation at the leading-edge are a contributing factor. In both cases, these oscillations are observed around the stall angle, where the reattachment of asymmetric flows is the most important factor. These initial experiments and the related ongoing work on nonslender wings suggest that the main cause of these self-excited oscillations is the separated and vortical flows, which can be very different from those for slender wings, as discussed earlier. In particular, the flow reattachment is suspected to play an important role in the unsteady aerodynamics. In Reference [48], tuft visualizations of surface flow pattern during the self-excited roll motion are presented. For the maximum roll angle, even the secondary separation line outboard of the reattachment line is visible, exhibiting classical signatures of the leading-edge vortex on that side. Therefore, reattachment, hysteresis and large phase lags associated with vortical and separated flows as well as unsteady separation at the leading-edge might be contributing factors to the observed self-induced roll oscillations. It should be noted that knowledge of unsteady flows is limited to slender wings [4, 24] and there is a need to understand unsteady flows over nonslender wings.

It is also interesting that these self-induced oscillations are observed over a small range of incidence. For a sweep angle of Λ=50°, the mean roll angle and the amplitude of roll oscillations are shown as a function of incidence in Figure 59 for a wing with rounded leading-edge and 10% thickness, and a wing with sharp leading-edge and 1.5% thickness. Prior to stall, the mean roll angle is nonzero and there are virtually no roll oscillations. In a critical and small range of incidence, the roll oscillations become large. With further increase in incidence, the mean roll angle becomes zero and the roll oscillations diminish. Comparison with the lift curves shown in

Figure 22 indicates that these self-excited roll oscillations occur around the stall angle. Note that stall occurs earlier for the sharp-edged wing.

8. Conclusions

Flow separation and formation of vortical flow occur at very low angles of attack for nonslender delta wings. Complete roll-up into a concentrated vortex does not take place at low angles of attack, and a broad wake-like flow is observed. As the vortical flow forms close to the wing surface, interactions with boundary layer vorticity may result in a dual vortex structure. As the angle of attack is increased, the primary vortex gets stronger while moving away from the surface. The vortex structure then resembles more that of slender wings, with significant axial flow in the core. Strong Reynolds number effects are observed, in particular for low angles of attack. Also, the effect of low Reynolds number may result in wake-like flow in the core, whereas jet-like flow is typical at higher Reynolds numbers.

Formation of shear layer instabilities in the separated flow from the leading-edge, and their interaction with the secondary flow with vorticity of the opposite sign have close similarities to those for slender wings. Vortex breakdown and transition from a jet-like to a wake-like flow at high angles of attack are much less abrupt for nonslender wings, with the core expanding in a gradual and conical fashion. For very low Reynolds number, even upstream flow may be wake-like and therefore it is difficult to define vortex breakdown based solely on the velocity field.

One of the distinct features of nonslender wings is that the primary attachment line occurs on the surface outboard of the symmetry plane, even when vortex breakdown is near the apex. The primary attachment line moves inboard with increasing angle of attack, and ultimately

reaches the centreline when the wing stalls. Leading-edge shape affects not only the flow separation characteristics, but also the attachment location. Compared to sharp leading-edges, the attachment line is more outboard for any given angle of attack for rounded leading-edges and there is a delay in stall. Compared with slender wings, nonslender delta wings have lower maximum lift coefficient and also lower stall angle. As the vortex lift contribution becomes a smaller proportion of the total lift with decreasing sweep angle, there is no obvious correlation between the onset of vortex breakdown and the change of the lift coefficient.

Flow/structure interactions occur when the frequency of the quasi-periodic oscillations in the vortex breakdown wake is close to the frequencies of the structural modes of the wing. Antisymmetric modes are dominant for full wings, indicating possible coupling of vortex/vortex interactions with the structural motion. At high angles of attack before the stall, the shear layer reattachment becomes an important source of buffeting. With increasing wing flexibility, substantial lift increase in the post-stall region is observed, which appears to be a feature of nonslender wings only. Self-excited antisymmetric vibrations of the wing promote reattachment of the shear layer, which results in the lift enhancement. These self-excited vibrations are not observed for a half-model. With increasing wing flexibility, streamwise flow develops within the reattachment region. Nonslender delta wings undergoing small amplitude roll or pitch oscillations exhibit many similarities with flexible wings. Totally separated flow over a rigid wing in the post-stall region becomes reattached and even the re-formation of the leading-edge vortex is observed with wing oscillations. There is an optimum range of frequencies in the range of St=1 to 2.

Experiments simulating large amplitude roll maneuvers of nonslender wings revealed that the response of the vortical flow strongly depends on the angle of attack, with the most drastic

effects being observed near the stall angle. Free-to-roll nonslender delta wings may have multiple trim positions at nonzero roll angles. Self-excited roll oscillations whose mean roll angle is nonzero are possible in a range of angles of attack, and their amplitude depends on the leading-edge shape. Both unsteady separation and reattachment might be important in the development of the self-induced roll oscillations, because these oscillations are also observed for sharp leading-edges for which the separation lines are fixed.

Acknowledgements

The authors acknowledge the financial support of the Air Force Office of Scientific Research (AFOSR). The first author is particularly indebted to his colleagues, Dr. G. Taylor and Dr. Z. Wang, for valuable discussions.

REFERENCES

1. Gursul, I., "Vortex Flows on UAVs: Issues and Challenges", *The Aeronautical Journal,* vol. 108, No. 1090, December 2004, pp. 597-610.

2. *Workshop on Aerodynamic Issues of Unmanned Air Vehicles*, 4-5 November 2002, University of Bath, UK.

3. Rockwell, D., "Three-Dimensional Flow Structure on Delta Wings at High Angle-of-Attack: Experimental Concepts and Issues", AIAA 93-0050, 31st AIAA Aerospace Sciences Meeting & Exhibit, 11-14 January 1993, Reno, NV.

4. Visbal, M. R., "Computational and Physical Aspects of Vortex Breakdown on Delta Wings", AIAA 95-0585, 33rd AIAA Aerospace Sciences Meeting & Exhibit, 9-12 January 1995, Reno, NV.

5. Delery, J. M., "Aspects of Vortex Breakdown", *Progress in Aerospace Sciences*, Vol. 30, pp. 1-59, 1994.

6. Délery, J. M., "Physics of Vortical Flows", *J. Aircraft*, Vol.29. No. 5, pp. 856-876, 1992.

7. Gursul, I., "Recent Developments in Delta Wing Aerodynamics", *The Aeronautical Journal,* September 2004, pp. 437-452.

8. Earnshaw, P. B. and Lawford, J. A., "Low-Speed Wind-Tunnel Experiments on a Series of Sharp-Edged Delta Wings", ARC Reports and Memoranda No. 3424, March 1964.

9. Wentz, W.H. and Kohlman, D.L., "Vortex Breakdown on Slender Sharp-Edged Wings", *Journal of Aircraft*, vol. 8, no. 3, March 1971, pp. 156-161.

10. Miau, J.J., Kuo, K.T., Liu, W.H., Hsieh, S.J., Chou, J.H., and Lin, C.K., "Flow Developments Above 50-Deg Sweep Delta Wings with Different Leading-Edge Profiles", *Journal of Aircraft,* vol. 32, no. 4, July-August 1995, pp. 787-794.

11. Ol, M. V. and Gharib, M., "Leading-Edge Vortex Structure of Nonslender Delta Wings at Low Reynolds Number", *AIAA Journal*, Vol. 41, No. 1, January 2003, pp. 16-26.

12. Ol, M. V., "An Experimental Investigation of Leading Edge Vortices and Passage to Stall of Nonslender Delta Wings," Symposium on Advanced Flow Management, RTO AVT-072, May 2001, Paper 2.

13. Ol, M. V., and Gharib, M., "The Passage Toward Stall of Nonslender Delta Wings at Low Reynolds Number," AIAA Paper 2001-2843, 31st AIAA Fluid Dynamics Conference and Exhibit, 11-14 June 2001, Anaheim, CA.

14. Gursul, I., Taylor, G., and Wooding, C., "Vortex Flows over Fixed-Wing Micro Air Vehicles", AIAA 2002-0698, 40th AIAA Aerospace Sciences Meeting & Exhibit, 14-17 January 2002, Reno, NV.

15. Taylor, G.S., Schnorbus, T., and Gursul, I., "An Investigation of Vortex Flows over Low Sweep Delta Wings", AIAA-2003-4021, AIAA Fluid Dynamics Conference, 23-26 June, Orlando, FL.

16. Gordnier, R. E. and Visbal, M. R., "Higher-Order Compact Difference Scheme Applied to the Simulation of a Low Sweep Delta Wing Flow", AIAA 2003-0620, 41st AIAA Aerospace Sciences Meeting and Exhibit, 6-9 January 2003, Reno, NV.

17. Erickson, G. E., "Water Tunnel Studies of Leading Edge Vortices", *Journal of Aircraft*, Vol. 19, No. 6, pp. 442-448, 1982.

18. Menke, M. and Gursul, I., "Unsteady Nature of Leading Edge Vortices", *Physics of Fluids*, Vol. 9, No. 10, 1997, pp. 2960-2966.

19. Gursul, I., "Unsteady Flow Phenomena over Delta Wings at High Angle-of-Attack", *AIAA Journal*, Vol. 32, No. 2, 1994, pp. 225-231.

20. Gursul, I. and Xie, W., "Buffeting Flows over Delta Wings", *AIAA Journal*, Vol. 37, No. 1, 1999, pp. 58-65.

21. Gordnier, R.E. and Visbal, M.R. “Unsteady vortex structure over a delta wing”, *Journal of Aircraft,* vol. 31, no. 1, 1994, pp. 243-248.

22. Menke, M., Yang, H. and Gursul, I., "Experiments on the Unsteady Nature of Vortex Breakdown over Delta Wings", *Experiments in Fluids*, vol. 27, 1999, pp. 262-272.

23. Redinoitis, O. K., Stapountzis, H., and Telionis, D. P., “Periodic Vortex Shedding over Delta Wings”, *AIAA Journal*, Vol. 31, No. 9, 1993, pp. 1555-1561.

24. Gursul, I., “Review of Unsteady Vortex Flows over Slender Delta Wings”, *Journal of Aircraft,* vol. 42, no. 2, March-April 2005, pp. 299-319.

25. Traub, L.W., “Extending Slender Wing Theory to Not So Slender Wings”, *Journal of Aircraft,* vol. 40, no. 2, 2003, pp. 399-402.

26. Polhamus, E.C., “Predictions of Vortex-Lift Characteristics by a Leading-Edge Suction Analogy”, *Journal of Aircraft,* vol. 8, no. 4, April, 1971, pp. 193-199.

27. Lee, M. and Ho, C.,‘Lift force of delta wings’, *App. Mech. Rev.*, Vol. 43, No. 9, pp. 209-221, 1990.

28. Bartlett, G.E. and Vidal, R.J., "Experimental Investigation of Influence of Edge Shape on the Aerodynamic Characteristics of Low Aspect Ratio Wings at Low Speeds", *Journal of The Aeronautical Sciences,* vol. 22, no. 8, August 1955, pp. 517-533.

29. Huang, X.Z., Mebarki, Y., Benmeddour, A., and Brown ,T., "Experimental and Numarical Studies of Geometry Effects on UCAV's Aerodynamics", AIAA-2004-0403.

30. Taylor, G. and Gursul, I., "Buffeting Flows over a Low Sweep Delta Wing", *AIAA Journal,* vol. 42, no. 9, September 2004, pp. 1737-1745.

31. Yaniktepe, B. and Rockwell, D., "Flow Structure on a Delta Wing of Low Sweep Angle", *AIAA Journal,* vol. 42, no. 3, March 2004, pp. 513-523.

32. Gordnier, R. E. and Visbal, M. R., "Instabilities in the Shear Layer of Delta Wings", AIAA-95-2281, 26th Fluid dynamics Conference, June, 1995, San Diego, CA.

33. Visbal, M. R. and Gordnier, R. E., "Origin of the Computed Unsteadiness in the Shear Layer of Delta Wings", *Journal of Aircraft*, vol. 32, no. 5, 1995, pp. 1146-1148.

34. Visbal, M. R. and Gordnier, R. E., "On the structure of the shear Layer emanating from a Swept Leading Edge at Angle of Attack", AIAA-2003-4016, 33rd Fluid Dynamics Conference and Exhibit, June, 2003, Orlando, FL.

35. Gad-el-Hak, M. and Blackwelder, R. F., "The Discrete Vortices from a Delta Wing", Vol. 23, No. 6, June, 1985, pp. 961-962.

36. Yavuz, M. M., Elkhoury, M., and Rockwell, D., "Near-Surface Topology and Flow Structure on a Delta Wing", *AIAA Journal*, Vol. 42, No. 2, pp. 332-340, 2004.

37. Lambourne, N. C. and Bryer, D. W., "The Bursting of Leading-edge Vortices – Some Observations and Discussion of the Phenomenon", ARC Reports & Memoranda No. 3282, April, 1961.

38. Visbal, M. R., "Computed Unsteady Structure of Spiral Vortex Breakdown on Delta Wings", AIAA-1996-2074, 27th AIAA Fluid Dynamics Conference, June, 1996, New Orleans, LA.

39. Lowson, M. V., "Some Experiments with Vortex Breakdown", Journal of the Royal Aeronautical Society, Vol. 68, May, 1964.

40. Taylor, G. S. and Gursul, I., "Unsteady Vortex Flows and Buffeting of a Low Sweep Delta Wing", AIAA-2004-1066, 42nd AIAA Aerospace Sciences Meeting & Exhibit, 5-9 January 2004, Reno, NV.

41. Brown, G. and Lopez, J., "Axisymmetric Vortex Breakdown, part 2. Physical mechanisms", Journal of Fluid Mechanics, Vol. 221, 1990, pp. 553-576.

42. Honkan, A. and Andreopoulos, J., "Instantaneous Three-Dimensional Vorticity Measurements in Vortical Flow over a Delta Wing", *AIAA Journal*, Vol. 35, No. 10, October 1997, pp. 1612-1620.

43. Lynn, R.J., Gib, J. and Shires, A., "Buffet Tests on a 40 Degree Diamond Wing Planform – Model M2391", DERA Report, DERA/MSS4/TR980309/1.0, August 1998.

44. Woods, M.I., "An Investigation of Buffet over Low-Observable Planforms", PhD Thesis, University of Bath, 1999.

45. Woods, M.I. and Wood, N.J., "Aerodynamic Characteristics of Lambda Wings", *The Aeronautical Journal,* April 2000, pp. 165-174.

46. Moore, D.W. and Pullin, D.I., "Inviscid Separated Flow over a Non-slender Delta Wing", *Journal of Fluid Mechanics*, vol. 305, 1995, pp. 307-345.

47. Elkhoury, M. and Rockwell, D., "Visualized Vortices on Unmanned Combat Air Vehicle Planform: Effect of Reynolds Number", *Journal of Aircraft,* vol. 41, no. 5, 2004, pp. 1244-1247.

48. McClain, A., "Aerodynamics of Nonslender Delta Wings", MPhil Thesis, University of Bath, Department of Mechanical Engineering, March 2004.

49. Kawazoe, H., Nakamura, Y., Ono, T., and Ushimaru, Y., "Static and Total Pressure Distributions around a Thick Delta Wing with Rounded Leading-Edge", AIAA-94-2321, 25th AIAA Plasmadynamics and Lasers Confernce, June 20-23, 1994, Colorado Springs, CO.

50. Kegelman, J.T. and Roos, F.W., "Effects of Leading-Edge Shape and Vortex Burst on the Flowfield of a 70° Sweep Delta Wing", AIAA Paper No. 89-0086, AIAA 27th Aerospace Sciences Meeting, Reno, NV, January 1989.

51. Gray, J., Gursul, I. and Butler, R., 2003, "Aeroelastic Response of a Flexible Delta Wing Due to Unsteady Vortex Flows", AIAA-2003-1106, 41st Aerospace Sciences Meeting and Exhibit, 6-9 January, Reno, NV.

52. Gordnier, R.E. and Visbal, M.R., "Computation of the Aeroelastic Response of a Flexible Delta Wing at High Angles of Attack", AIAA-2003-1728.

53. Doggett, R. V. and Soistmann, D. L., "Some Low-Speed Flutter Characteristics of Simple Low-Aspect-Ratio Delta Wing Models", NASA TM 101547, January, 1989.

54. Tang, D., Henry, J. K., and Dowell, E. H., "Limit Cycle Oscillations of Delta Wing Models in Low Subsonic Flow", *AIAA Journal*, Vol. 37, No. 11, November, 1999.

55. Tang, D. and Dowell, E. H., "Effects of Angle of Attack on Nonlinear Flutter of a Delta Wing", *AIAA Journal*, vol. 39, No. 1, January , 2001.

56. Attar, P. J., Dowell, E. H. and Tang, D., "A theoretical and experimental investigation of the effects of a steady angle of attack on the nonlinear flutter of a delta wing plate model", *Journal of Fluids and Structures*, vol. 17, 2003, pp. 243-259.

57. Attar, P. J., Dowell, E. H. and Tang, D., "Modeling Aerodynamic Nonlinearities for two Aeroelastic Configurations: Delta Wing and Flapping Flag", 44th AIAA/ASME/ASCE/AHS/ASC Structures, Structural Dynamics and Materials Conference, April, 2003, Norfolk, VA.

58. Attar, P. J., Dowell, E. H. and White, J. R., "Modeling the LCO of a Delta Wing Using a High Fidelity Structural Model", AIAA-2004-1692, 45th AIAA/ASME/ASCE/AHS/ASC Structures, Structural Dynamics and Materials Conference, April, 2004, Palm Springs CA.

59. Gordnier, R.E. and Melville, R., "Numerical Simulation of Limit-Cycle Oscillations of a Cropped Delta Wing Using the Full Navier-Stokes Equations", *International Journal of Computational Fluid Dynamics,* vol. 14, no. 3, 2001, pp. 211-222.

60. Attar, P. J. and Gordnier, R. E., "Aeroelastic Prediction of the Limit Cycle Oscillations of a Cropped Delta Wing", AIAA-2005-1915, 46th AIAA/ASME/ASCE/AHS/ASC Structures, Structural Dynamics and Materials Conference, April, 2005, Austin, TX.

61. Schairer, E. T. and Hand, L. A., "Measurements of Unsteady Aeroelastic Model Deformation by Stereo Photogrammetry", AIAA-1997-2217, 15th Applied Aerodynamics Conference, June, 1997, Atlanta, GA.

62. Taylor, G. S. and Gursul I, 'Lift Enhancement over a Flexible Low Sweep Delta Wing, AIAA-2004-2618 2nd AIAA Flow Control Conference, 27 June – 1 July 2004, Portland, OR.

63. Gursul, I., Vardaki, E. and Taylor, G., "Flow Control with Wing Flexibility", 1st Europen Forum on Flow Control, October 11-14, 2004, Poitiers, France.

64. Taylor, G.S., Kroker, A. and Gursul, I., "Passive Flow Control over Flexible Nonslender Delta Wings", AIAA-2005-0865, 43rd Aerospace Sciences Meeting and Exhibit, 10-13 January 2005, Reno, NV.

65. Lian, Y., Shyy, W., Viieru, D., and Zhang, B., "Membrane Wing Aerodynamics for Micro Air Vehicles", *Progress in Aerospace Sciences,* vol. 39, no. 6-7, 2003, pp. 425-465.

66. Pelletier, A. and Mueller, T.J., "Low Reynolds Number Aerodynamics of Low-Aspect-Ratio, Thin/Flat/Cambered-Plate Wings", *Journal of Aircraft,* vol. 37, no. 5, 2000, pp. 825-832.

67. Wooding, C.L. and Gursul, I., 2003, "Unsteady Aerodynamics of Low Aspect Ratio Wings at Low Reynolds Numbers", Royal Aeronautical Society Aerospace Aerodynamics Research Conference, 10-12 June, London.

68. Torres, G.E., and Mueller, T.J., "Aerodynamic Characteristics of Low Aspect Ratio Wings at Low Reynolds Numbers", *Proceedings of the Conference: Fixed, Flapping and Rotary Wing Vehicles at Very Low Reynolds Numbers*, Univ. of Notre Dame, Notre Dame, IN, 5-7 June 2000, pp. 228-305.

69. Roos, F.W. and Kegelman, J.T., "Control of Coherent Structures in Reattaching Laminar and Turbulent Shear Layers", *AIAA Journal,* vol. 24, no. 12, December 1986, pp. 1956-1963.

70. Cipolla, K. M. and Rockwell, D., "Flow Structure on Stalled Delta Wing Subjected to Small Amplitude Pitching Oscillations", *AIAA Journal*, Vol. 33, No. 7, pp. 1256-1262, July 1995.

71. Gad-el-Hak, M. and Blackwelder, R. F., "Control of the Discrete Vortices from a Delta Wing", *AIAA Journal*, Vol. 25, No. 8, pp. 1042-1049, 1987.

72. Margalit, S., Greenblatt, D., Seifert, A., and Wygnanski, I., "Active Flow Control of a Delta Wing at High Incidence Using Segmented Piezoelectric Actuators", AIAA 2002-3270, 1st AIAA Flow Control Conference, 24-26 June 2002, St. Louis, MO.

73. Siegel, S., McLaughlin, T. E., and Albertson, J. A., "Partial Leading Edge Blowing of a Delta Wing at High Angles of Attack", AIAA 2002-3268, 1st AIAA Flow Control Conference, 24-26 June 2002, St. Louis, MO.

74. Siegel, S., McLaughlin, T. E., and Morrow, J. A., "PIV Measurements on a Delta Wing with Periodic Blowing and Suction", AIAA 2001-2436, 19th AIAA Applied Aerodynamics Conference, June 2001, Anaheim, CA.

75. Vardaki, E., Gursul, I. And Taylor, G., "Physical Mechanisms of Lift Enhancement for Flexible Delta Wings", AIAA-2005-0867, 43rd Aerospace Sciences Meeting and Exhibit, 10-13 January 2005, Reno, NV.

76. Cummings, R. M., Morton, S. A., Siegel, S. G., and Bosscher, S., "Numerical Prediction and Wind Tunnel Experiment for a Pitching Unmanned Combat Air Vehicle", AIAA-2003-0417, 41st Aerospace Sciences Meeting, 6-9 January 2003, Reno, NV.

77. Ashley, H., Katz, J., Jarrah, M.A., and Vaneck, T., "Survey of Research on Unsteady Aerodynamic Loading of Delta Wings", *Journal of Fluids and Structures,* vol. 5, 1991, pp. 363-390.

78. Soltani, M.R., Bragg, M.B. and Brandon, J.M., "Measurements on an Oscillating 70-Deg Delta Wing in Subsonic Flow", *Journal of Aircraft,* vol. 27, no. 3, March 1990, pp. 211-217.

79. Jenkins, J. E., Myatt, J. H., and Hanff, E. S., "Body-Axis Rolling Motion Critical States of a 65-Degree Delta Wing," *Journal of Aircraft*, Vol. 33, No. 2, 1996, pp. 268-278.

80. Hanff, E. S., and Huang, X. Z., "Roll-Induced Cross-Loads on a Delta Wing at High Incidence," AIAA Paper 91-3223, 9th AIAA Applied Aerodynamics Conference, 23-25 September 1991, Baltimore, MD.

81. Huang, X. Z., and Hanff, E. S., "Prediction of Normal Force on a Delta Wing Rolling at High Incidence," AIAA Paper 93-3686, AIAA Atmospheric Flight Mechanics Conference, 9-11 August 1993, Monterey, CA.

82. Vardaki, E. and Gursul, I., "Vortex Flows on a Rolling Nonslender Delta Wing", AIAA-2004-4729, 22nd AIAA Applied Aerodynamics Conference, 16-19 August 2004, Providence, Rhode Island.

83. Gordnier, R.E., "Computation of Vortex Breakdown on a Rolling Delta Wing", *Journal of Aircraft,* vol. 32, no. 3, 1995, pp. 686-688.

84. Hüschler, S., "Wing Rock of Nonslender Delta Wings", Research Project Report, University of Bath, June 2003.

85. Ueno, M., Matsuno, T., and Nakamura, Y., "Unsteady Aerodynamics of Rolling Thick Delta Wing with High Aspect Ratio", AIAA-98-2520, 16th Applied Aerodynamics Conference, June 15-18, 1998, Albuquerque, NM.

86. Matsuno, T., Yokouchi, S., and Nakamura, Y., "The Effect of Leading-Edge Profile on Self-Induced Oscillations of 45-Degree Delta Wings", AIAA-2000-4004.

87. Matsuno, T. and Nakamura, T., "Self-induced Roll Oscillation of 45-Degree Delta Wings", AIAA-2000-0655, 38th AIAA Aerospace Sciences Meeting and Exhibit, 10-13 January 2000, Reno, NV.

88. Arena, A.S. and Nelson, R.C., "Experimental Investigations on Limit Cycle Wing Rock of Slender Wings", *Journal of Aircraft,* vol. 31, no. 5, Sept-Oct. 1994, pp. 1148-1155.

89. Ericksson, L.E., "Wing Rock of Nonslender Delta Wings", *Journal of Aircraft,* vol. 38, no. 1, January-February 2001, pp. 36-41.

90. Ericksson, L.E. and Beyers, M.E., "An Analysis of Self-Induced Roll Oscillations of a 45-Degree Delta Wing", AIAA-2003-0737.

FIGURE CAPTIONS

Figure 1: Current and future Unmanned Combat Air Vehicles and fixed-wing Micro Air Vehicles.

Figure 2: Variation of lift coefficient with angle of attack [8].

Figure 3: Variation of maximum normal force coefficient as a function of sweep angle from various sources.

Figure 4: Surface oil flow visualization of the flow over a 50° sweep delta wing at α=2.5°

Figure 5: Mean axial velocity profile through the vortex core at x/c=0.3 for a Λ=50° sweep delta wing.

Figure 6: Mean vortex structure over a Λ=50° sweep delta wing at α=5° angle of attack showing development of a dual vortex structure.

Figure 7: Dual vortex structure in a crossflow plane a) computation by Gordnier and Visbal [16], Λ=50°, α=5° b) PIV measurement by Taylor et al [15] Λ=50°, α=7.5° c) PIV measurement by Yaniktepe and Rockwell [31] Λ=38.7°, α=7°

Figure 8: Mean vortex structure over a Λ=50° sweep delta wing at α=15° angle of attack showing vortex structure b) crossplane upstream of breakdown c) crossplane downstream of breakdown

Figure 9: Λ=50° sweep wing at α=15° Upper – Surface streamline pattern and pressure coefficient [16], Lower – Surface oilflow pattern [30]

Figure 10: Instantaneous vortex structure over a Λ=50° wing at α=15°

Figure 11: Instantaneous vortex structure on a crossflow plane for a Λ=50° sweep wing at α=15° a,b) upstream of breakdown and c,d) downstream of breakdown.

Figure 12: Shear Layer substructures visible in the PIV measurements of Yavuz et al [36] for a Λ=38.7° sweep wing on a plane parallel and immediately adjacent to the surface of the wing.

Figure 13: Comparison of dye flow visualization of Yaniktepe and Rockwell [31] and the computational streakline of Gordnier and Visbal [16].

Figure 14: Mean axial velocity contours on a plane through the vortex core: a) α=15°, b) α=10°, c) α=5°

Figure 15: Comparison of the velocity magnitude on a plane through the vortex core for a Λ=50° sweep wing at α=15°. Upper – PIV measurements of Taylor and Gursul [30], Lower – Computations of Gordnier and Visbal [16]

Figure 16: Instantaneous vortex structure on a plane through the vortex core a) axial vorticity, b) axial velocity, c) fluctuating kinetic energy.

Figure 17: PIV measurements [30] of the rms velocity and streamline pattern on a plane parallel and adjacent to the surface of the wing.

Figure 18: Variation of spanwise location of reattachment line with incidence for measurements in both a wind tunnel and water channel.

Figure 19: Influence of Reynolds number on dual vortex structure a) Re=10,000, b) Re=20,000, c) Re=50,000

Figure 20: Variation of spanwise location of vortex core with Reynolds number from various experiments and computations [10, 11, 16, 30].

Figure 21: Location of reattachment line as a function of angle of attack for various leading-edge shapes, t/c=4%.

Figure 22: Variation of lift coefficient with angle of attack for various leading-edge shapes and thickness.

Figure 1: Current and future Unmanned Combat Air Vehicles and fixed-wing Micro Air Vehicles.

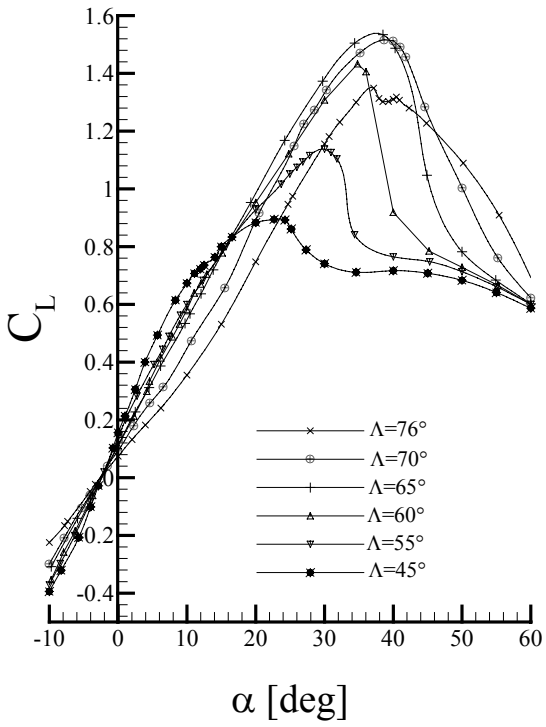

Figure 2: Variation of lift coefficient with angle of attack, adapted from [8].

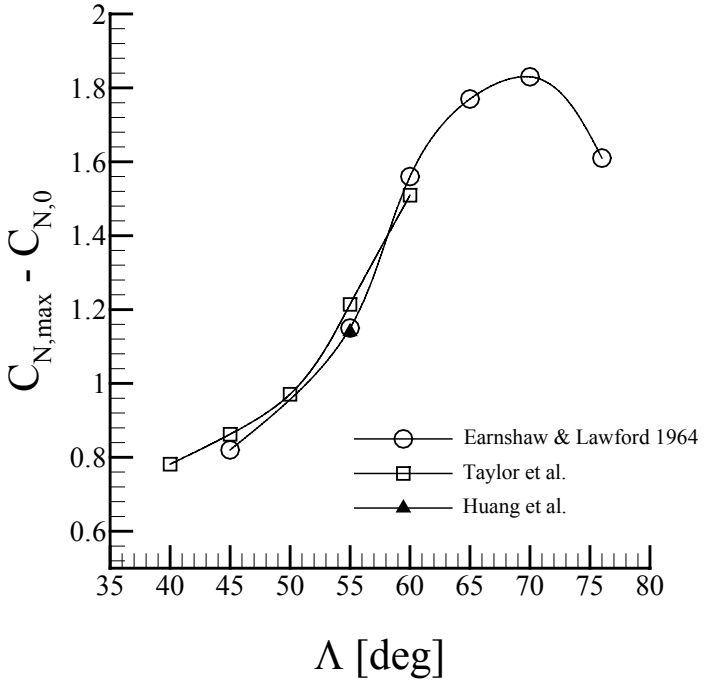

Figure 3: Variation of maximum normal force coefficient as a function of sweep angle from various sources.

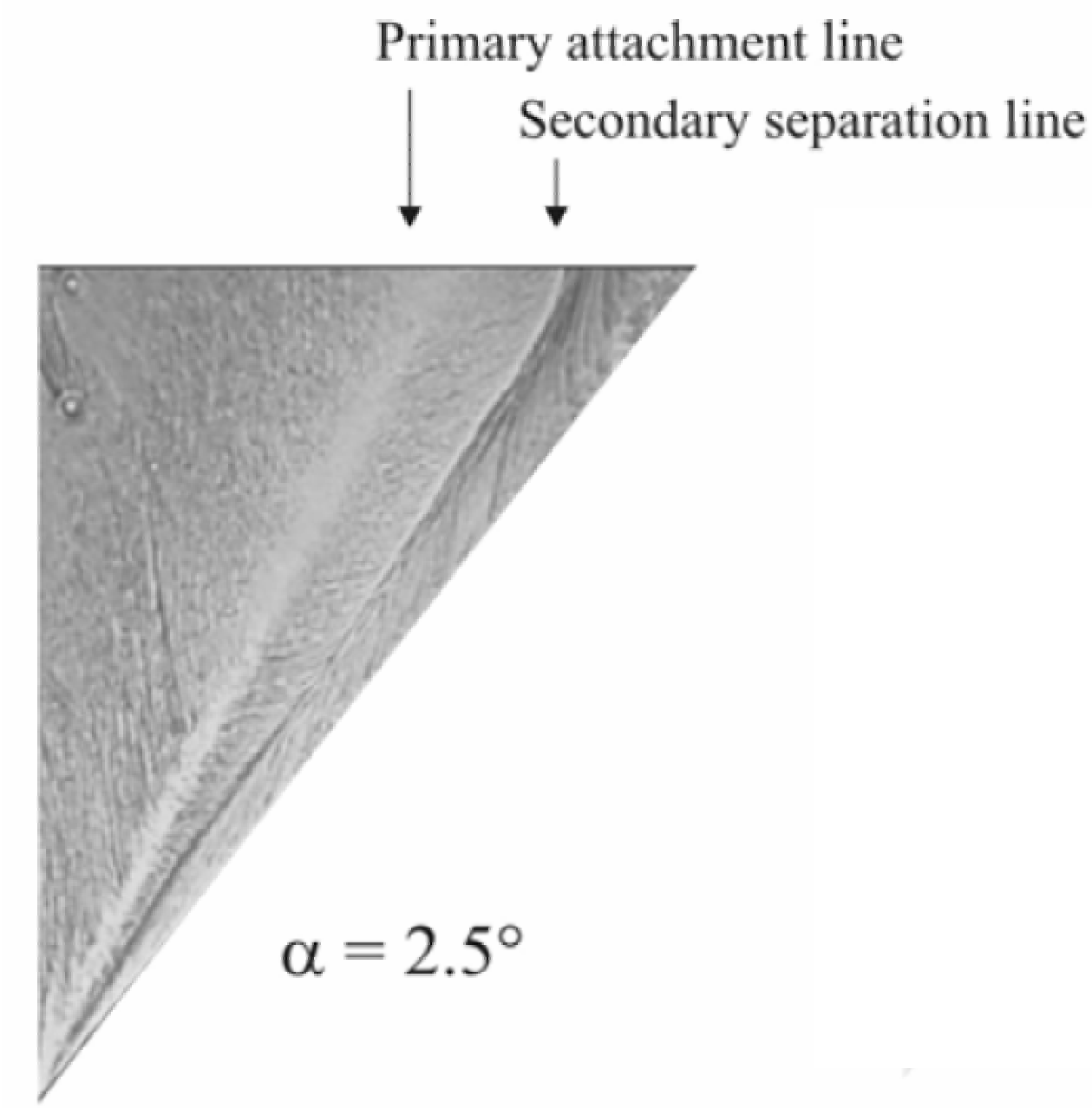

Figure 4: Surface oil flow visualization of the flow over a 50° sweep delta wing at α=2.5°

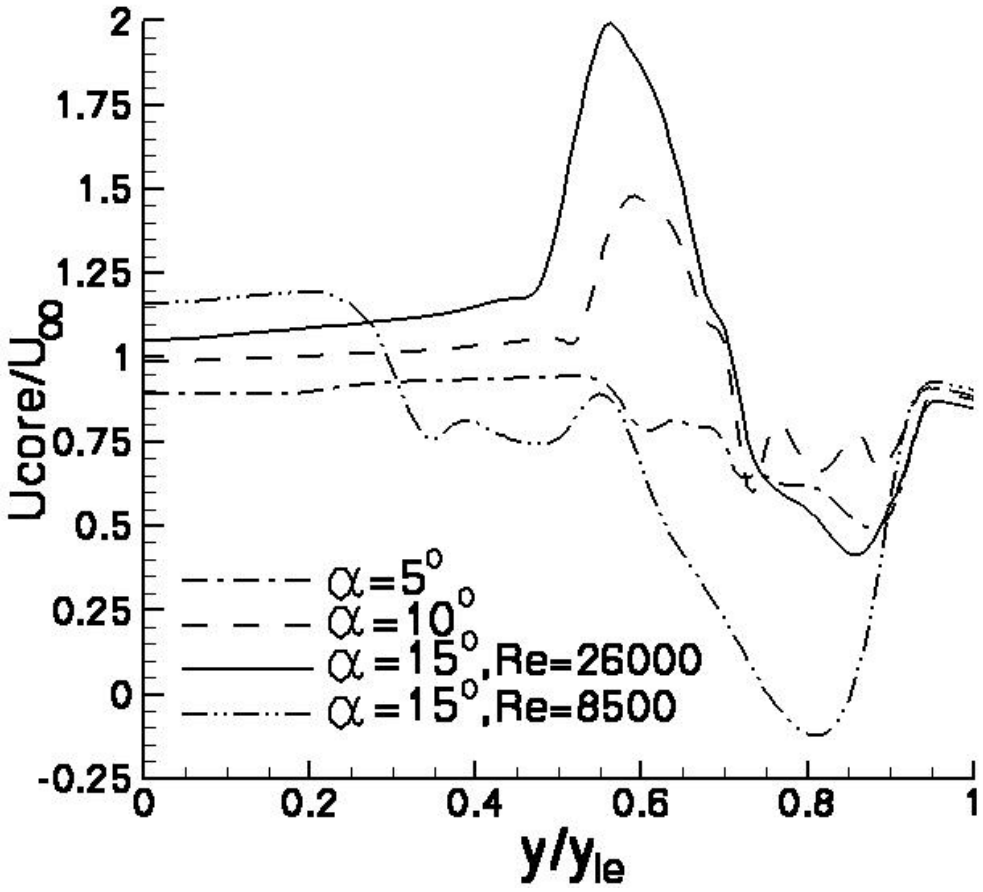

Figure 5: Mean axial velocity profile through the vortex core at x/c=0.3 for a Λ=50° sweep delta wing.

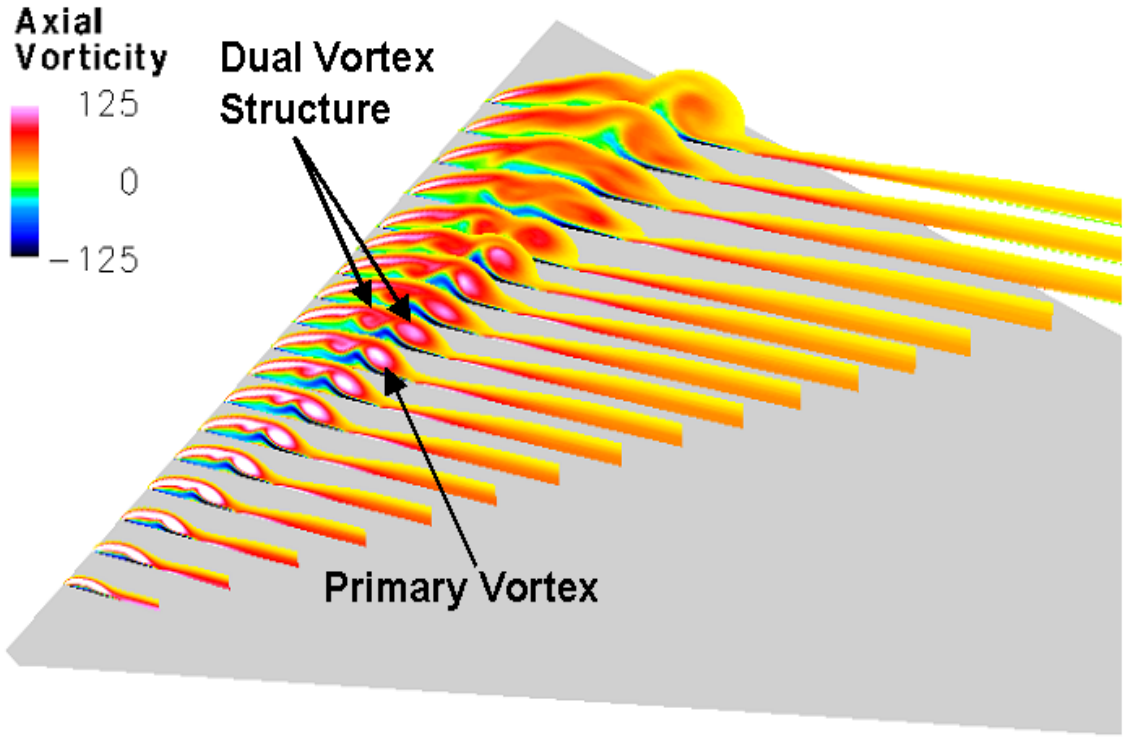

Figure 6: Mean vortex structure over a Λ=50° sweep delta wing at α=5° angle of attack showing development of a dual vortex structure.

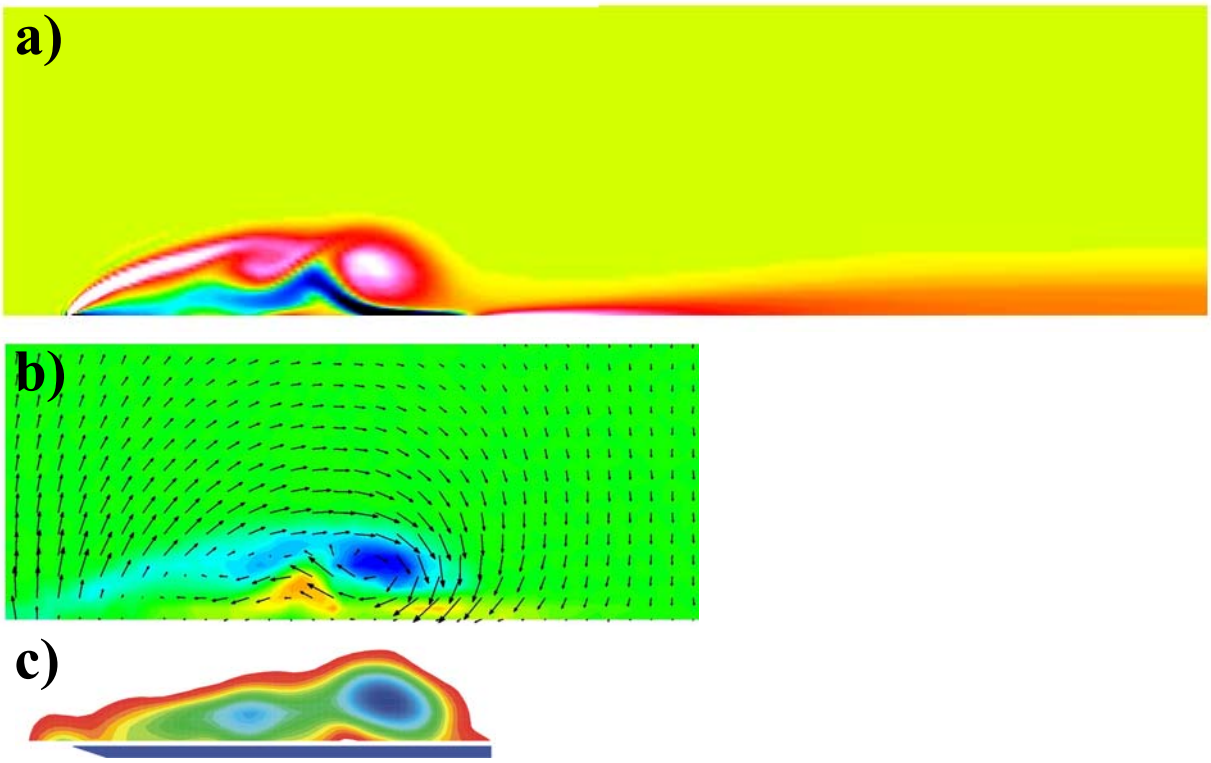

Figure 7: Dual vortex structure in a crossflow plane a) computation by Gordnier and Visbal [16], Λ=50°, α=5° b) PIV measurement by Taylor et al [15] Λ=50°, α=7.5° c) PIV measurement by Yaniktepe and Rockwell [31] Λ=38.7°, α=7°

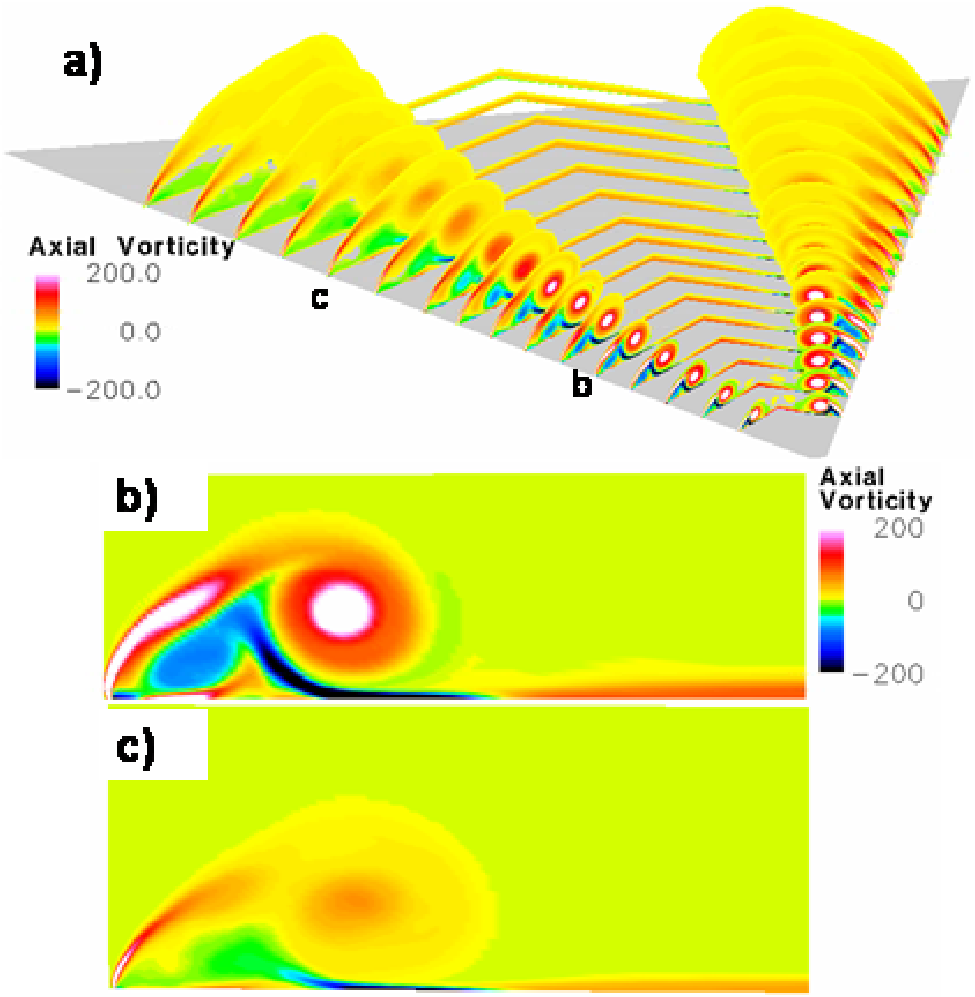

Figure 8: Mean vortex structure over a Λ=50° sweep delta wing at α=15° angle of attack showing vortex structure b) crossplane upstream of breakdown c) crossplane downstream of breakdown

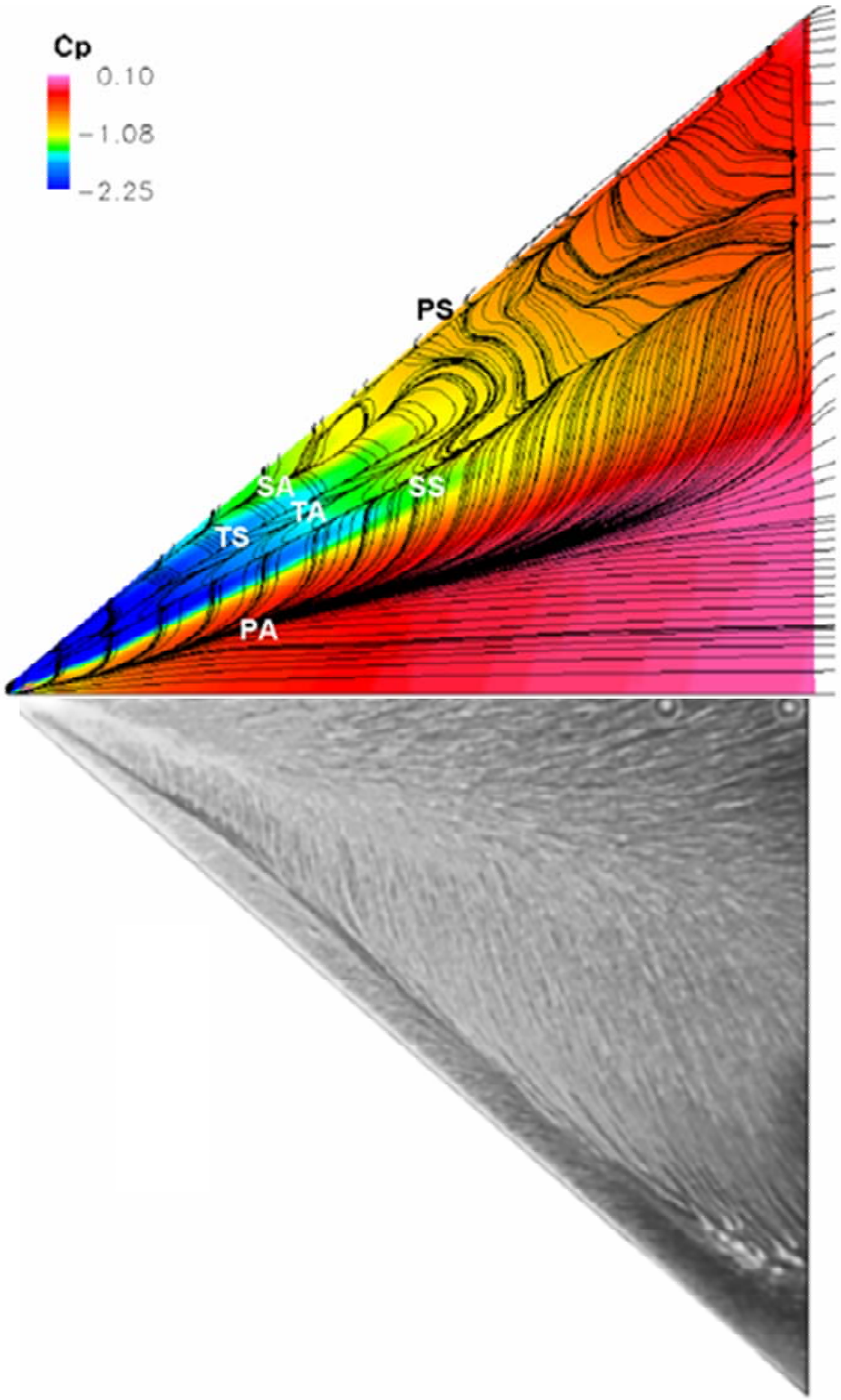

Figure 9: Λ=50° sweep wing at α=15° Upper – Surface streamline pattern and pressure coefficient [16], Lower – Surface oilflow pattern [30]

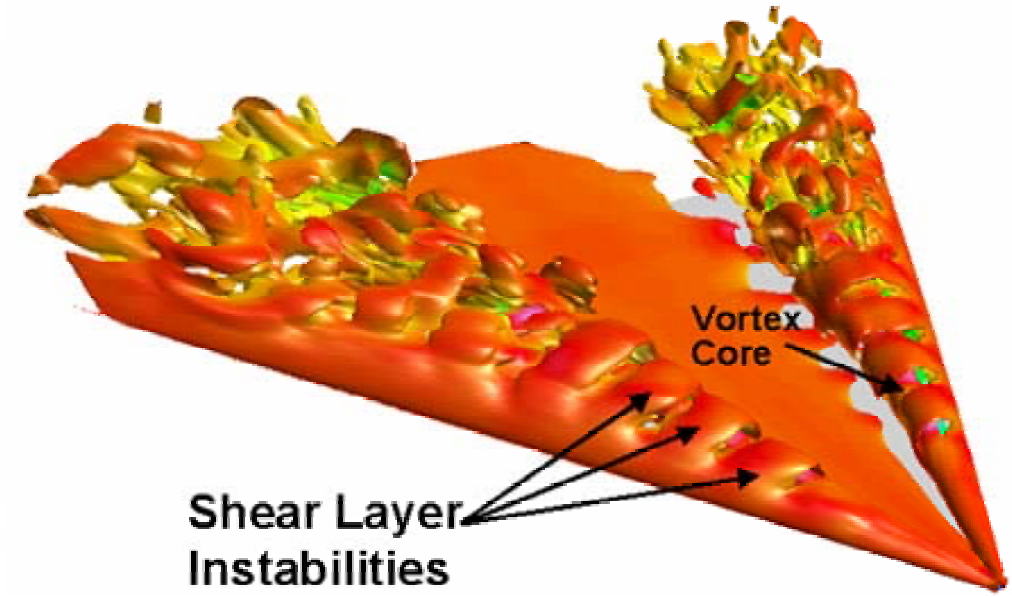

Figure 10: Instantaneous vortex structure over a Λ=50° wing at α=15°

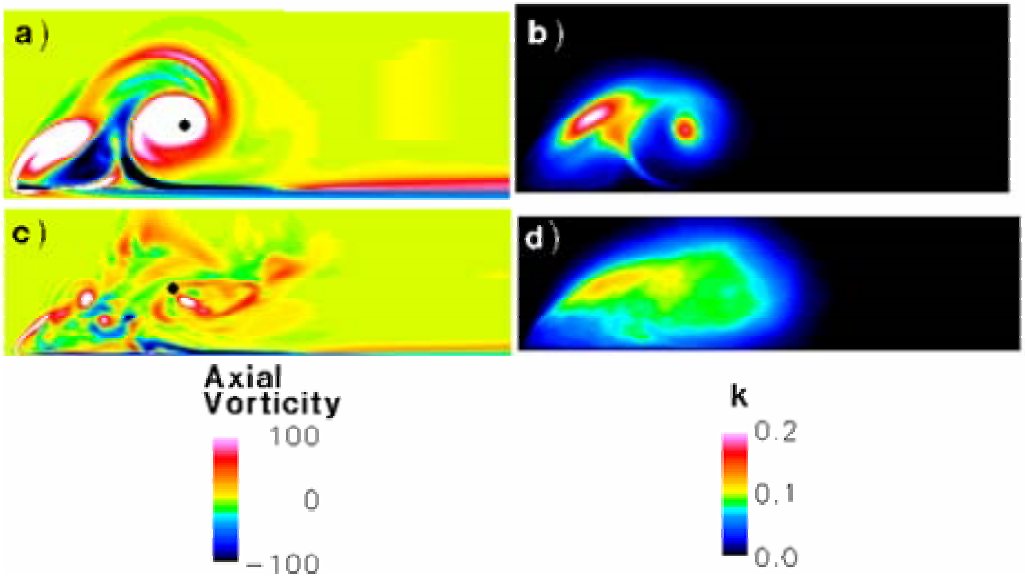

Figure 11: Instantaneous vortex structure on a crossflow plane for a Λ=50° sweep wing at α=15° a,b) upstream of breakdown and c,d) downstream of breakdown.

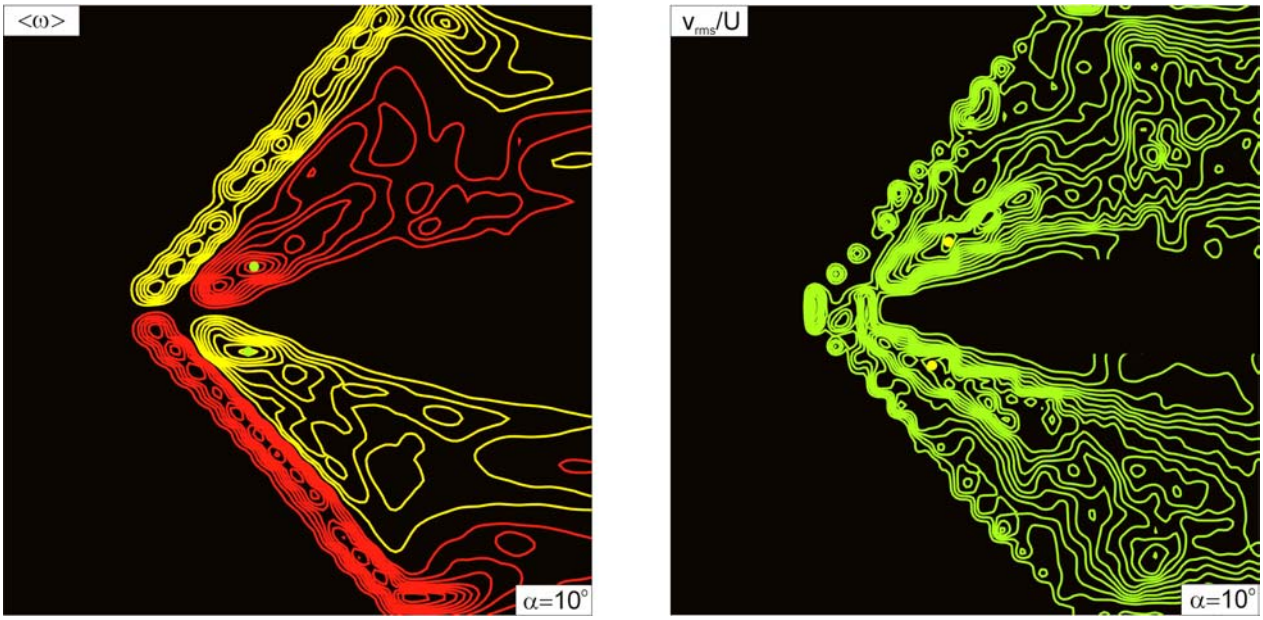

Figure 12: Shear Layer substructures visible in the PIV measurements of Yavuz et al [36] for a Λ=38.7° sweep wing on a plane parallel and immediately adjacent to the surface of the wing.

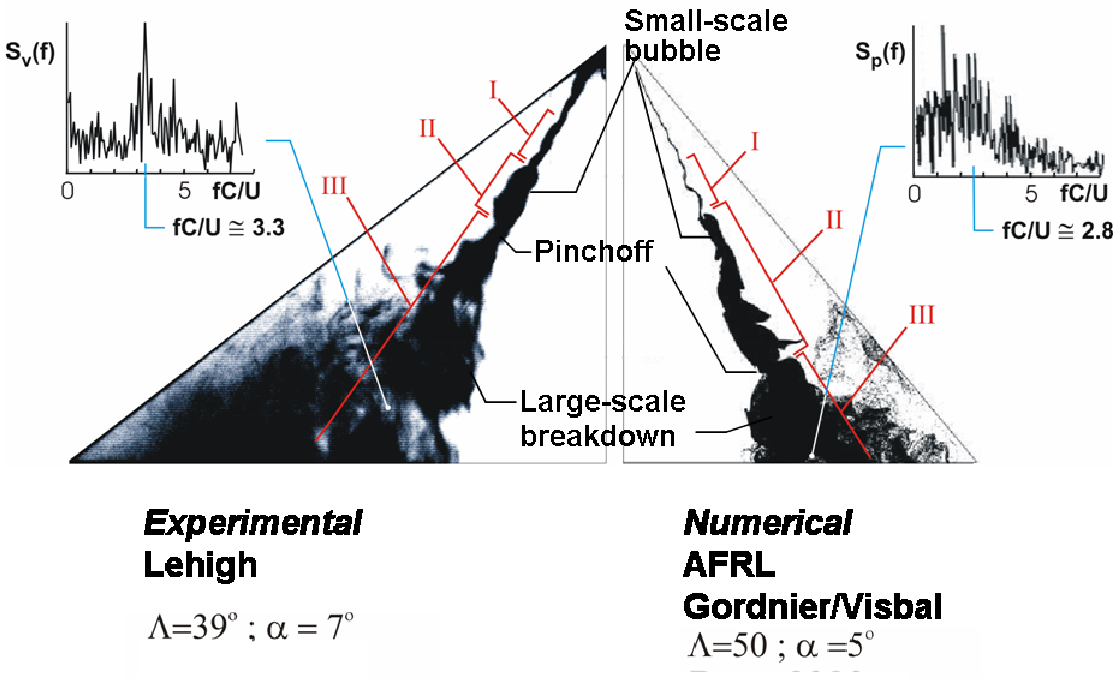

Figure 13: Comparison of dye flow visualization of Yaniktepe and Rockwell [31] and the computational streakline of Gordnier and Visbal [16].

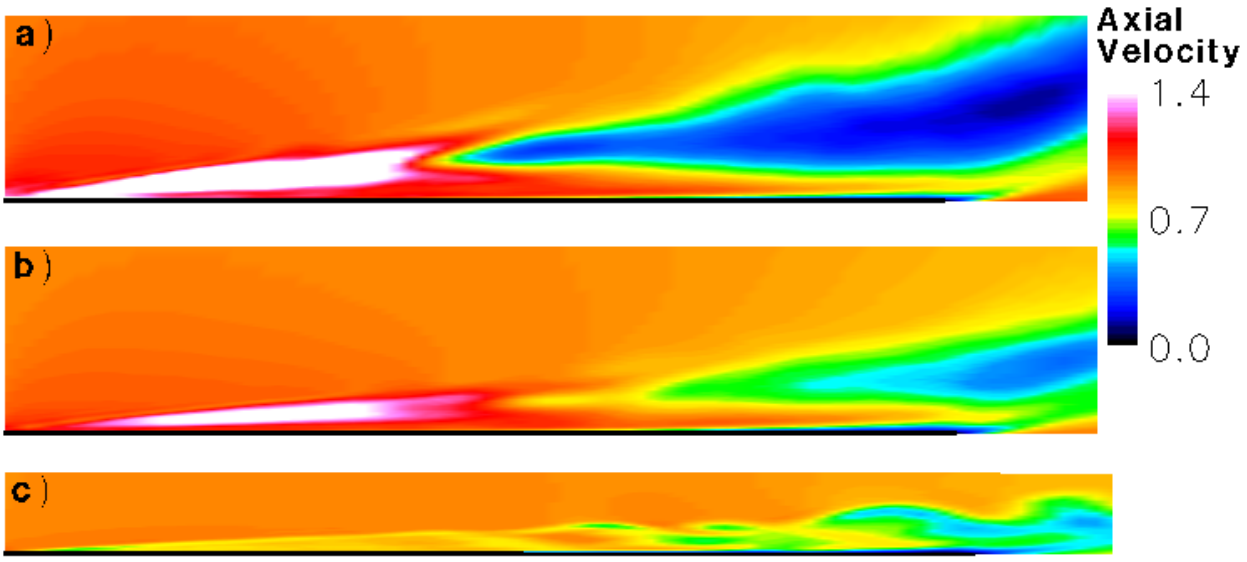

Figure 14: Mean axial velocity contours on a plane through the vortex core: a) α=15°, b) α=10°, c) α=5°

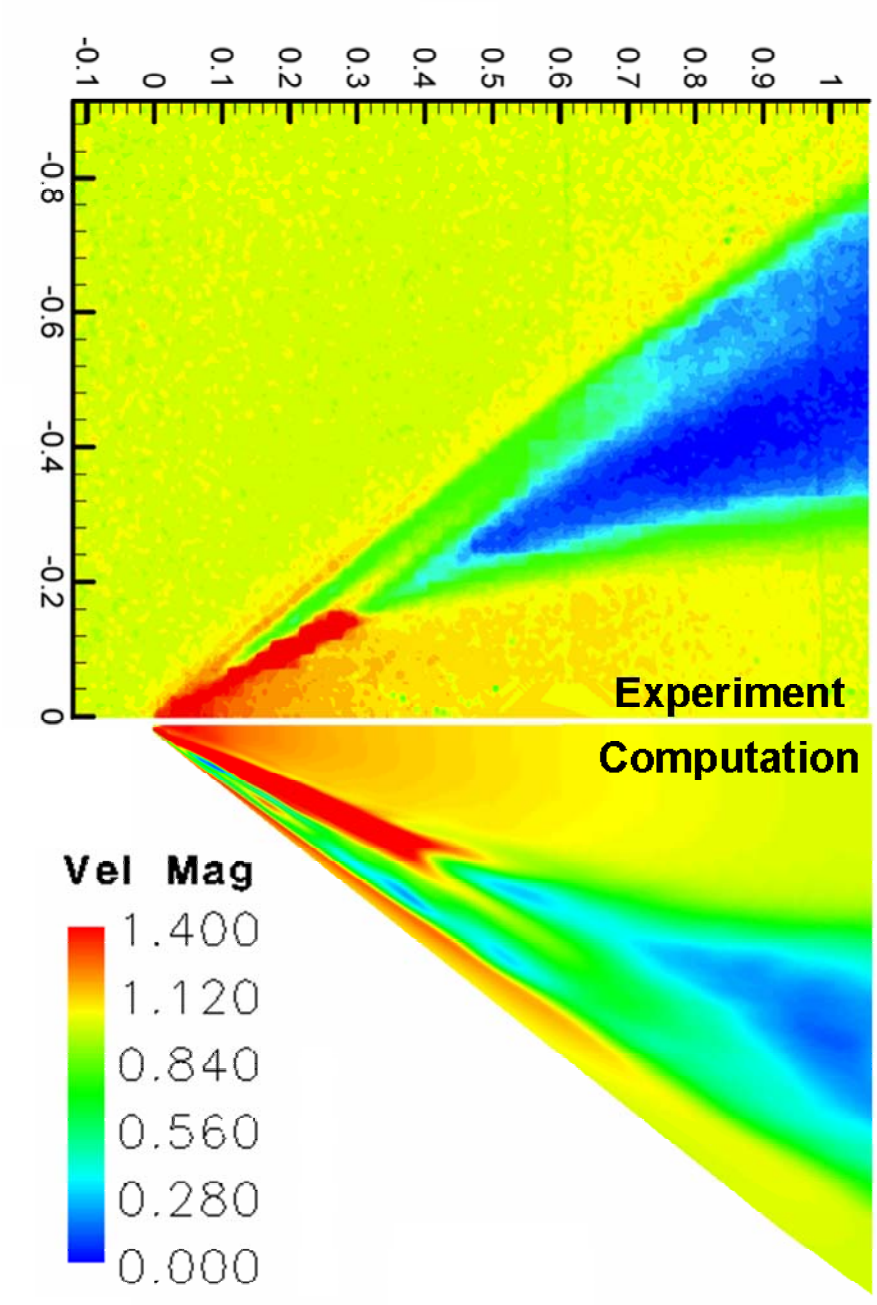

Figure 15: Comparison of the velocity magnitude on a plane through the vortex core for a Λ=50° sweep wing at α=15°. Upper – PIV measurements of Taylor and Gursul [30], Lower – Computations of Gordnier and Visbal [16]

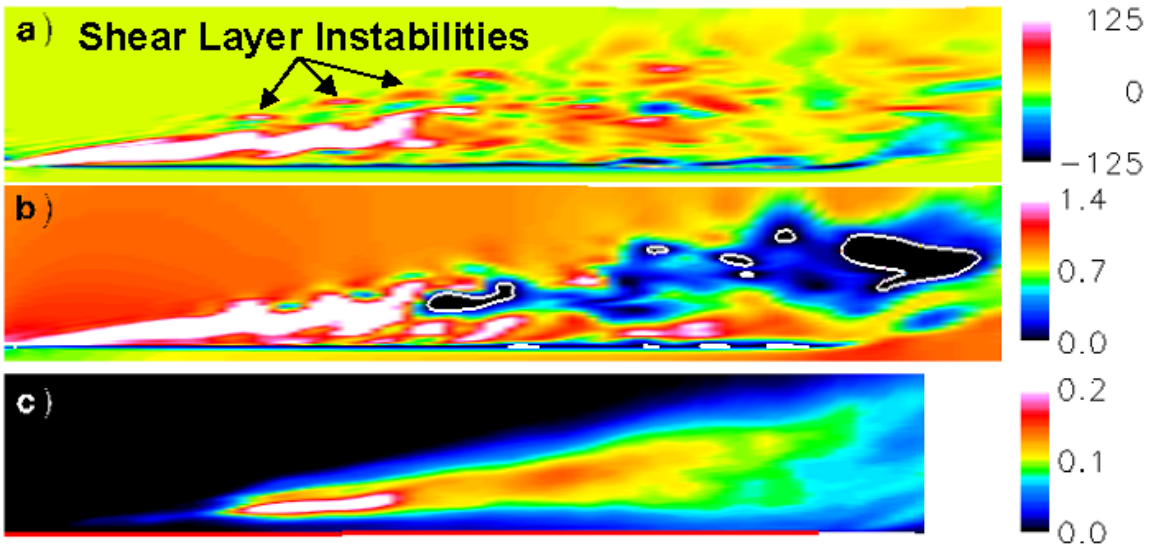

Figure 16: Instantaneous vortex structure on a plane through the vortex core a) axial vorticity, b) axial velocity, c) fluctuating kinetic energy.

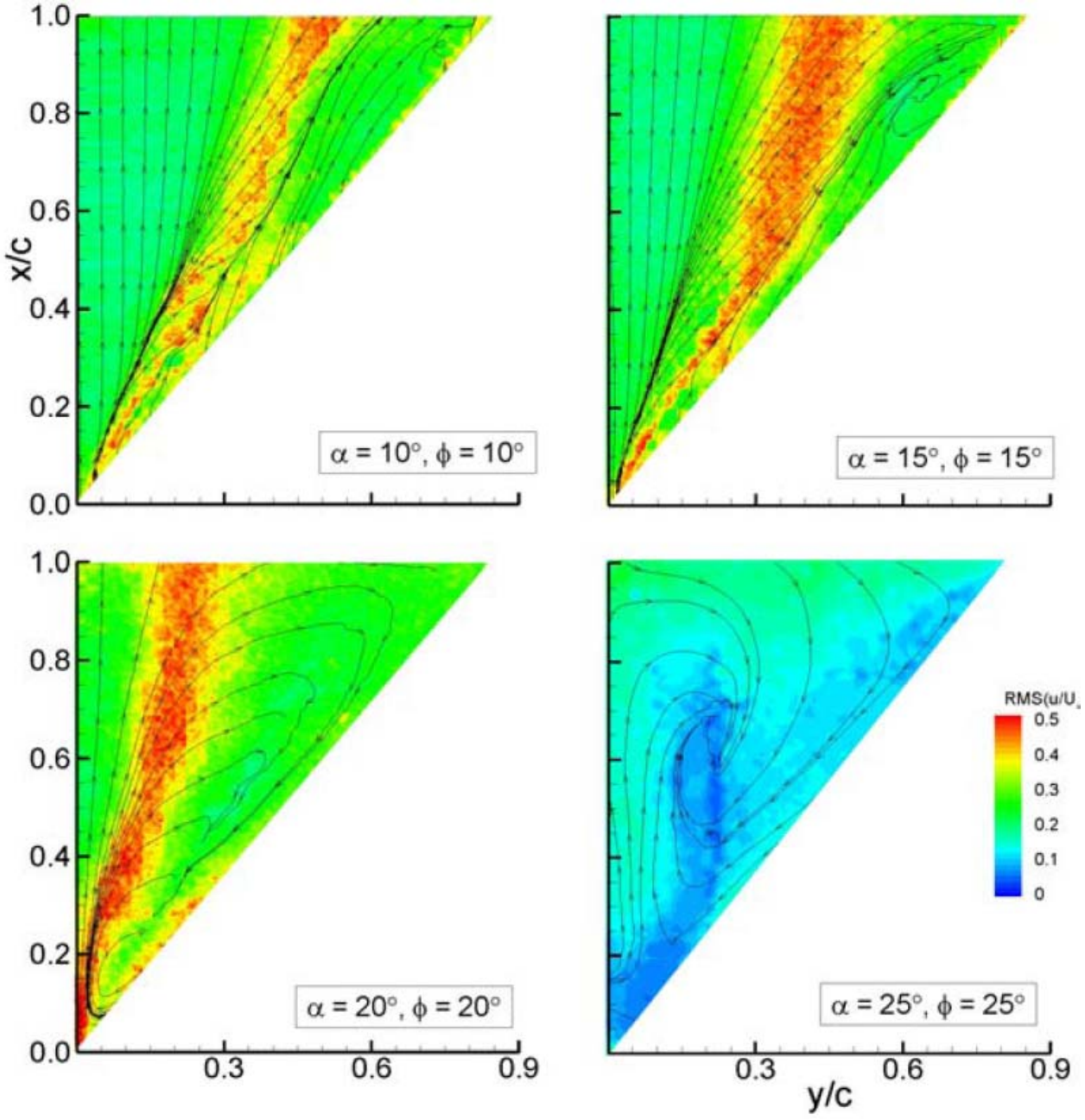

Figure 17: PIV measurements [30] of the rms velocity and streamline pattern on a plane parallel and adjacent to the surface of the wing.

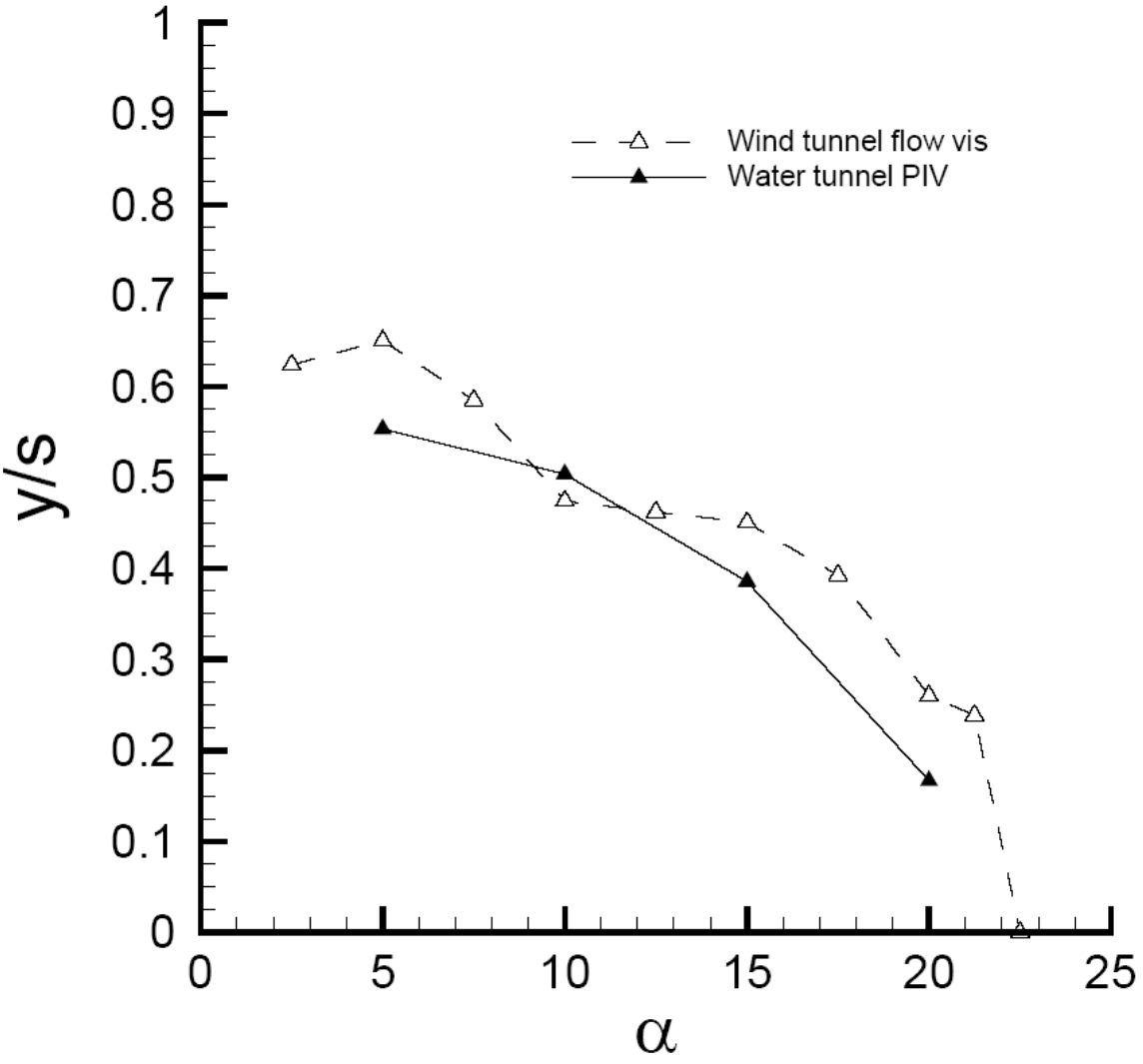

Figure 18: Variation of spanwise location of reattachment line with incidence for measurements in both a wind tunnel and water channel.

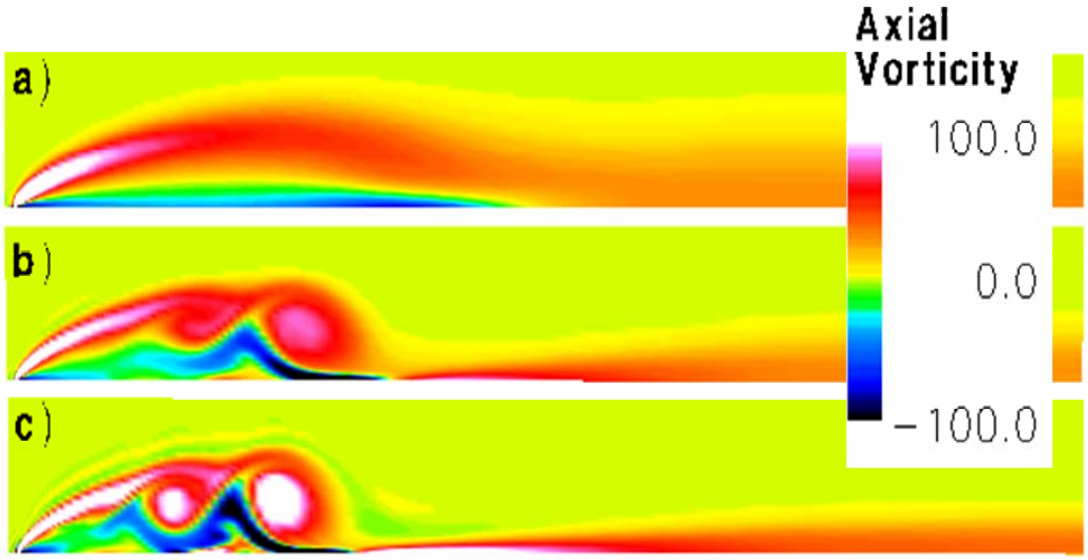

Figure 19: Influence of Reynolds number on dual vortex structure a) Re=10,000, b) Re=20,000, c) Re=50,000

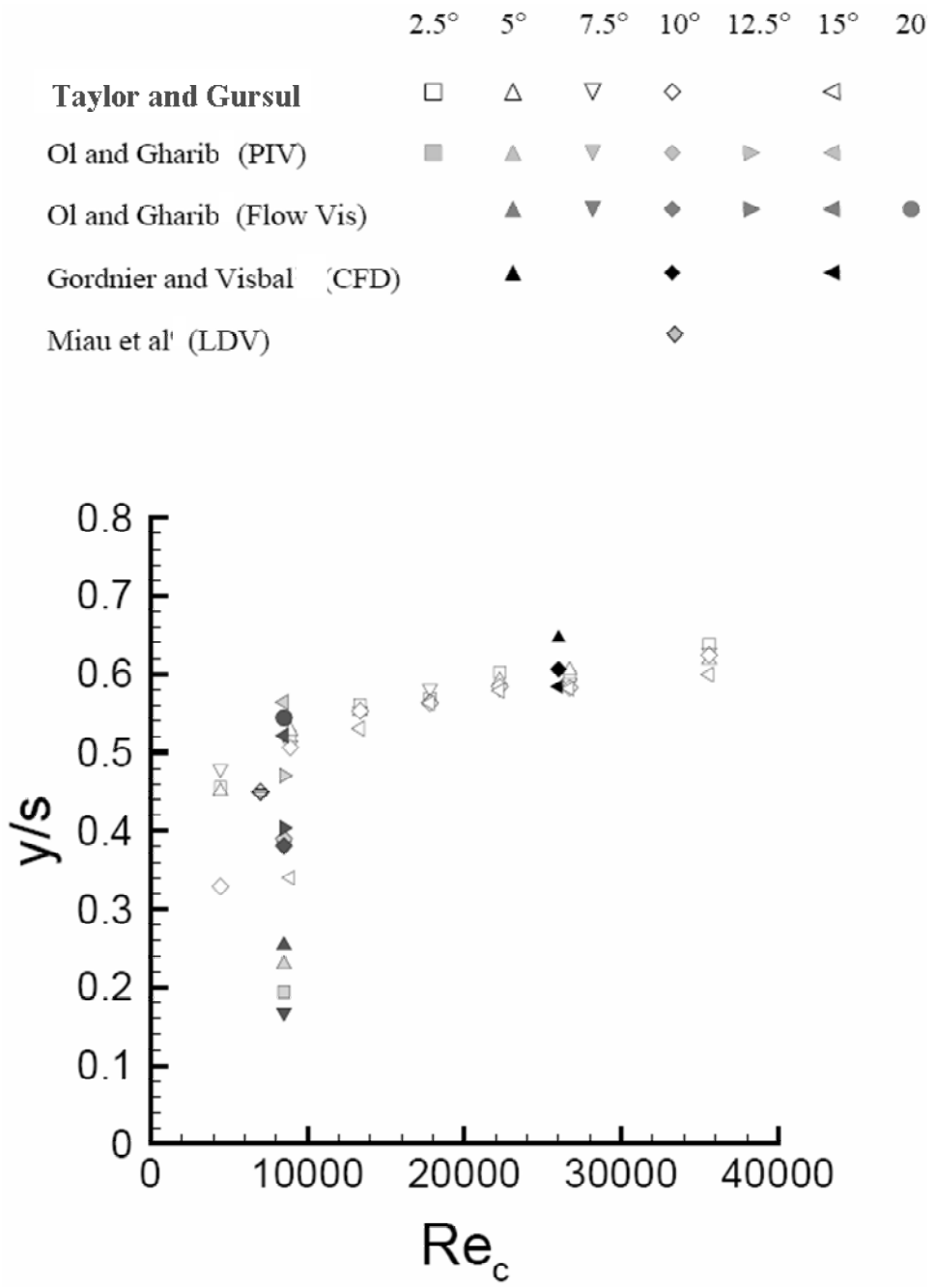

Figure 20: Variation of spanwise location of vortex core with Reynolds number from various experiments and computations [10, 11, 16, 30]

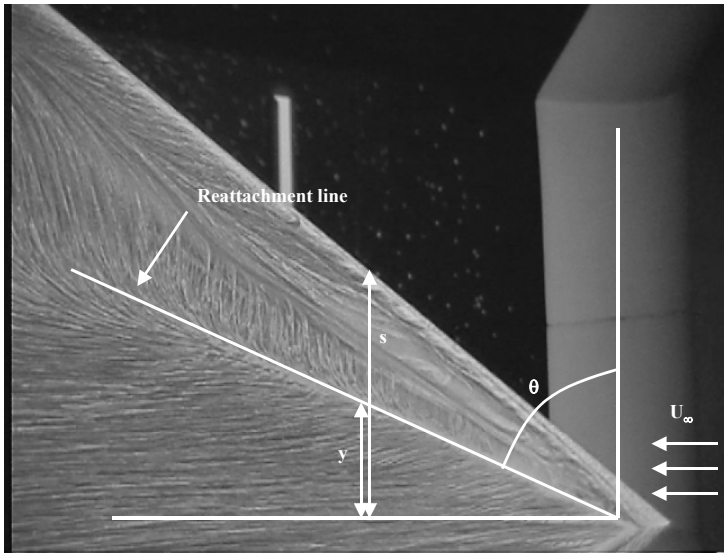

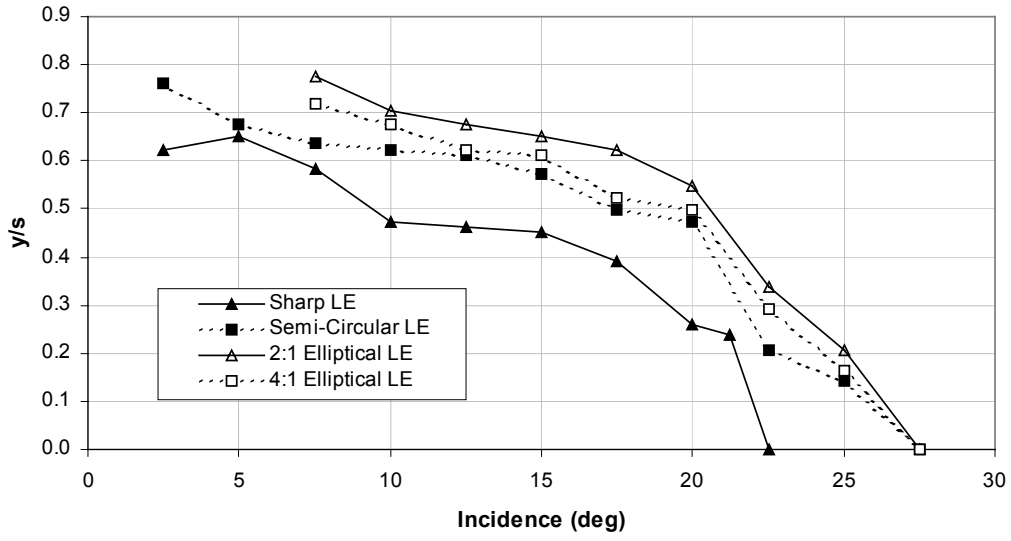

Figure 21: Location of reattachment line as a function of angle of attack for various leading-edge shapes, t/c=4%.

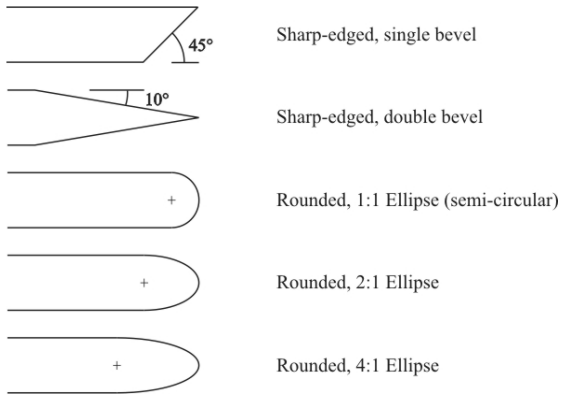

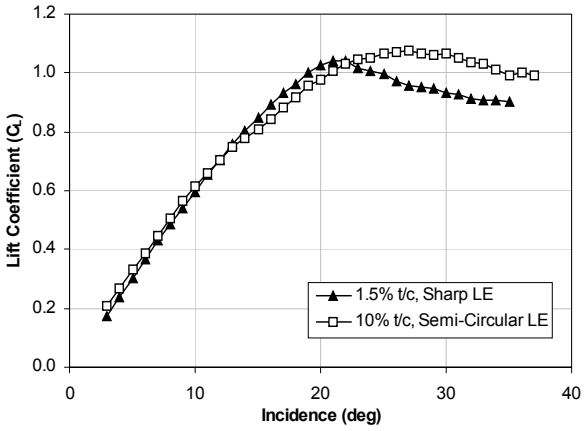

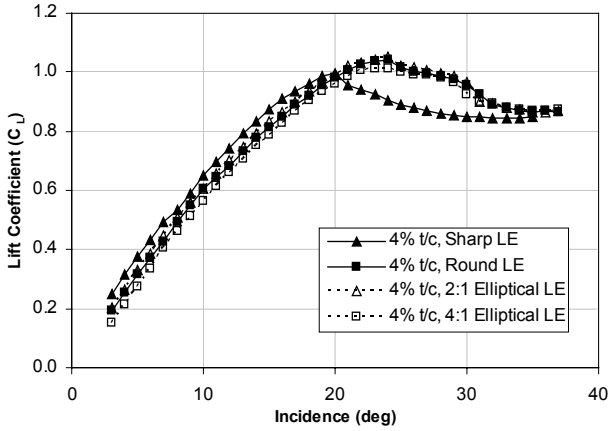

Figure 22: Variation of lift coefficient with angle of attack for various leading-edge shapes and thickness.

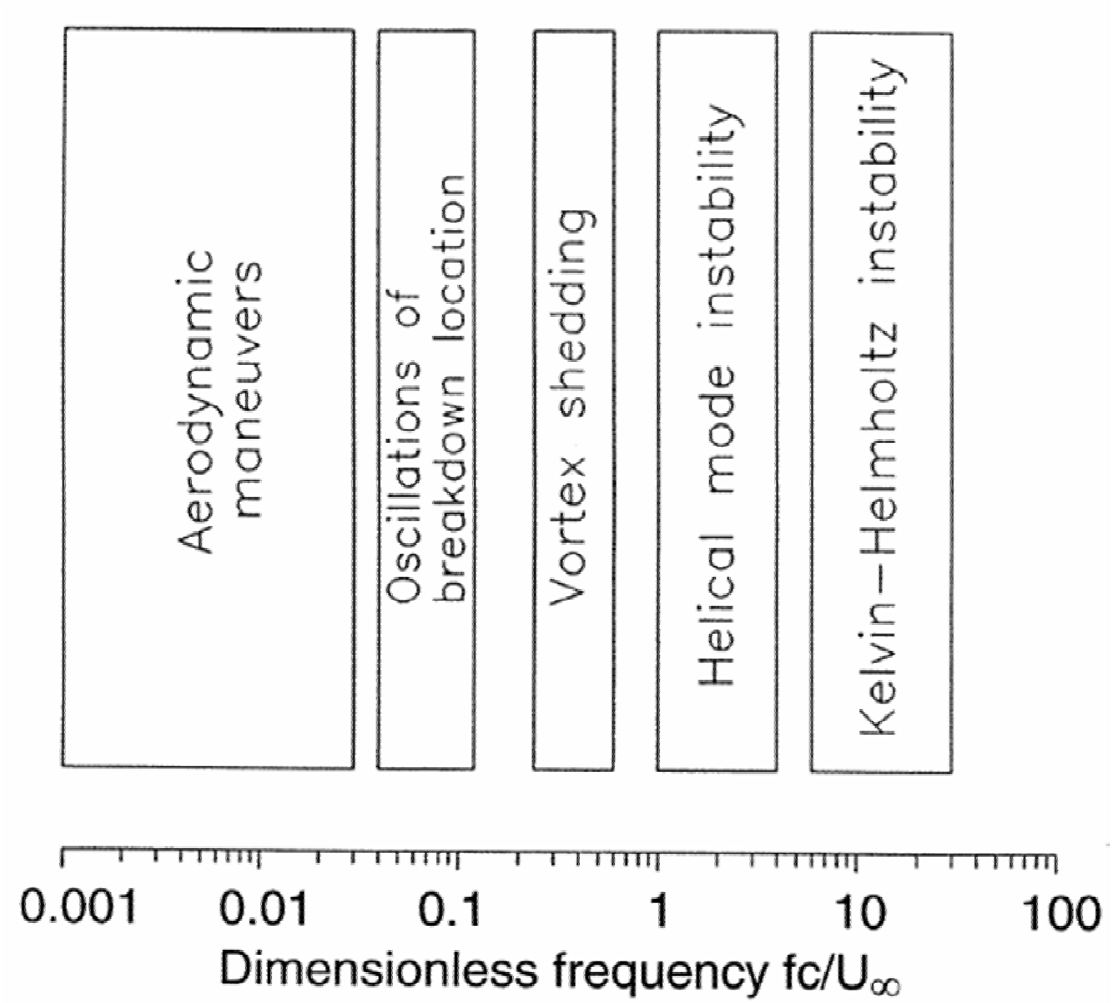

Figure 23: Spectrum of unsteady flow phenomena over delta wings as a function of dimensionless frequency.

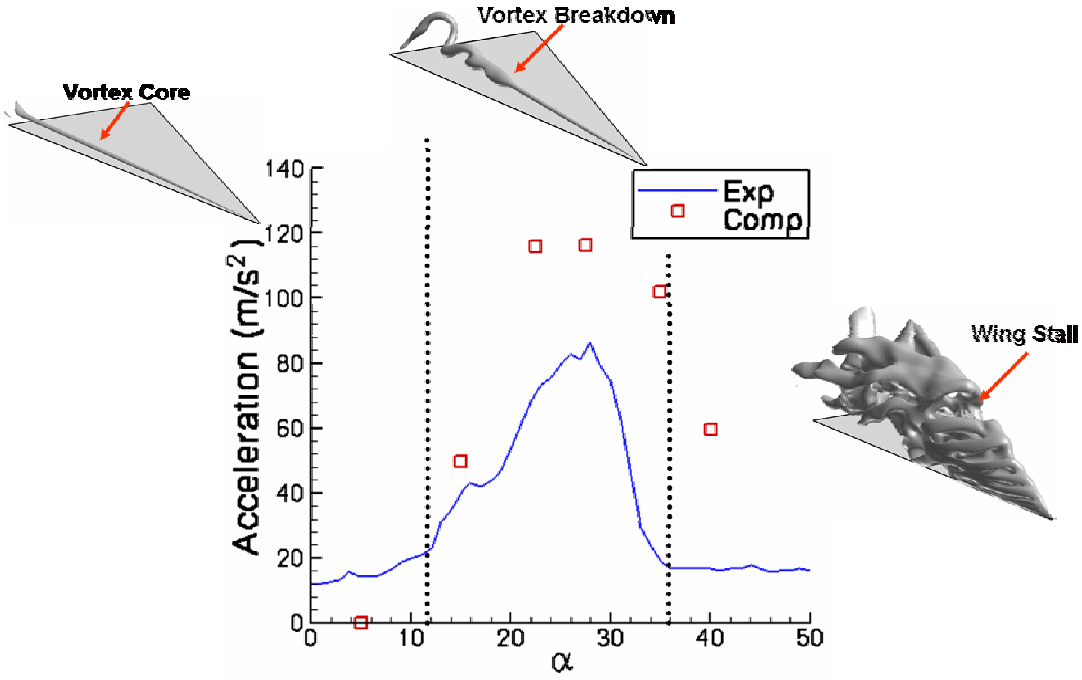

Figure 24: Variation of wingtip rms acceleration as a function of angle of attack for a Λ=60° sweep half delta wing model.

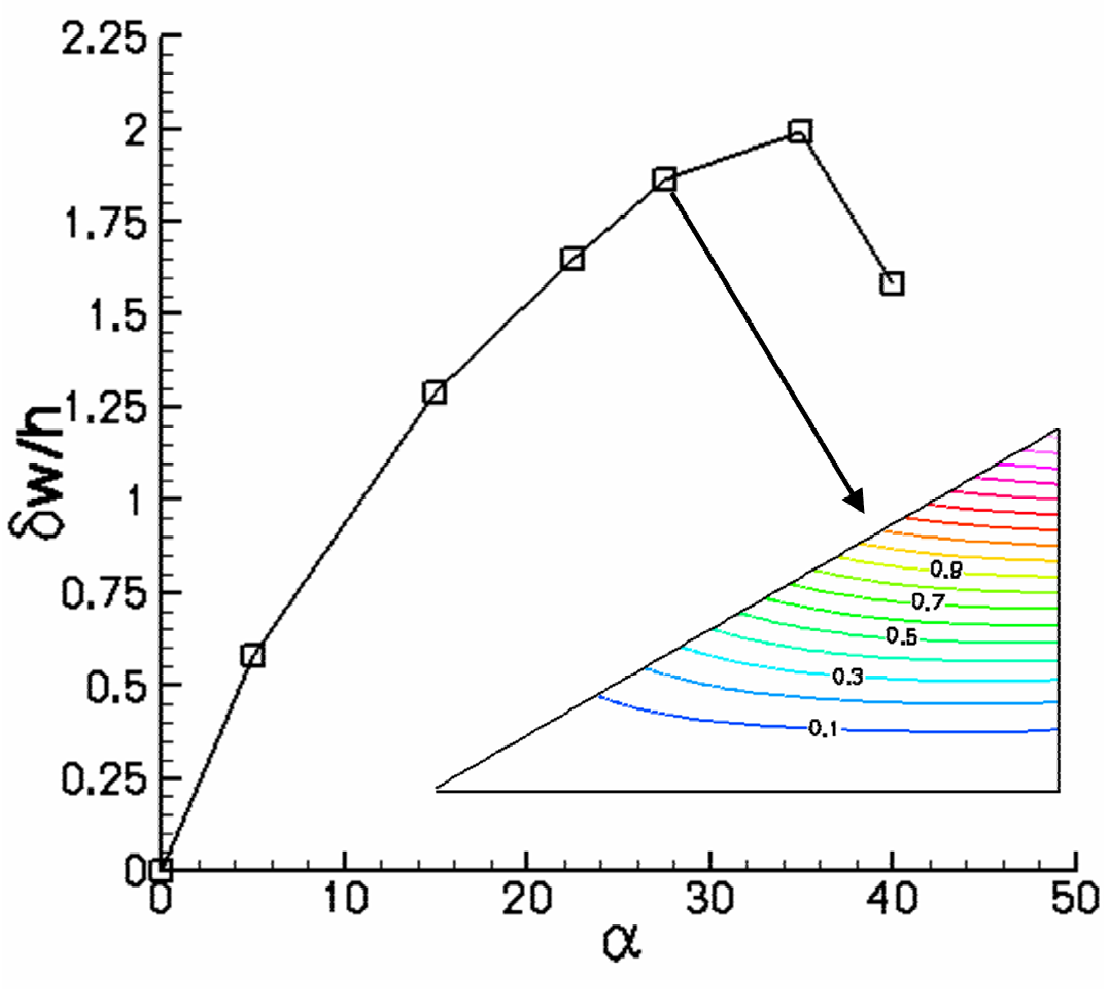

Figure 25: Mean wingtip deflection as a function of angle of attack and the mean deflection of a Λ=60° sweep wing for at α=27.5°.

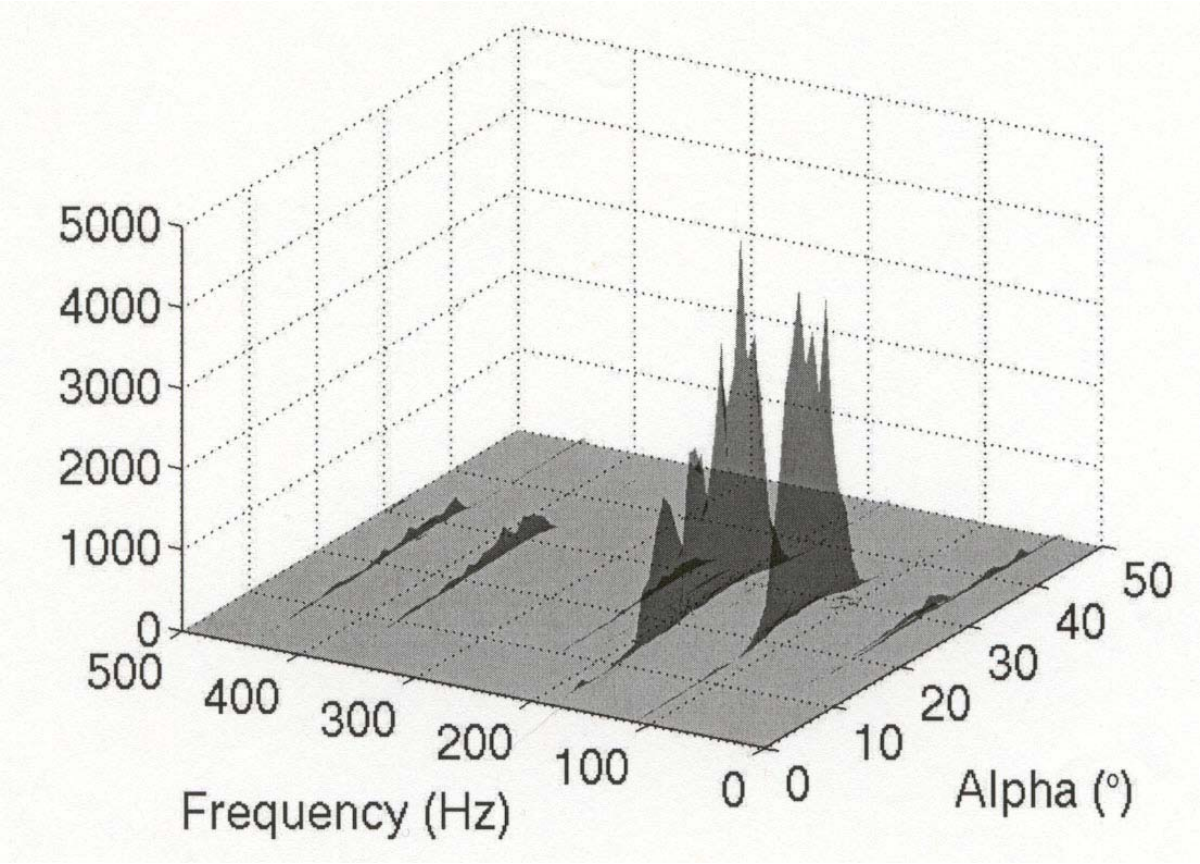

Figure 26: Three-dimensional spectra as a function of frequency and angle of attack for the Λ=60° half delta wing model.

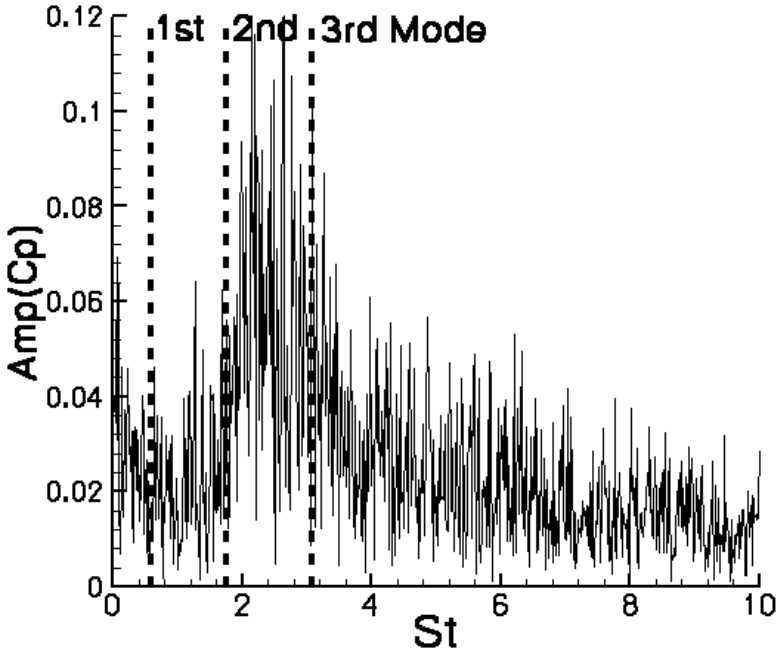

Figure 27: Spectral analysis of the pressure fluctuations under the vortex core for α=27.5°

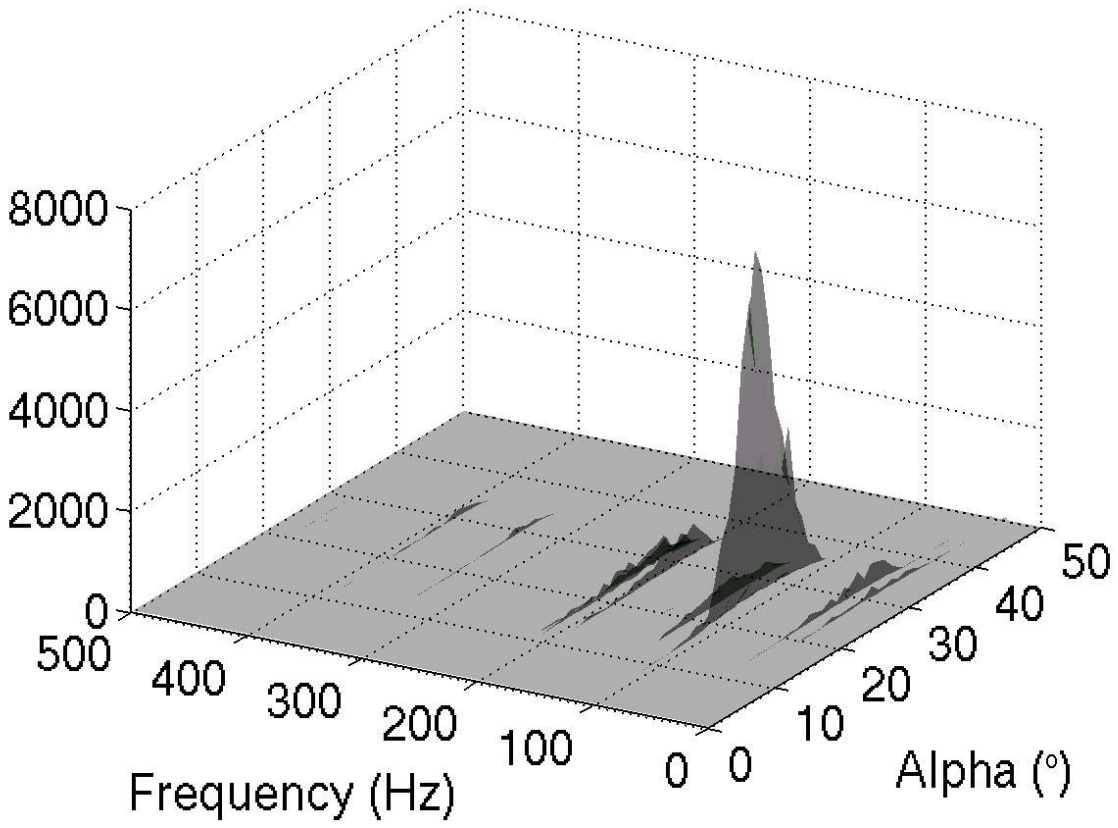

Figure 28: Three-dimensional spectra as a function of frequency and angle of attack for the Λ=60° full delta wing model.

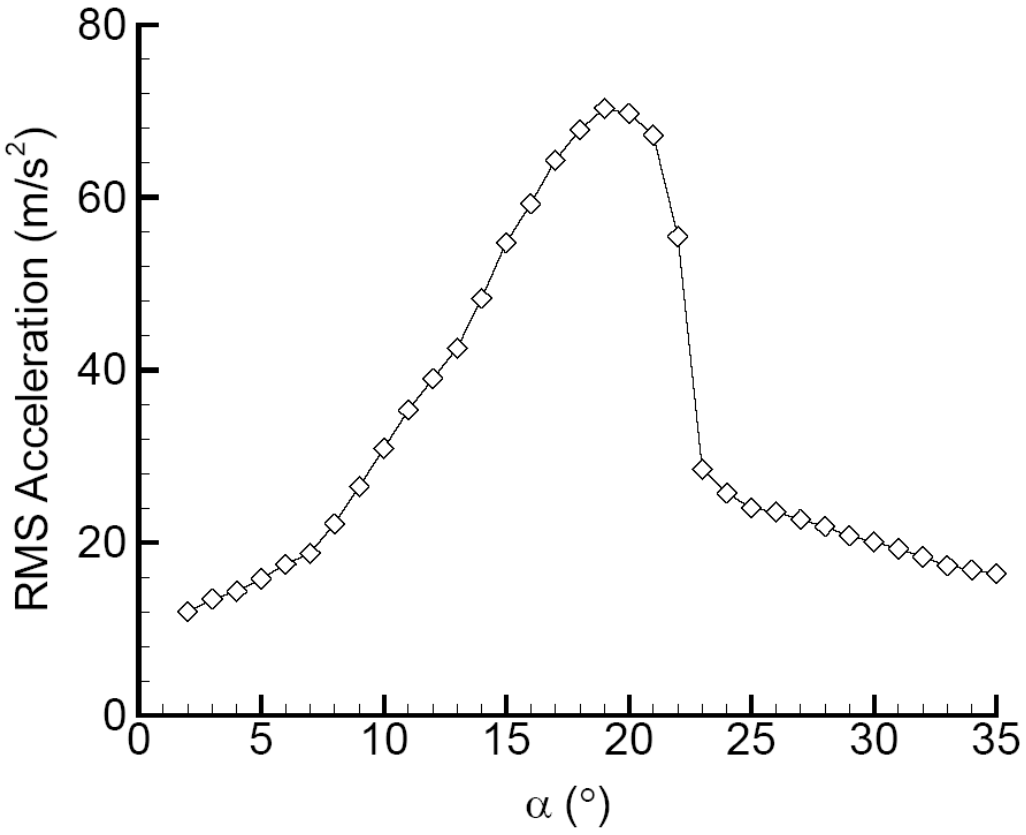

Figure 29: Variation of wingtip rms acceleration as a function of angle of attack for a Λ=50° sweep half delta wing model.

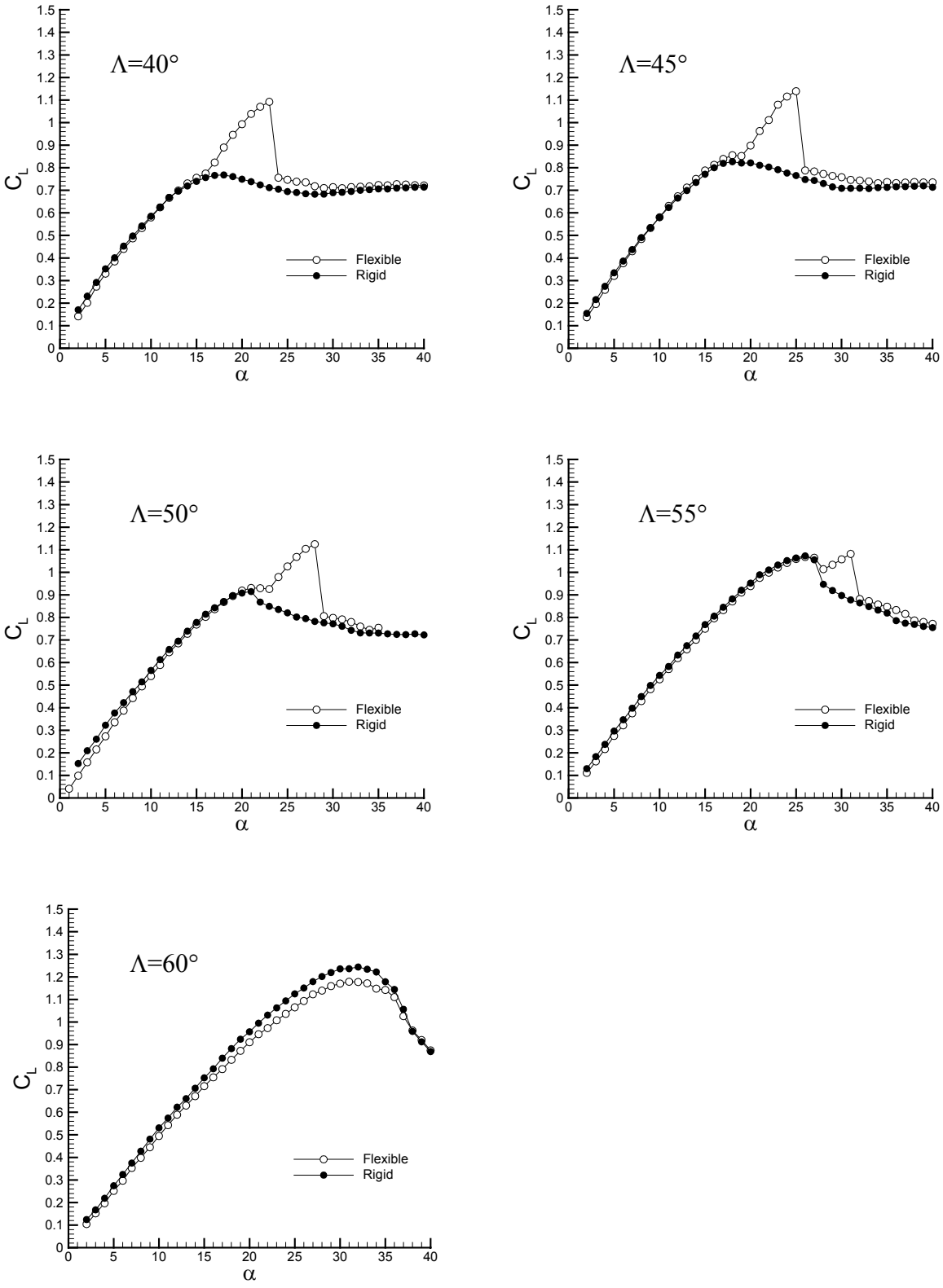

Figure 30: Variation of lift coefficient as a function of angle of attack and sweep angle for rigid and flexible wings.

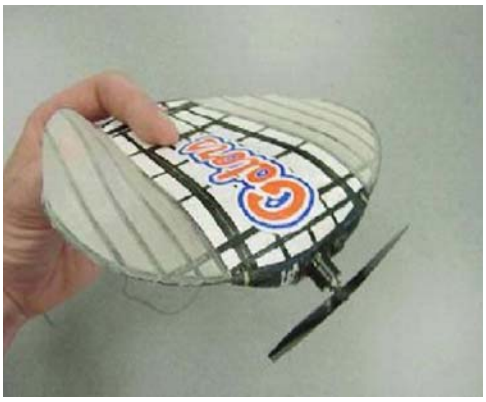

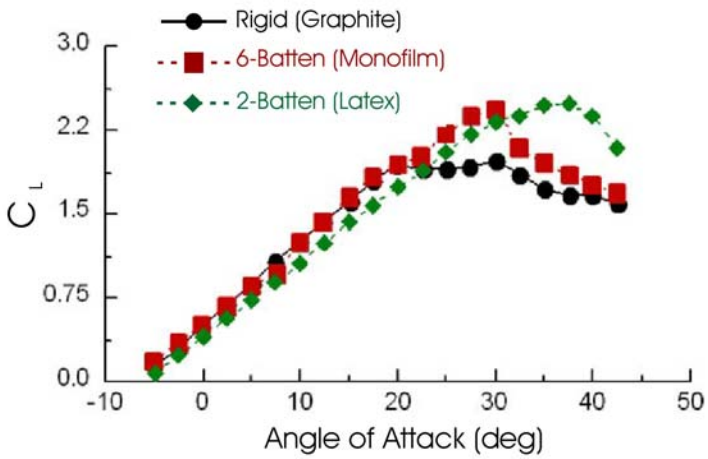

Figure 31: MAV with membrane wing (top); lift coefficient versus angle of attack (bottom) [65].

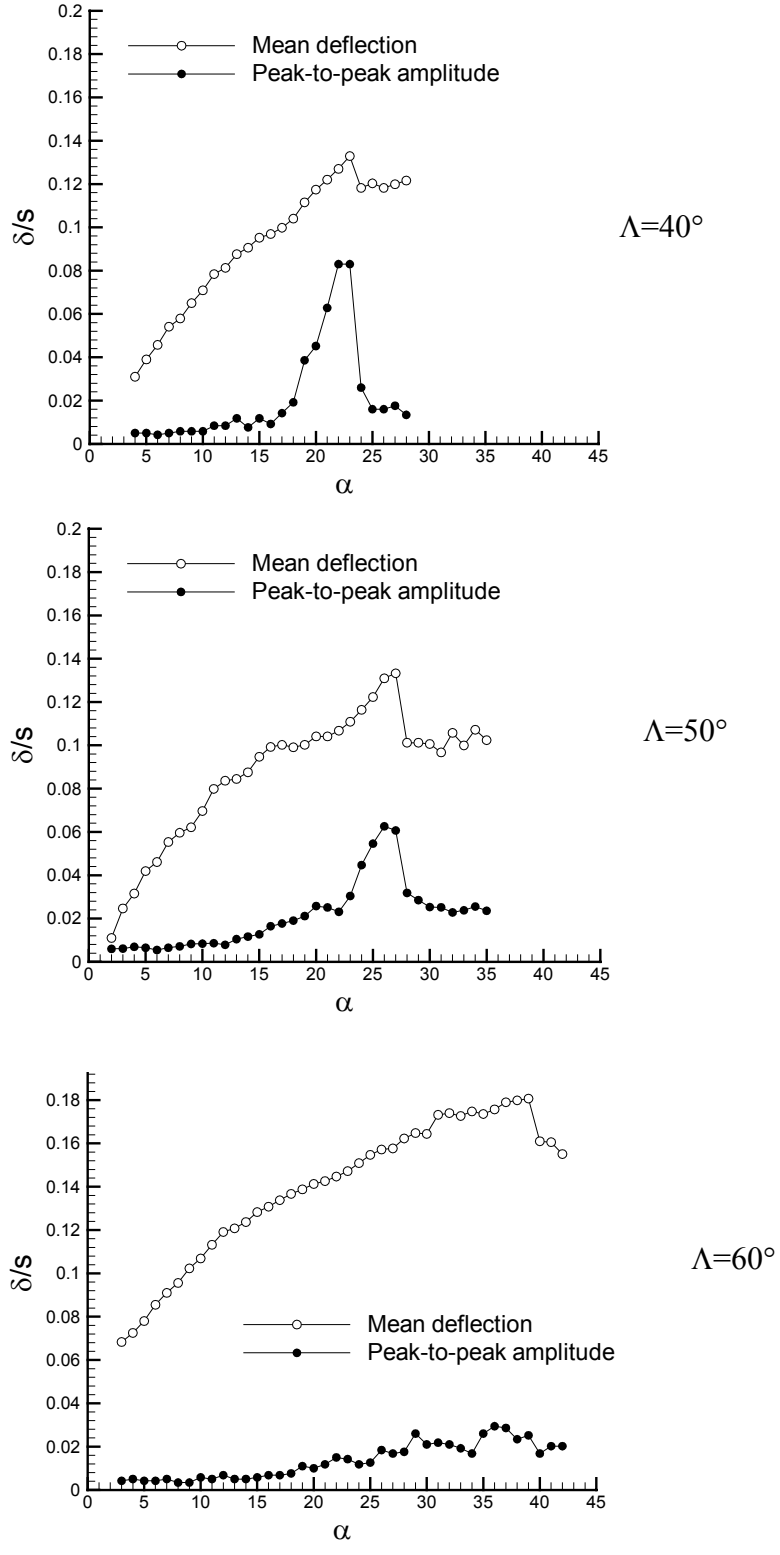

Figure 32: Variation of mean and amplitude of wing tip deformation.

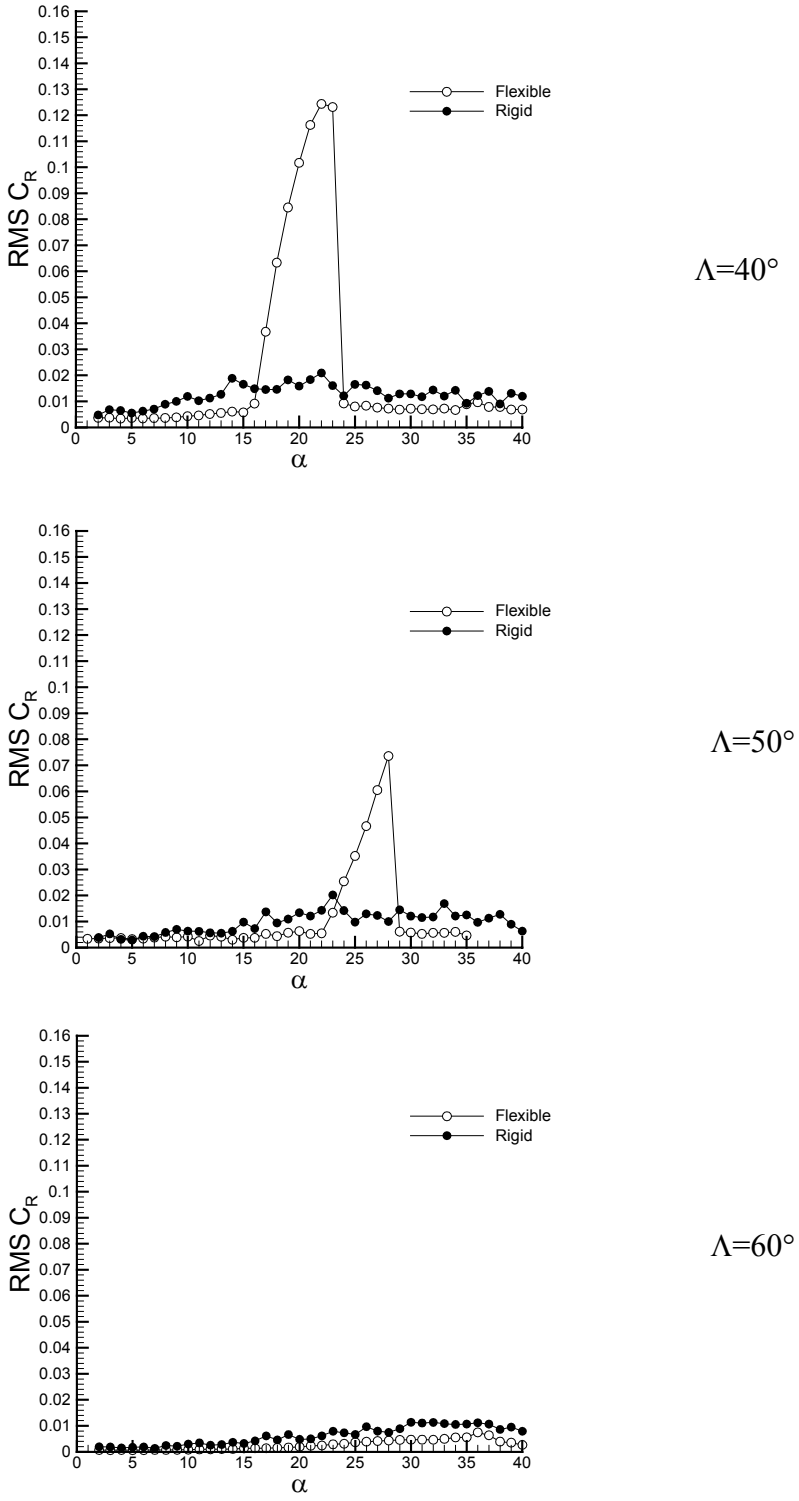

Figure 33: Variation of the root-mean-square rolling moment coefficient as a function of angle of attack.

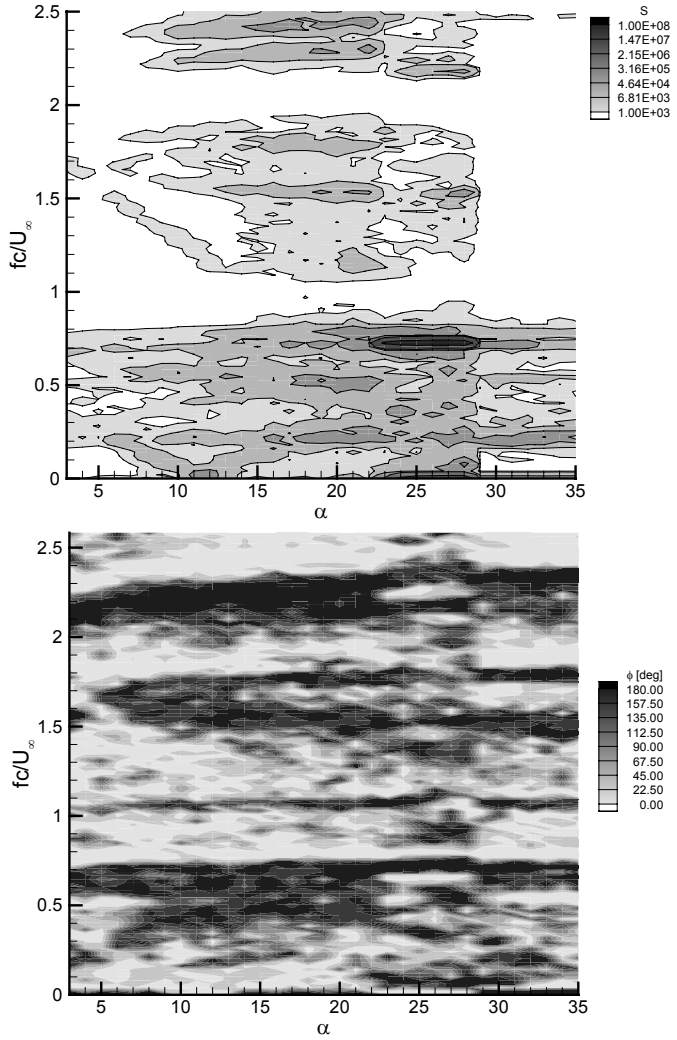

Figure 34: Contours of cross-spectral amplitude (top) and phase angle (bottom) between the wing tip accelerations as a function of frequency and incidence.

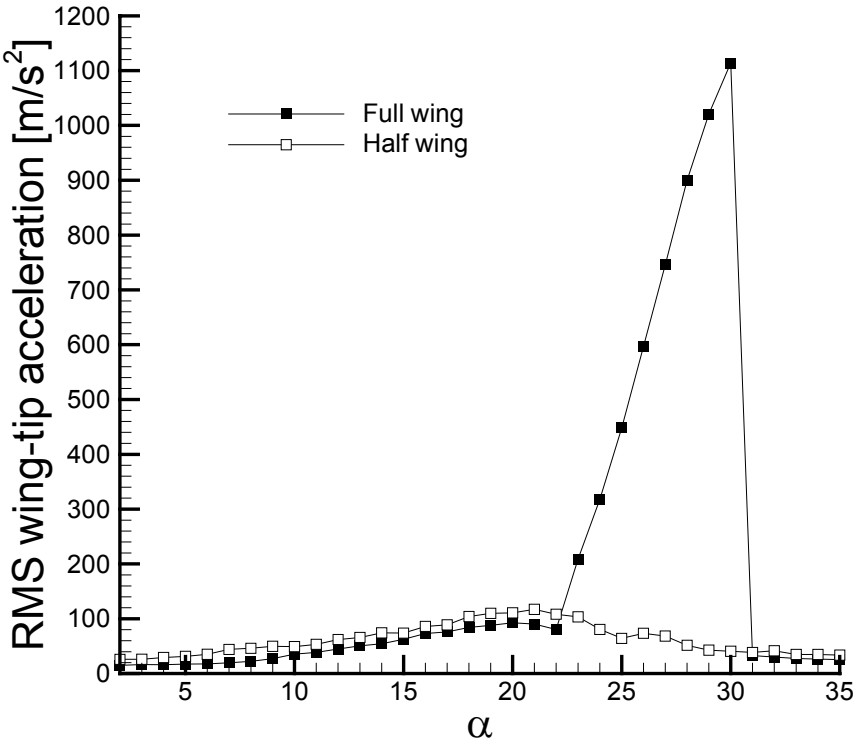

Figure 35: Variation of root-mean-square wing tip acceleration for 50° half-wing and full-wing models.

Rigid wing

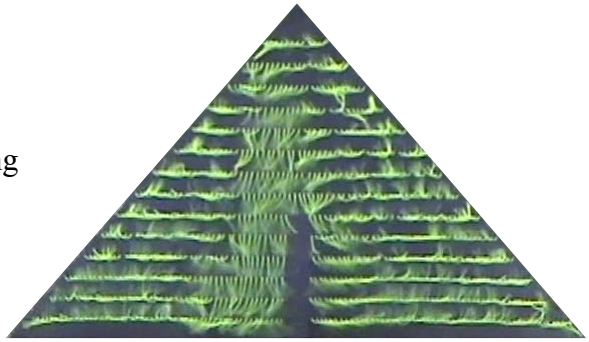

Flexible wing

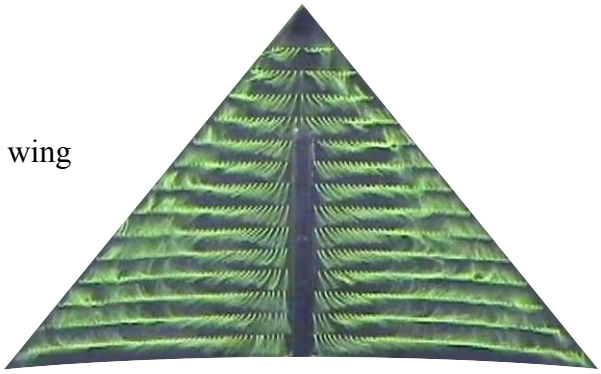

Figure 36: Tuft visualisation of surface flow patterns at α=27°.

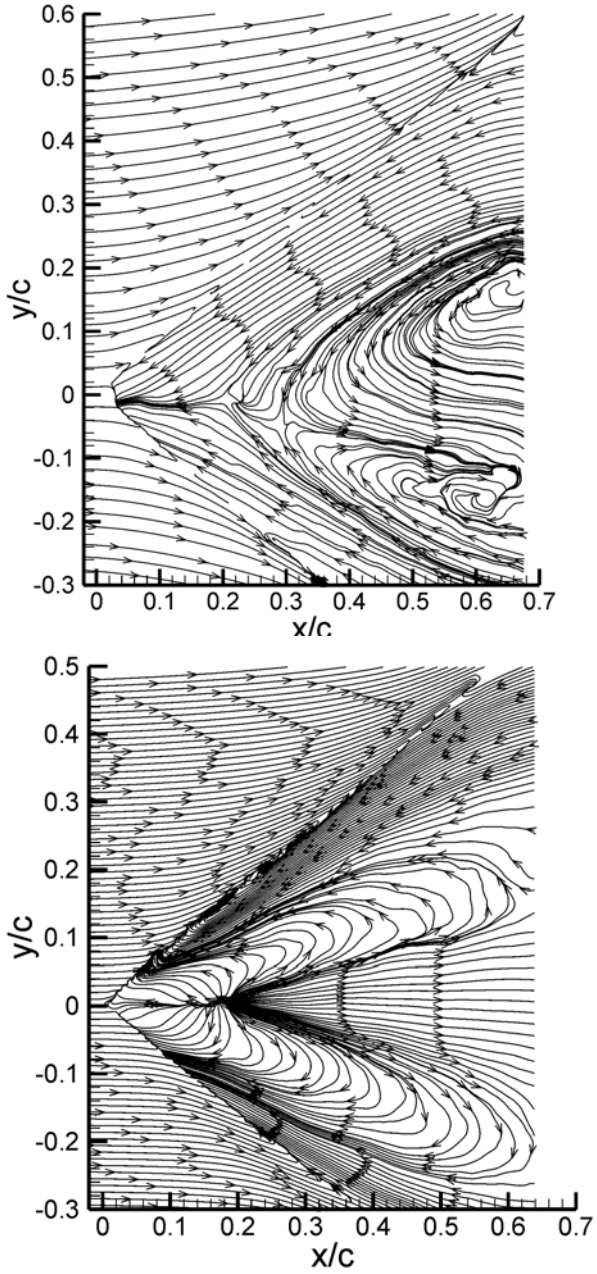

Figure 37: Time-averaged near surface streamlines for rigid (top) and flexible wings (bottom) at α=27°, Λ=50°.

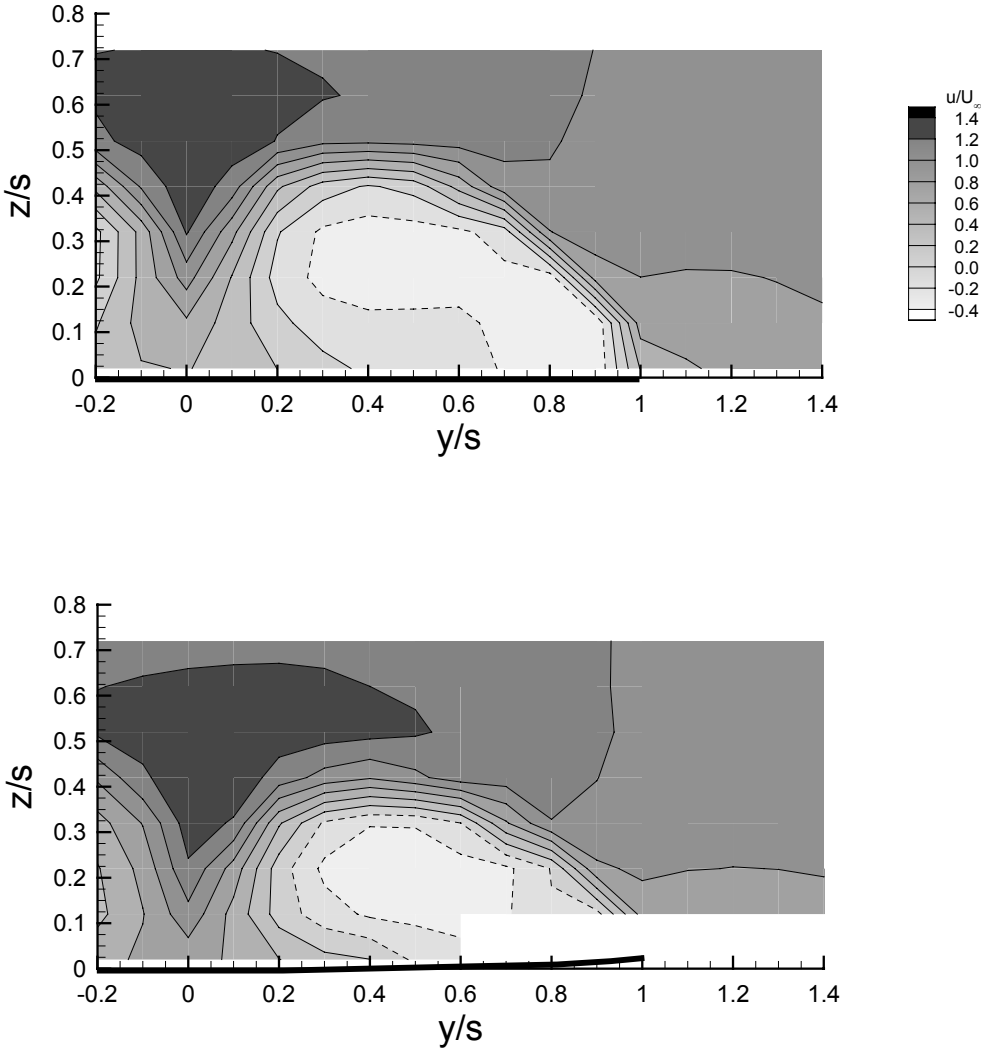

Figure 38: Contours of chordwise velocity component for rigid (top) and flexible wings (bottom), x/c=40%, α=25°, Λ=50°.

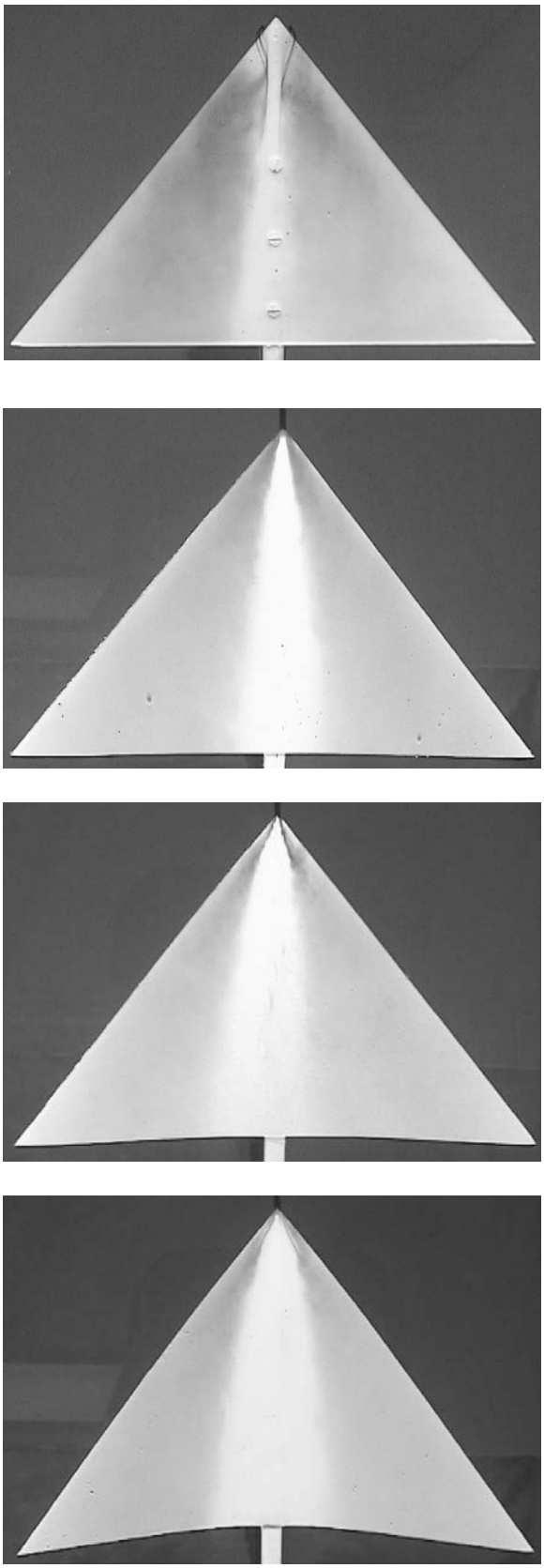

Figure 39: Flow visualization for rigid and flexible wings in water tunnel, $\alpha = 20°$.

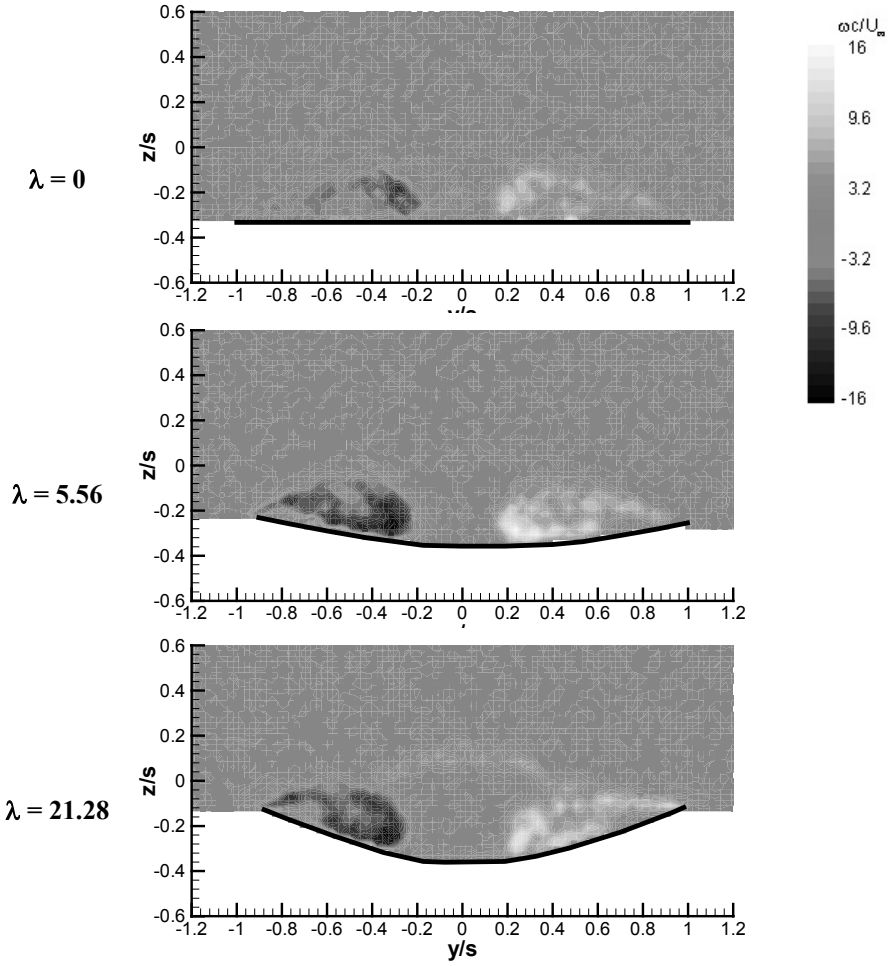

Figure 40: Magnitude of vorticity in a cross-flow plane at x/c=0.8 for rigid and flexible wings in water tunnel experiments, $\alpha = 20°$.

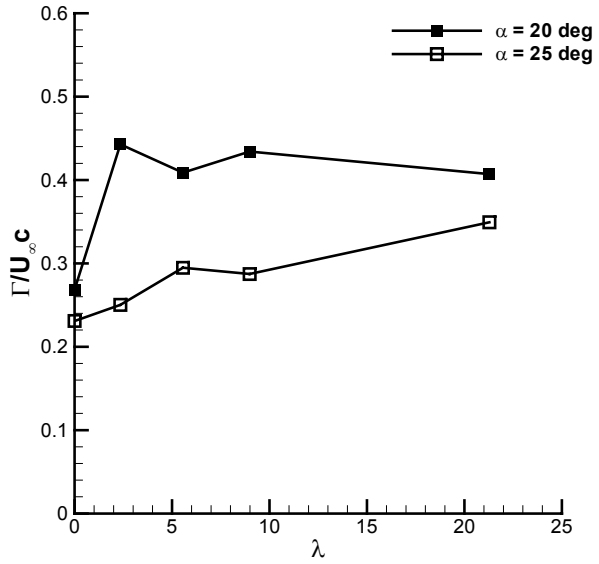

Figure 41: Variation of normalized circulation with wing flexibility.

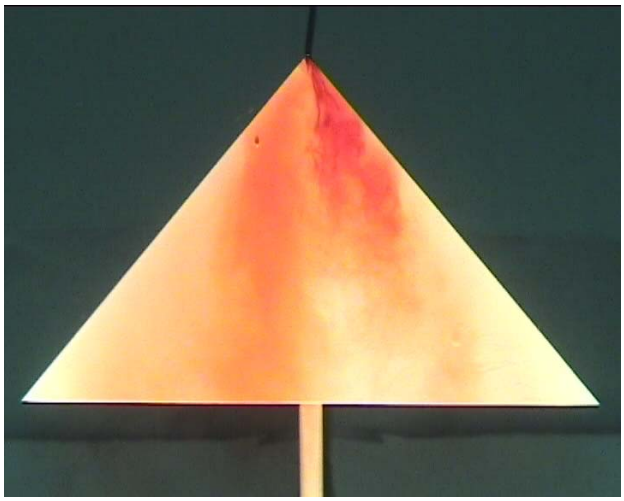

fc/U_∞ = 0

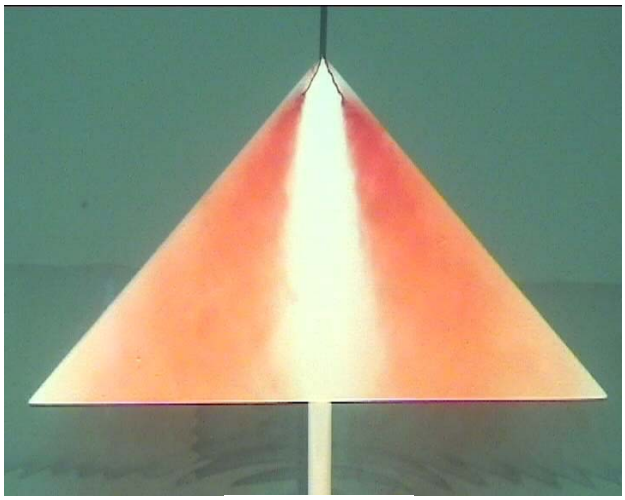

fc/U_∞ = 0.5

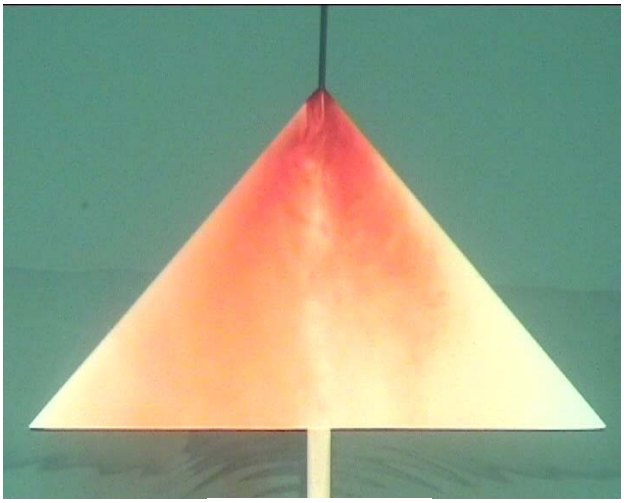

fc/U_∞ = 0.15

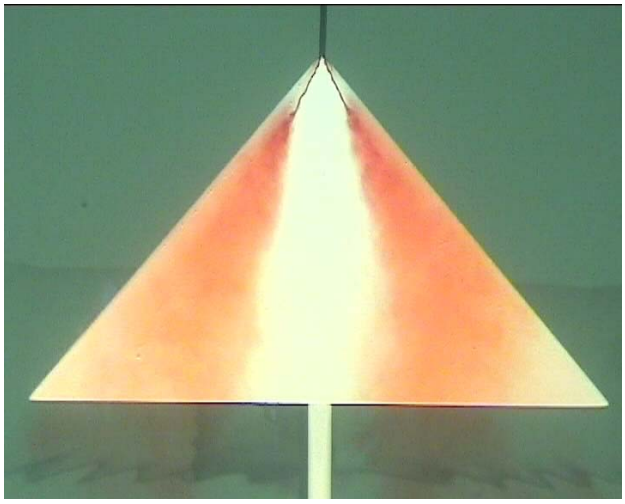

fc/U_∞ = 0.89

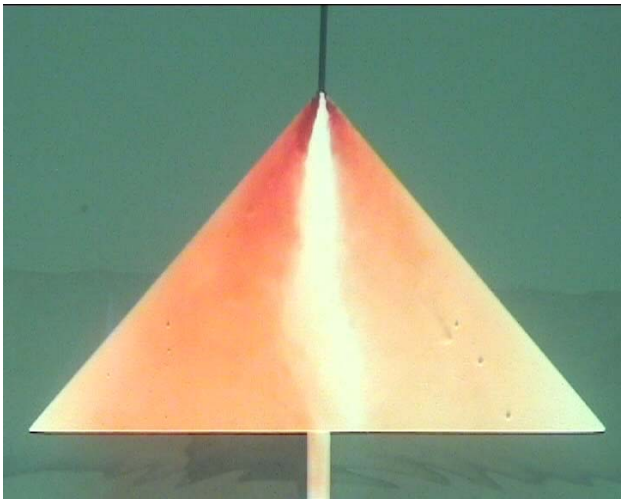

fc/U_∞ = 0.3

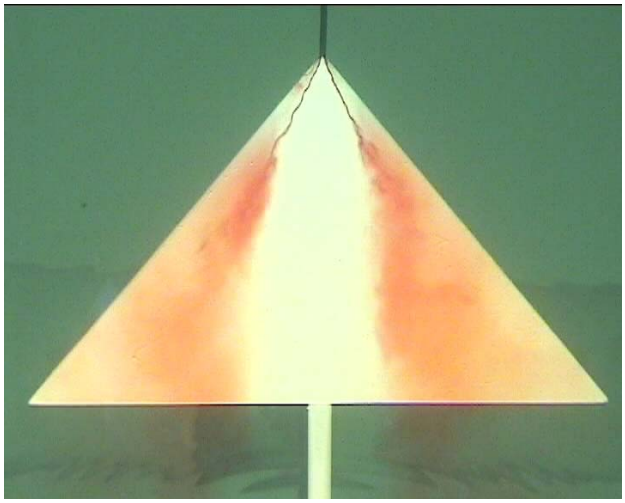

fc/U_∞ = 1.78

Figure 42: Flow visualization for a stationary and small-amplitude ($\Delta\phi$=5°) rolling wing in water tunnel experiments.

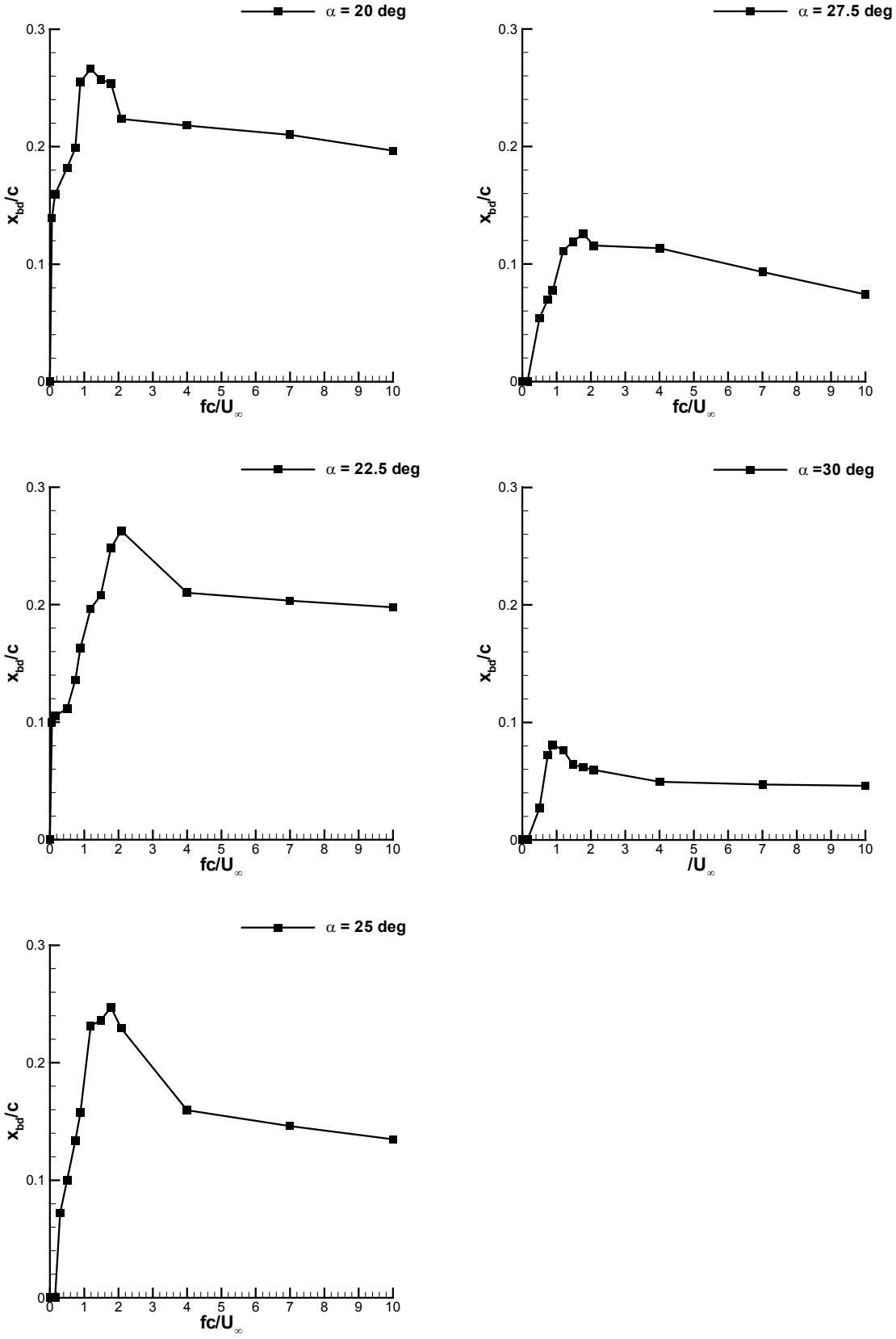

Figure 43: Variation of mean breakdown location as a function of dimensionless frequency for different angles of attack in water tunnel experiments.

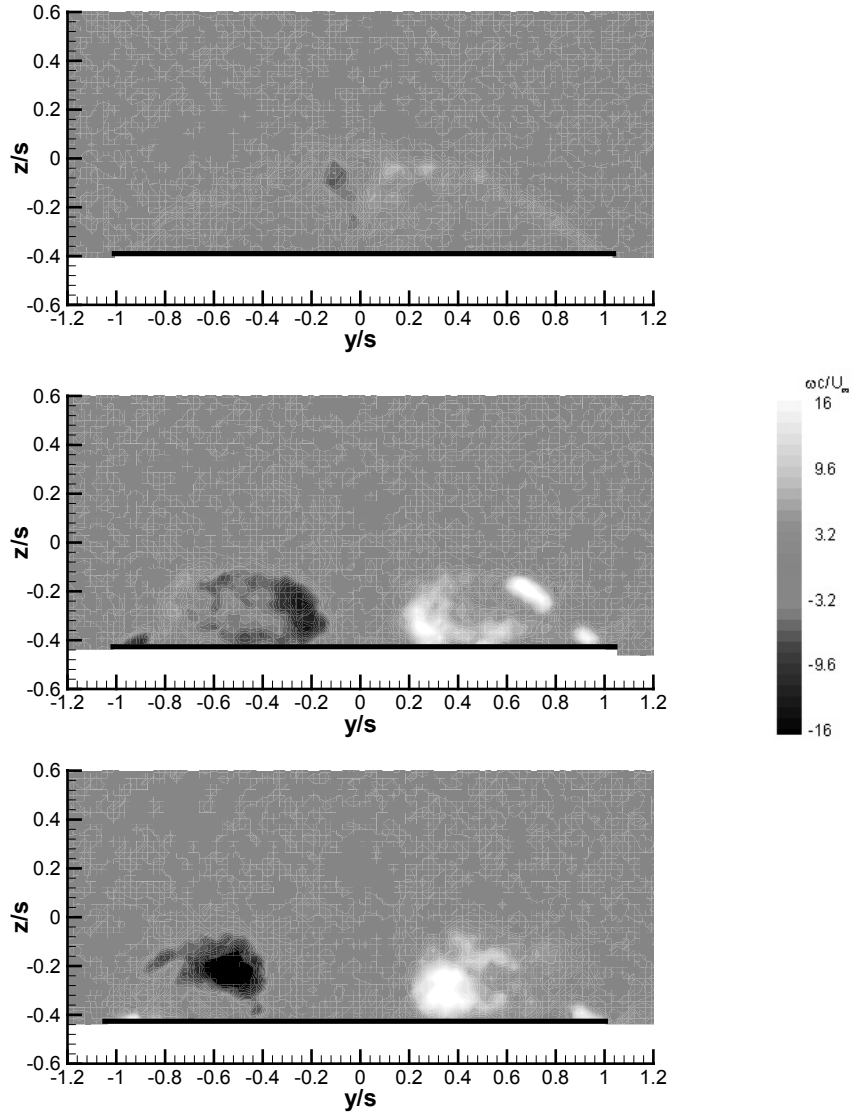

Figure 44: Magnitude of vorticity in a cross-flow plane at x/c=0.8 for stationary and rolling wings in water tunnel experiments, $\alpha = 25°$.

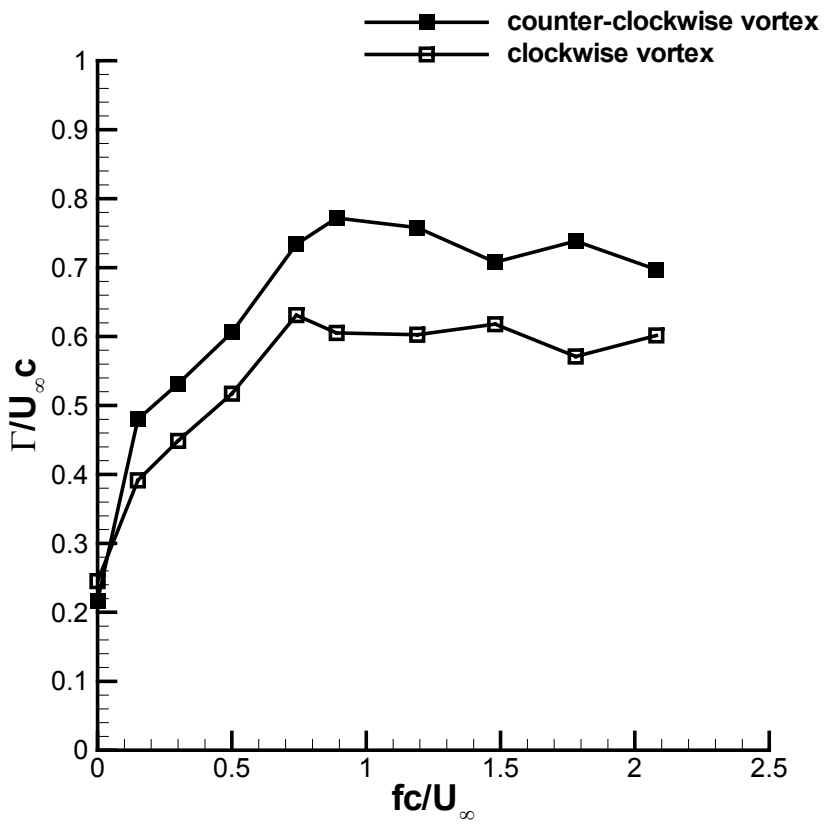

Figure 45: Variation of normalized circulation of vortical flow in a cross-flow plane at x/c=0.8 as a function of dimensionless frequency in water tunnel experiments, $\alpha = 25°$.

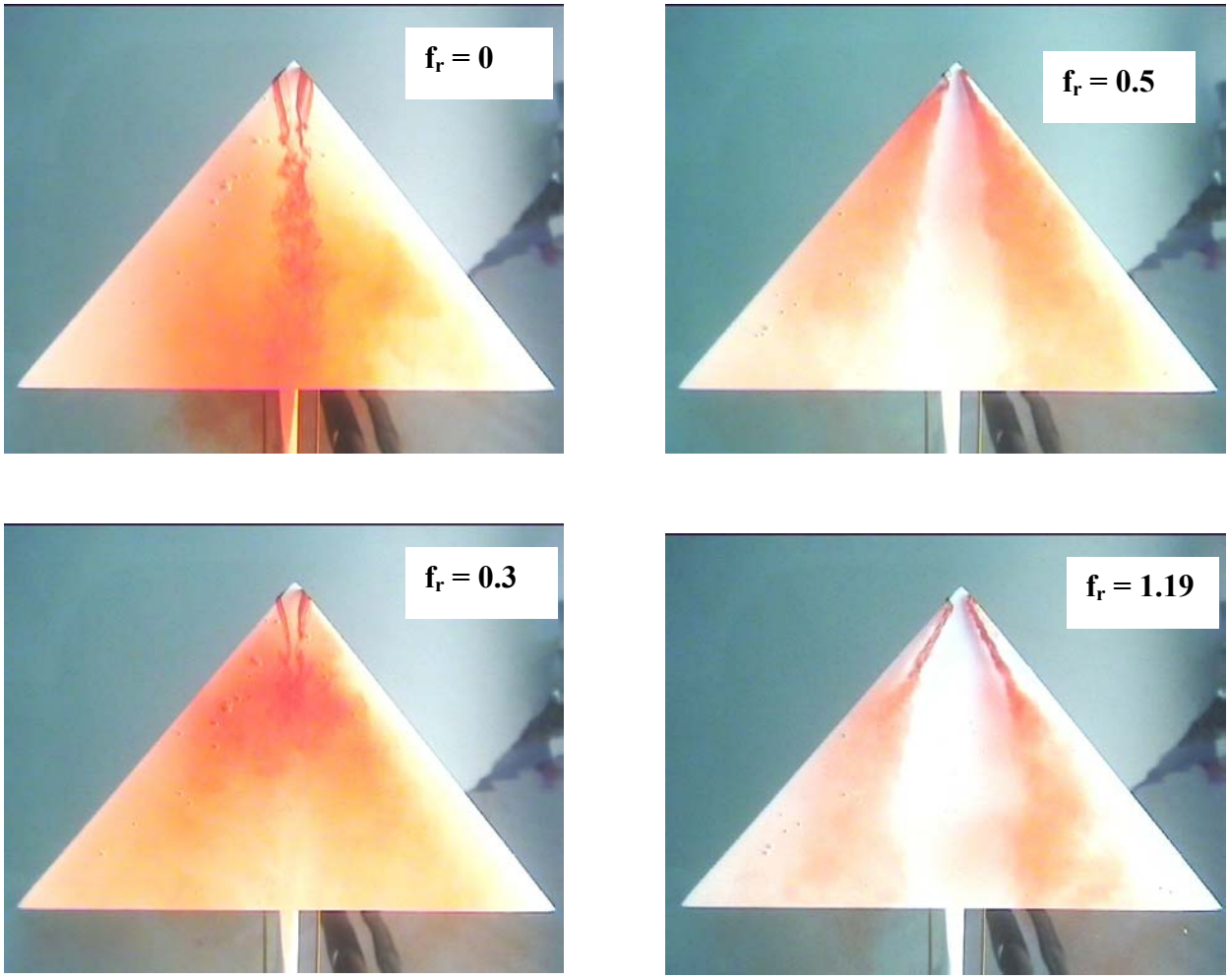

Figure 46: Flow visualization for a stationary and small amplitude ($\Delta\alpha$=1°) pitching wing for various reduced frequencies fc/U_∞, α=25°, Λ=50°.

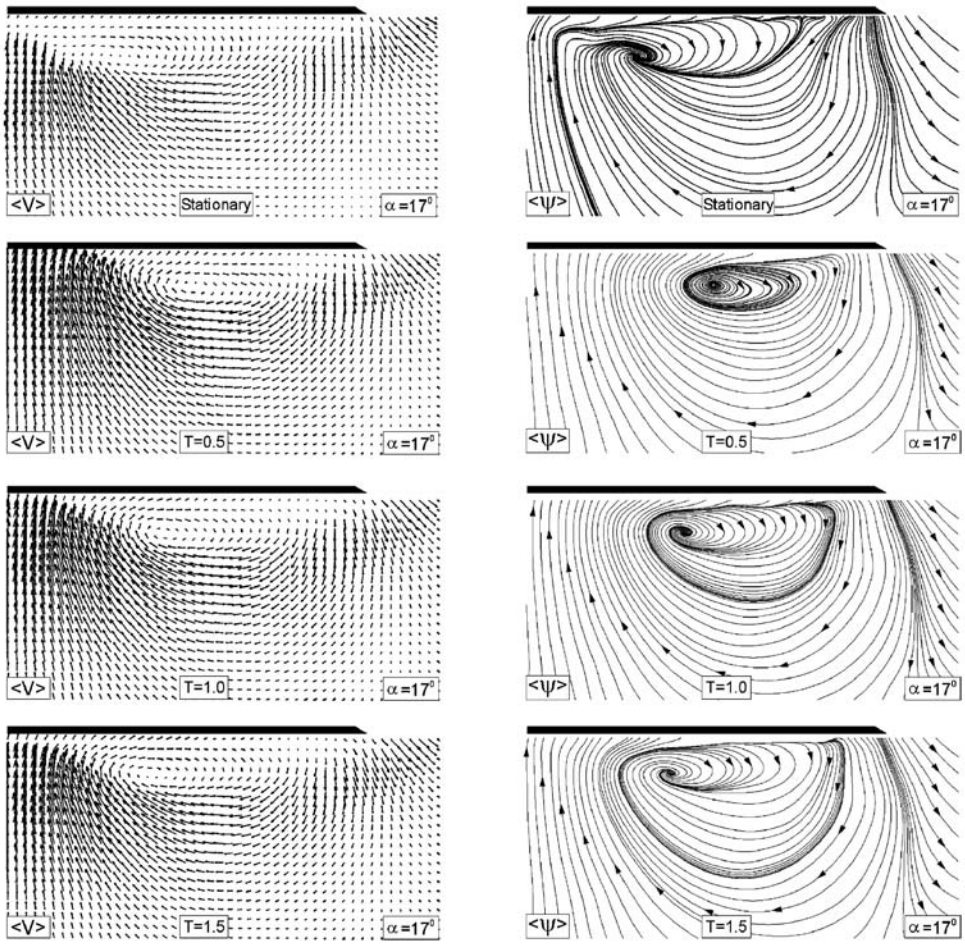

Figure 47: Effect of small amplitude pitching oscillations on time-averaged velocity and streamline patterns at x/c=0.8 for α=17°, Λ=38.7° [31].

fc/U_∞=0

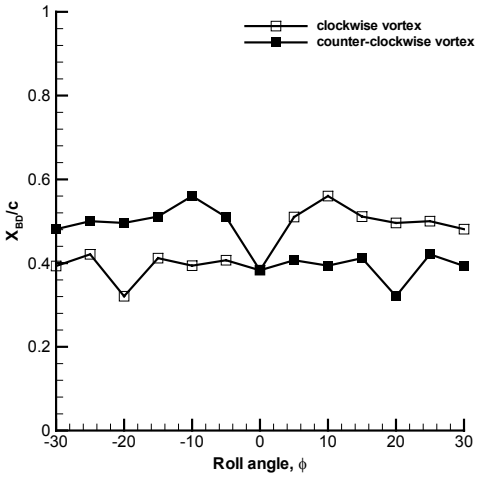

a)

fc/U_∞=0.015

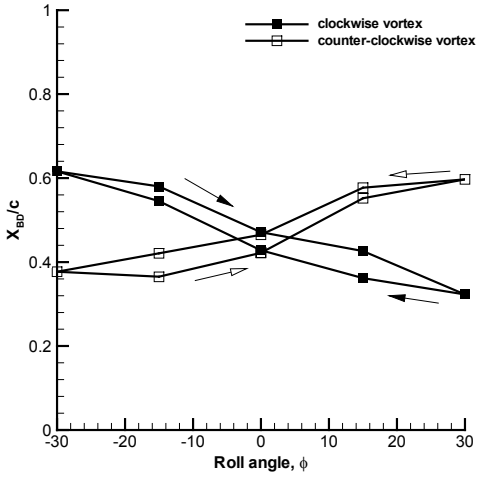

b)

fc/U_∞=0.15

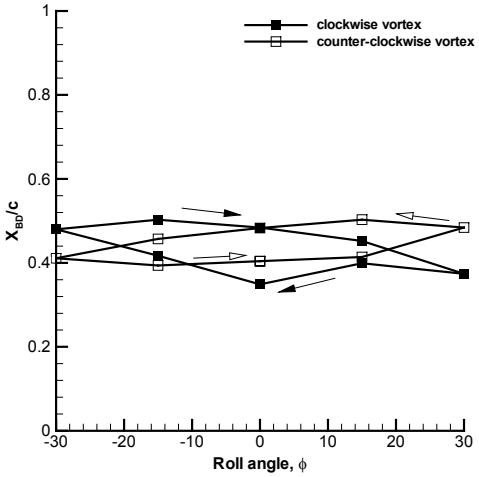

c)

Figure 48: Variation of the vortex breakdown position X_{BD}/c with the roll angle φ for different cases of the wing motion at α= 15° and for φ_{max} = 30°; a) static case; b) fc/U_∞=0.015; c) fc/U_∞=0.15.

fc/U∞=0

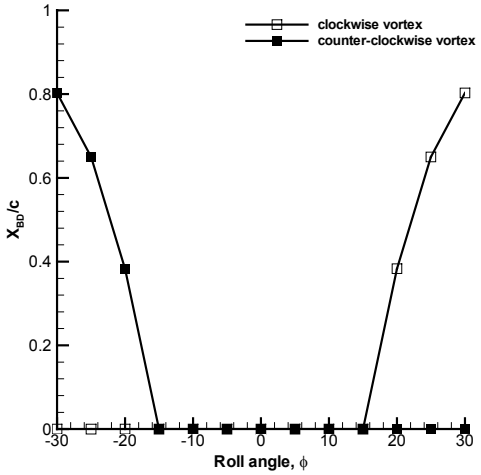

a)

fc/U∞=0.015

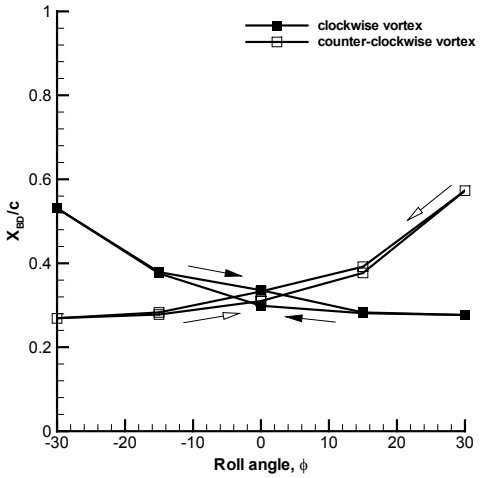

b)

fc/U∞=0.15

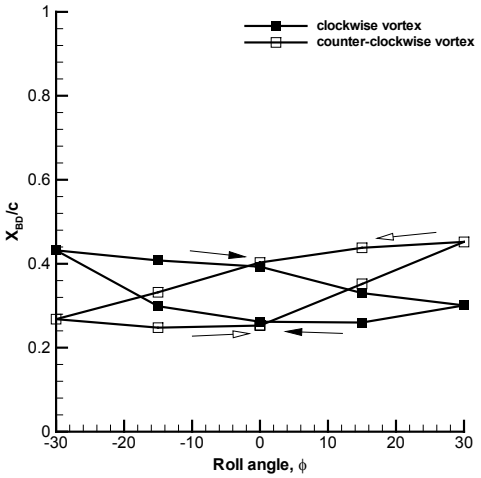

c)

Figure 49: Variation of the vortex breakdown position X_{BD}/c with the roll angle φ for different cases of the wing motion at α = 20° and for φ_{max} = 30°; a) static case; b) fc/U_∞=0.015; c) fc/U_∞=0.15.

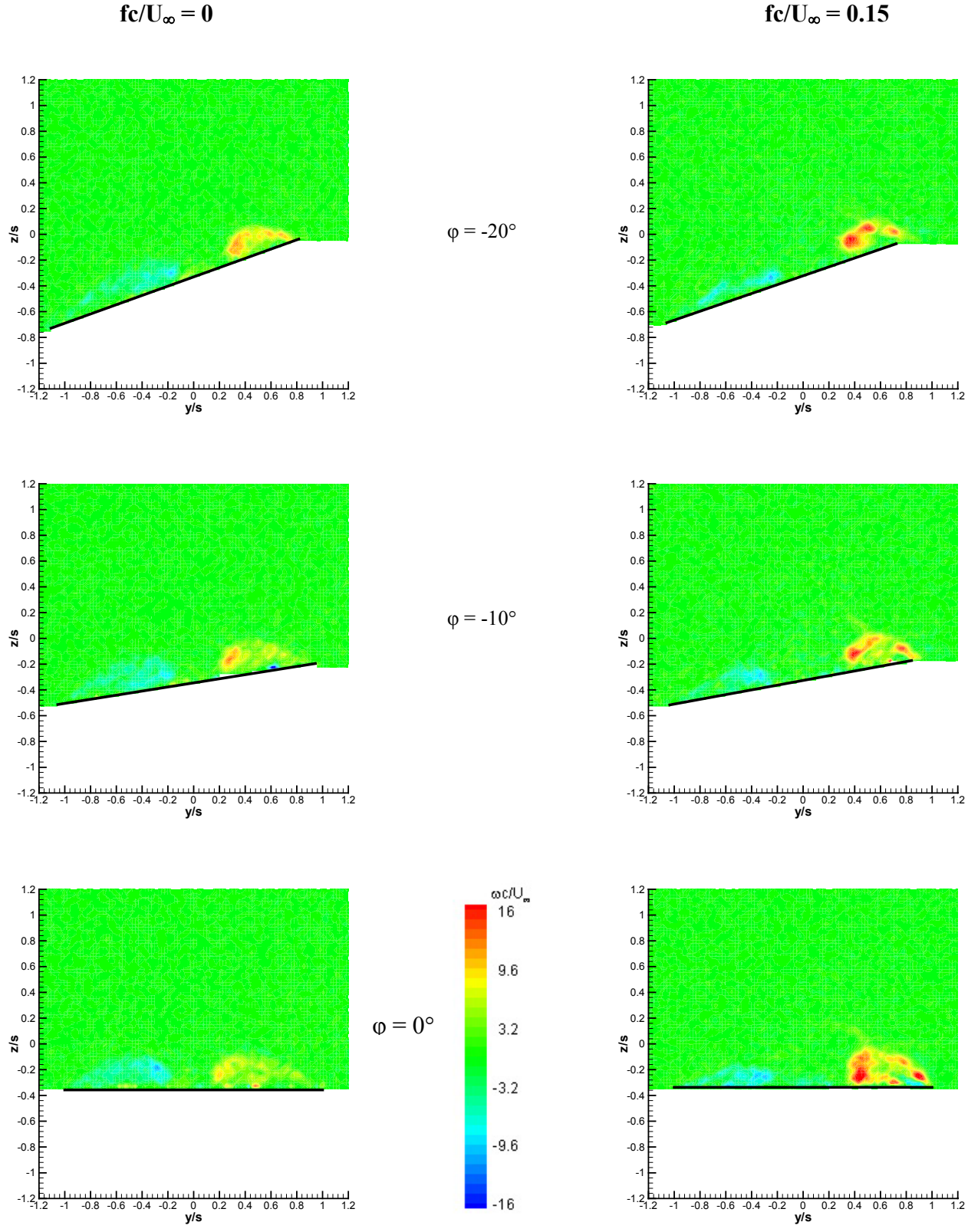

Figure 50: Comparison of vorticity in a cross-flow plane at x/c=0.8 for the static and dynamic cases, α=20°.

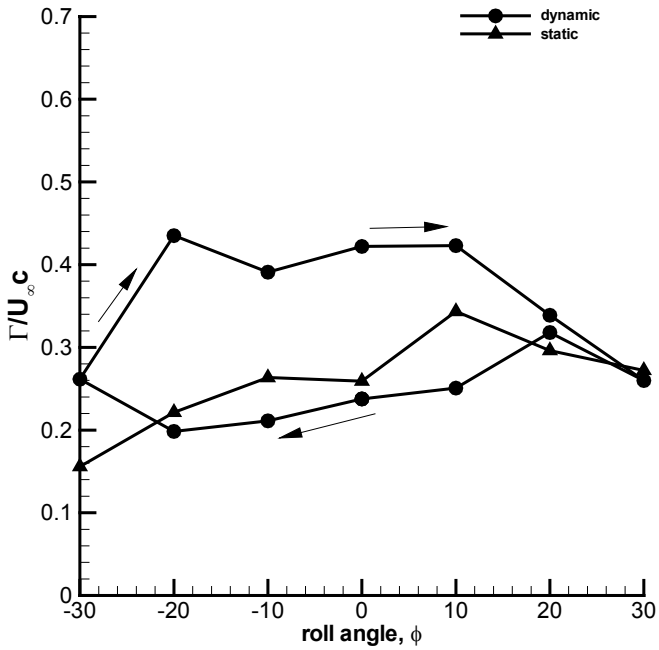

Figure 51: Variation of circulation for the counter-clockwise vortex over a cycle for the static and dynamic cases at α=20°.

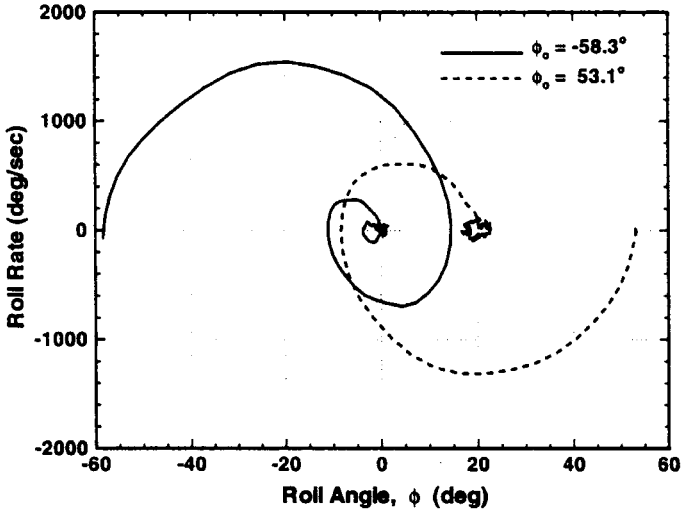

Figure 52: Phase plane trajectories for two values of initial roll angle, α=30°, Λ=65° [79].

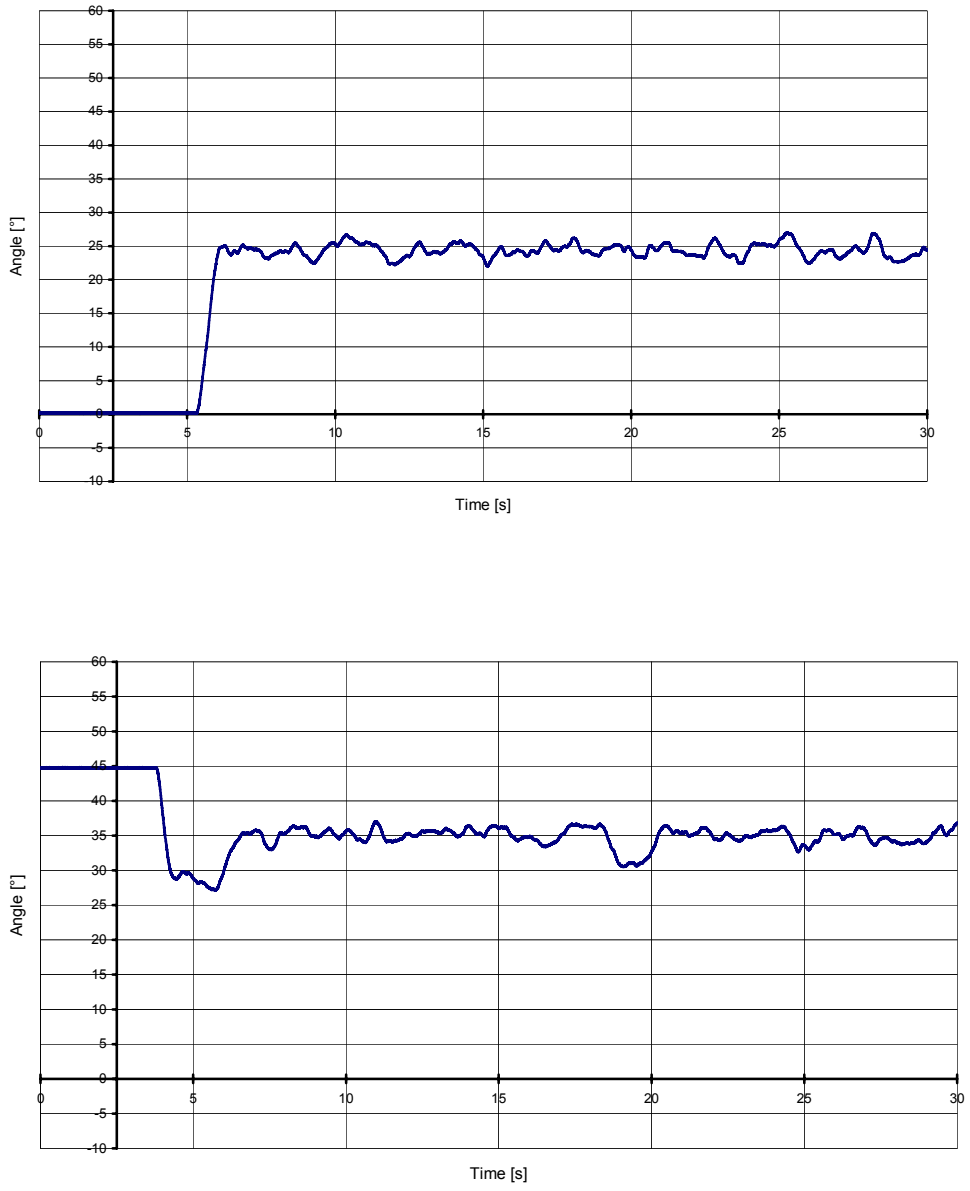

Figure 53: Time histories of roll angle for two values of initial roll angle, α=15°, Λ=50°.

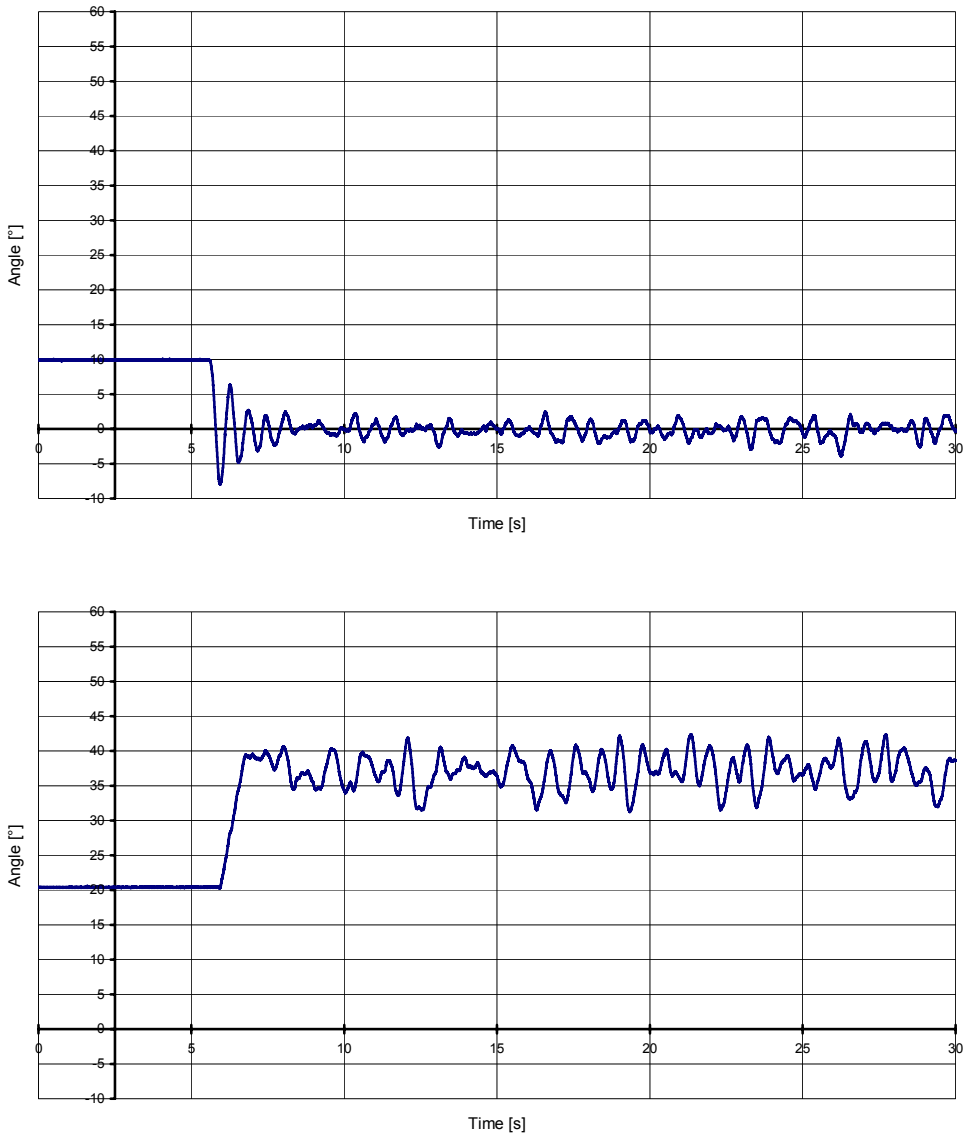

Figure 54: Time histories of roll angle for two values of initial roll angle, α=32.5°, Λ=50°.

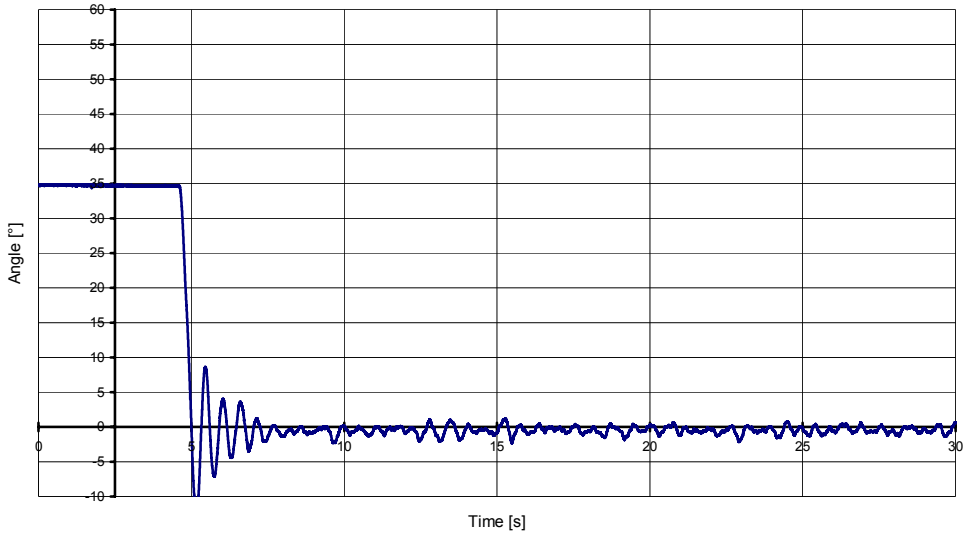

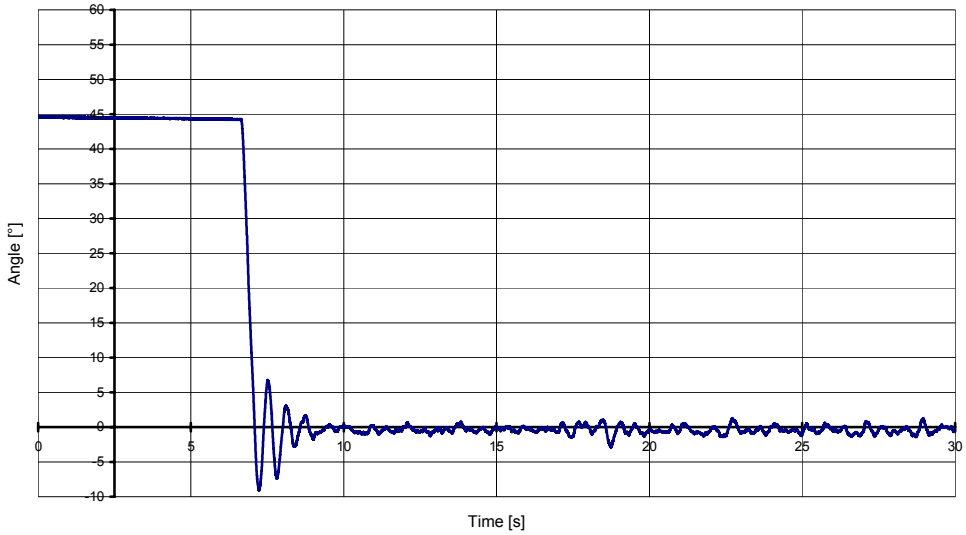

Figure 55: Time histories of roll angle for two values of initial roll angle, α=35°, Λ=50°.

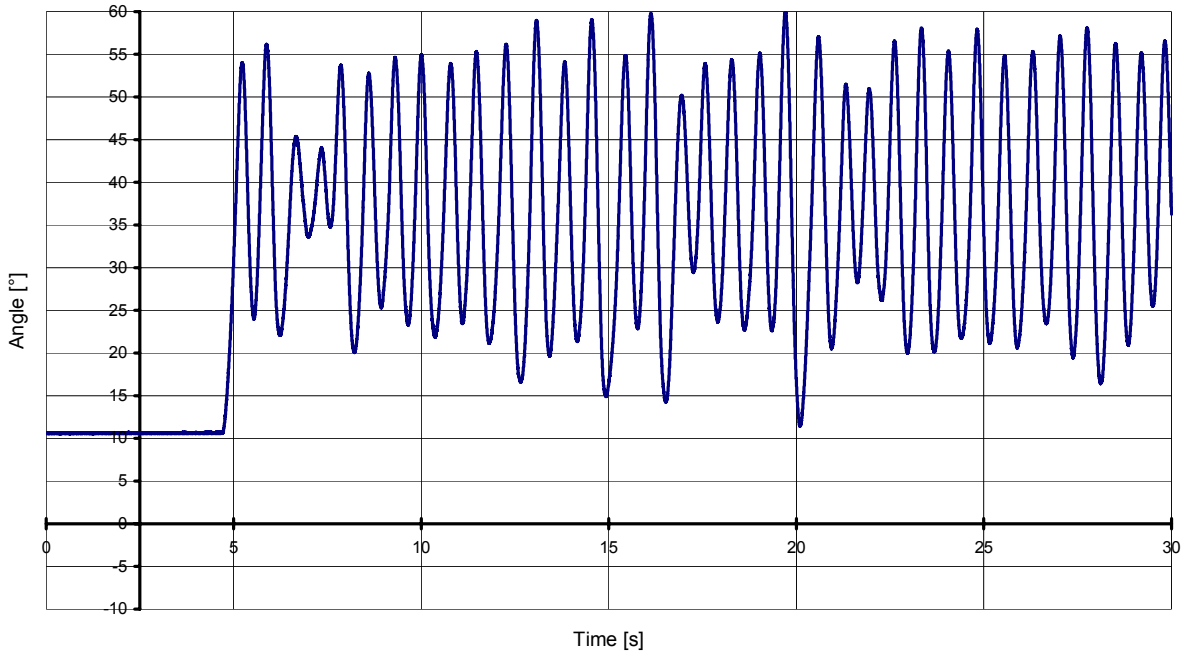

Figure 56: Time history of roll angle for α=27.5°, Λ=50°, ϕ_0=10° for rounded leading-edge.

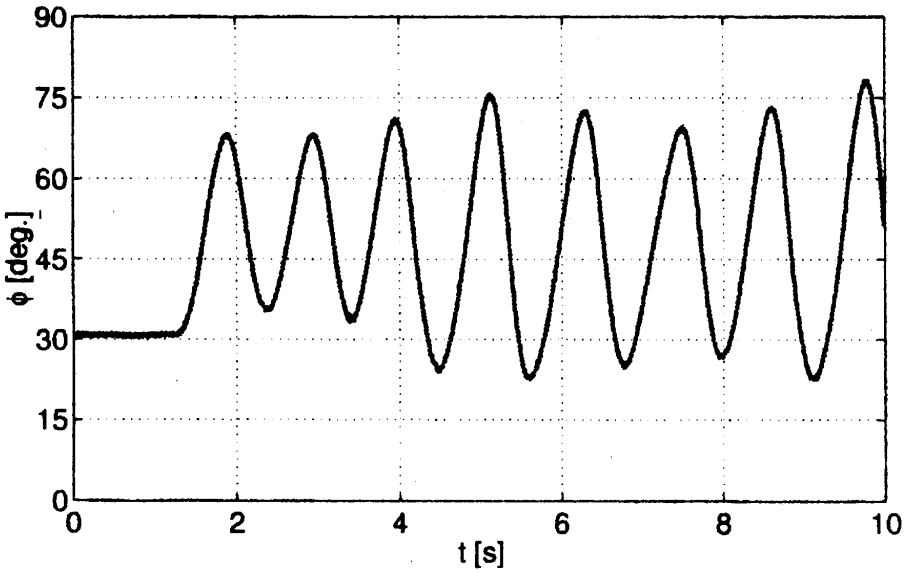

Figure 57: Time history of roll angle for α=30°, Λ=45°, ϕ_0=30° for rounded leading-edge [87].

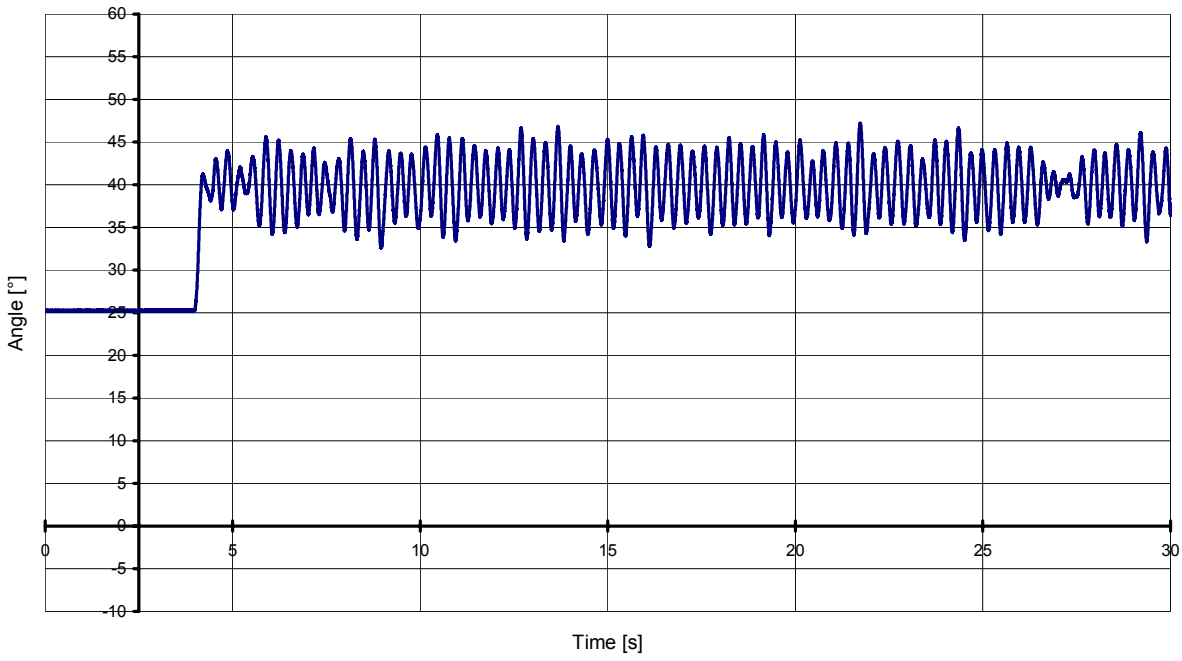

Figure 58: Time history of roll angle for α=22.5°, Λ=50°, ϕ_0=25° for sharp leading-edge.

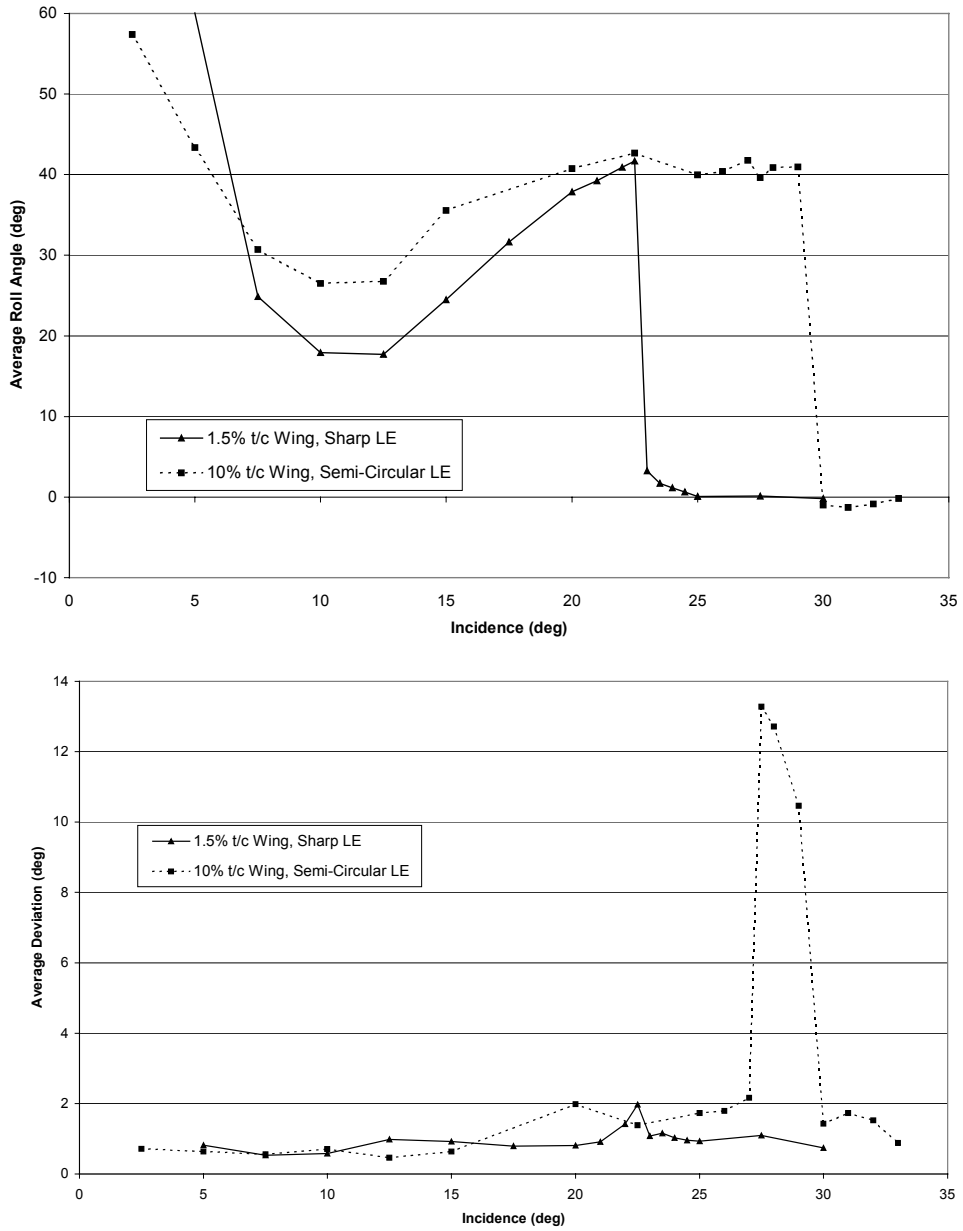

Figure 59: Variation of mean (top) and standard deviation (bottom) of roll angle as a function of angle of attack for sharp and rounded leading-edges.